6-19-2017

# Plasmonic Effect on Exciton and Multiexciton Dynamics of Quantum Dots near Metal Nanostructures

SWAYANDIPTA DEY
*University of Connecticut - Storrs*, diptachem007@gmail.com

# Plasmonic Effect on Exciton and Multiexciton Dynamics of Quantum Dots near Metal Nanostructures

Swayandipta Dey, Ph.D.

University of Connecticut, 2017

Recent scientific progress has resulted in the development of sophisticated hybrid nanostructures composed of semiconductor nanocrystals (quantum dots, QDs) and metal nanoparticles (MNPs). These hybrid structures open up new possibilities for developing next generation nanoscale optoelectronic devices that combine the best attributes of each component material. The optical response of MNPs is dominated by surface plasmon resonances which create large local electromagnetic field enhancements. When coupled to surrounding semiconductor components, the enhanced local electric field results in strong absorption/emission, alteration in emission decay rates, enhancement in exciton emission and other interesting non-linear effects (multiphoton generation). Although hybrid nanostructures are poised to be utilized in a variety of applications, serious hurdles for the design of new devices still remain. These difficulties largely result from a poor understanding of how the structural components interact at the nanoscale. These synergetic interactions strongly depend on the exact composition and geometry of the structure, and therefore, a quantitative comparison between theory and experiment is often difficult to achieve. My dissertation work primarily focuses on paving a bridge between the experimental and theoretical studies and the mechanisms involved in exciton and multiexciton emission dynamics of single QDs in presence of plasmonic nanostructures by careful consideration of different parameters which significantly affect the interaction between these nanoparticles at a single particle level.

# Plasmonic Effect on Exciton and Multiexciton Dynamics of Quantum Dots near Metal Nanostructures

Swayandipta Dey

M.Sc. Integrated., Pondicherry Central University, India [2011]

**A Dissertation**

**Submitted in Partial Fulfillment of the**

**Requirements for the Degree of**

**Doctor of Philosophy**

**at the**

**University of Connecticut**

**2017**

**2017**

# APPROVAL PAGE

Doctor of Philosophy Dissertation

## Plasmonic Effect on Exciton and Multiexciton Dynamics of Quantum Dots near Metal Nanostructures

Presented by

Swayandipta Dey, M.Sc. Integrated

Major Advisor

_____

Dr. Jing Zhao

Associate Advisor

_____

Dr. Xudong Yao

Associate Advisor

_____

Dr. Yu Lei

**University of Connecticut**

**2017**

**Dedicated To**

*My late grandfather Mr. Ajit Kumar Das, my parents and my sister*

**Acknowledgements**

The work in this thesis ended up being the culmination of many collaborations and discussions with an astounding variety of wonderful people. To start off with, I would like to thank my research advisor, Dr. Jing Zhao, for providing me the resources in order for me to pursue my project ideas. The unique combination of resources, people and research projects you have cultivated gave me the opportunity to study an incredibly diverse assortment of topics, and much of the interesting works in our group has arisen from your strong collaborative culture that you had instilled over the years. Your commitment to quality and willingness to see things through goes unparalleled and invaluable and I am glad to have been able to spend all these years working with you.

My heartfelt thanks go to my collaborators Dr. Ou Chen (Brown University) for providing me with your high-quality quantum dot samples for my studies and for all your advice and guidance during conference meets. I would also like to thank my collaborator Dr. Shengli Zou (University of Central Florida) for providing us with theoretical calculations and simulations to explain my studies. I am also grateful to my committee members Dr. Xudong Yao and Dr. Tomoyasu Mani for their guidance and wisdom, and specially all their advice helping me figure out with my next career steps. I am equally thankful to my research collaborator and associate advisor Dr. Yu Lei who let me work jointly on some interesting projects with his student Xiangcheng Sun who has been a great friend of mine during my time here at UCONN and for all the valuable discussions and advice you have had for me. I would also like to thank Dr. Joseph DePasquale for passing on your love of teaching (teaching with you has added quite an invaluable experience on fostering and mentoring young minds!) and for all your guidance and friendly talks to cheer me up while I taught for you during my time at UCONN. I am also grateful to the Department of Chemistry and Institute of Materials Science, University of Connecticut and their employees for their support during my graduate studies. I would also like to take a moment to extend my heartfelt thanks to

my career strategist and professional development mentor Dr. Daniel Eustace who has always taught me how not to never give up with things that I care about most and how to tackle every difficult situation that fall in my way.

My sincerest thanks to my dearest colleagues Julie Jenkins and one of my good travel buddies, Sravan Thota who started off their graduate research at the same time with me. I will be always grateful for all your endless assistance and contributions to my projects and all the critical feedback that you have passed along during the course of my dissertation research. Outside UCONN, I really enjoyed the company of my wonderful roommates Kailendra, Pavan and Umesh. Thank you all for your friendship, support, and most importantly, a strong bond of brotherhood that we had developed over the last four years!

Thanks to my family for their support, sacrifices and encouragement during all these years and for letting me pursue my dreams without any barriers! Thank you, Mom and Dad, for always believing in me, and always standing by my side and for laying a solid foundation of my life. Without all these years of your relentless support and blessings, I would not be here where I am today. A very special thank you goes to my little sister Sanhita, who has particularly been my best friend and my ultimate backbone right from my childhood. I would also like to thank all my well-wishers and everyone else, for all your encouragement and support during this journey. Finally, my thanks and praise to the Almighty Himself for all your blessings to me and for all the strength you give me each day to help me grow and stand up as a better person.

# Table of Contents

# List of Figures

# List of Tables

# Chapter One .

# Plasmonic Effect on Exciton and Multiexciton Emission of Single QDs near Metal Nanoparticles



## 1.1. Abstract

Quantum dots are nanoscale semiconducting quantum emitters with high quantum yield and size-dependent emission wavelength, holding promises in many optical and electronic applications. In the first half (Section 1) of this chapter, we will first introduce about some of the fascinating optical phenomenon exhibited by single colloidal quantum dots, particularly, photon antibunching and photoluminescence blinking. Then we will introduce the applicability of single quantum dots on non-classical light generation and the photon antibunching property manifested by these nanocrystals. A brief theoretical background on photon emission statistics and experimental methods to measure photon statistics and multiexciton quantum yield will be subsequently discussed. Next, in the latter half of the chapter (Section 2) we will talk about how the plasmons from metal nanoparticles affect the exciton and multiexciton emission of single quantum dots. When quantum dots are situated close to noble metal nanoparticles, their emitting behavior can be conveniently tuned because of the interaction between the excitons of the quantum dots and the plasmons of the metal nanoparticles. This interaction at the single quantum dot level gives rise to reduced or suppressed photoluminescence blinking and enhanced multiexciton emission, which is difficult to achieve in isolated quantum dots. However, the mechanism of how plasmonic structures cause the changes in the quantum dot emission remains unresolved. Due to

the complexity of the system, the interfaces between metal, semiconductor, and ligands must be considered, in addition to factors such as geometry, interparticle distance, and spectral overlap. The challenges in the design and fabrication of the hybrid nanostructures, as well as in understanding the exciton-plasmon coupling mechanism can be overcome by a cooperative effort in synthesis, optical spectroscopy, and theoretical modeling.

## 1.2. Introduction

### *1.2.1. Non-classical light generation from single quantum dots*

Over the last few decades, a significant amount of research has been involved in the field of nanoscale quantum optics. This was triggered due to the advancement of various top-down and colloidal bottom-up synthetic approaches aimed primarily in developing high quality inorganic semiconducting nanocrystals (also known as quantum dots, QDs). Besides possessing size dependent emission color tunability and high photostability, these unique classes of materials also exhibit atom-like discrete energy spectrum and sharp emission lines which arises as a direct consequence of spatial quantum confinement of charge carriers. These QDs are highly solution processable and have shown potential to be integrated into different solid-systems and microcavities which makes highly advantageous to use them as optically or electrically triggered solid state single photon sources.[1-5] Additionally like various other pre-existing non-classical and single photon sources such as single nitrogen vacancies and color centers in diamond, single trapped ions, single fluorescent organic molecules, these QDs also demonstrated capability of generating non-classical light under room temperature conditions. This unique property also makes them potential candidates for device applications in the fields of quantum communication and quantum cryptography.[6,7-12] Therefore, it is imperative towards developing a profound

understanding of the quantum optical properties of these nanocrystals. These unique quantum optical properties can be further explored using certain well-established photon correlation spectroscopic measurements which are primarily based on photon emission statistics of the materials and light sources. According to the laws of quantum optics, the process of non-classical light generation cannot be explained based on the classical electromagnetic theory. Instead, it is based on a quantum mechanical model where the atoms as well as the radiation field is assumed to be quantized, thus describing the correlation and discreteness of light generated by most two-level quantum emitter system such as a single atom, ion or an exciton in a quantum dot. The non-classical light generation is based on creating radiating light fields with suppressed photon number fluctuations unlike what is observed in most of the naturally available classical light and thermal sources.

### *1.2.2. Theoretical Background on Photon Statistics*

Coherent or Glauber states which has been named after Roy Glauber for his pioneering work in the field of quantum optics represent an example of a well approximated classical light source. This idea of coherence is not strictly related to the classical term, but instead it refers to a special kind of quantum mechanical state of the light field that corresponds to a single resonator mode having a well-defined amplitude and phase relation. An example for such a source is laser and the states generated by a laser emission.[13-15]

The probability of finding n number of photons or the photon number distribution in a coherent state follows Poissonian statistics which is given by $P(n) = \frac{e^{-\langle n \rangle}\langle n \rangle^n}{n!}$; where the mean photon number $\langle n \rangle = |\alpha|^2$ where $\alpha$ can be represented as the basis of the eigenstates of photon number operator. For, non-classical light sources and thermal (or chaotic) sources which exhibit a

relatively narrower and wider photon number distributions or photon fluctuations follow sub-Poissonian and super-Poissonian distribution respectively.[12] Therefore, this difference in statistical distribution of photon emission gives us a general idea on how to build light sources and thereby manipulate photon emission by generating different kinds of radiating light fields.[12, 16-17] The comparison in the photon number distribution from different light sources has been illustrated in **Figure 1.1**.

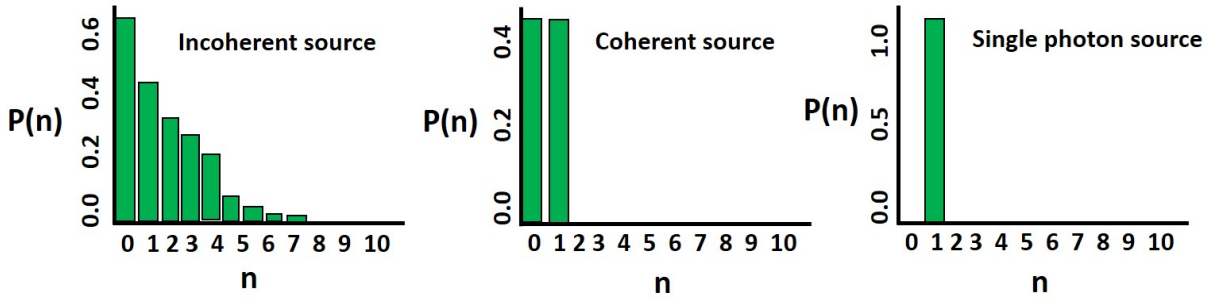


**Figure 1.1**. Difference in probability distribution, denoted by P(n) as a function of the number of photons, n for various light sources. The incoherent (e.g. thermal) source exhibit wide number fluctuations around the mean photon number. The coherent light source (e.g. laser) presents a Poisson distribution, narrower than that of thermal light, but with still strong number fluctuations. A non-classical light source (e.g. ideal single photon source) delivers a minimal and particularly discrete photon number fluctuation with n = 1.[17]

Light sources can be therefore classified based on the temporal sequence (i.e. time dependent separation) or photon number fluctuations around a particular coherence time($\tau_c$) and the type of statistical distribution model that the photon number or intensity fluctuation follows.

So, for photons emitted from conventional light (incoherent) sources such as spectral, incandescent, blackbody sources or thermal light sources tend to arrive in bunches i.e. the probability to observe more than one photon arriving closely spaced in time is particularly high. Therefore, we also refer these light sources as "bunched" and the phenomenon as photon bunching. The statistics of photon distribution from these sources follow a Bose-Einstein distribution. Whereas for coherent light source such as one emitted from a laser, the information on photon arrival times are mostly uncorrelated and the photon statistics are described by Poisson distribution as discussed earlier. In contrast to most of these coherent and classical light sources, non-classical light sources (sometimes refer to as squeezed light sources) which exploit various non-linear quantum optical effects such as single nitrogen vacancy, trapped ion, atom or even a single colloidal QD can generate antibunched light with suppressed photon number fluctuations.[12, 17,1, 18-19] The schematic representation of photon arrival sequence for different kinds of light sources as a function of time has been illustrated in **Figure 1.2**.

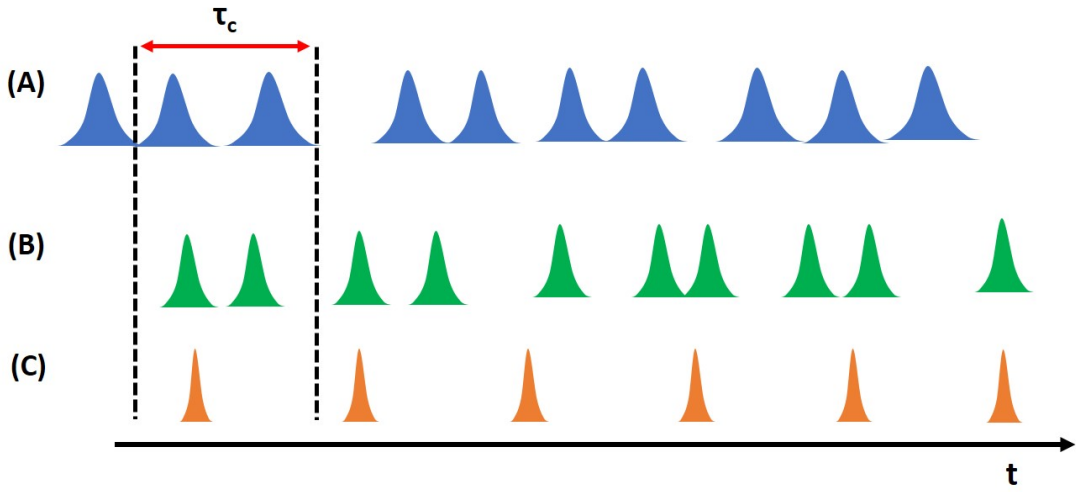


**Figure 1.2**. Photon arrival sequence as a function of time for (A) bunched (photons arrive together) (B) random or coherent (no correlation to photon arrival) and (C) antibunched light (photons arrive with a finite time lag); $\tau_c$ is the coherence time.

The physical reason behind the photon antibunching phenomenon lies in the very fact that for a single two-level discrete quantum emitting system. So, between every successive single photon emission event, there always exists a certain finite time lag or time lapse since after a photon is emitted from its excited state $|1\rangle$ to its ground state $|0\rangle$ as illustrated in **Figure 1.3**, the emitter needs to get re-excited before it can emit again. The fluctuations in this generated photon stream when observed as a function of time follows a sub-Poissonian distribution. In fact, this ability to control and generate single photons on demand under an external electrical or optical trigger which at the same time can operate at room temperature can be of potential interest to several future applications in the field of quantum communication technologies.[12, 17, 20]

A non-classical light state which is represented by a photon number or Fock state $|n\rangle$ can be generated by an ideal single photon source.[7, 12] The photon number or intensity fluctuations exhibited by that of a single Coherent and Fock states are completely different when the probability

of photon distribution is calculated around a particular mean photon number. **Figure 1.3A** and **B** displays the difference in the photon number distribution for the Coherent and Fock states respectively.

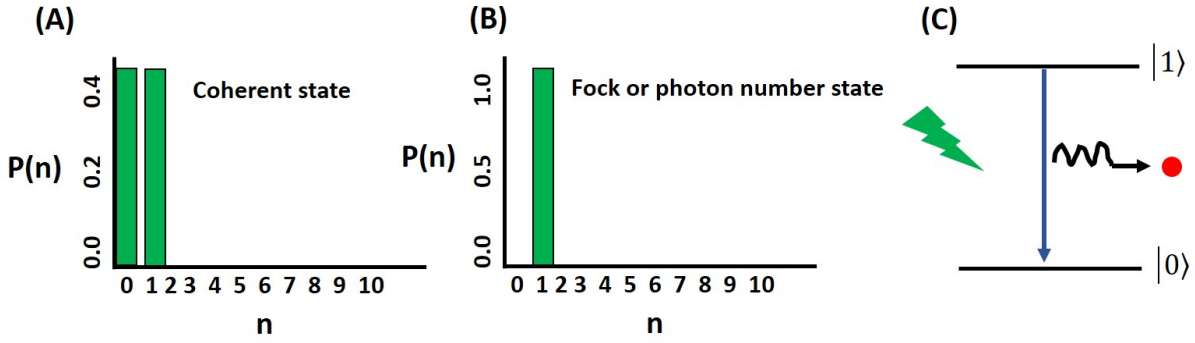


**Figure 1.3**. Probability distribution difference in photon number fluctuations for (A) Coherent and (B) Fock states (C) A simple diagrammatic representation of a two-level quantum emitting system spontaneously emitting a single photon.[12]

### *1.2.3. Experimental method for Photon Statistics and Multiexciton Quantum Yield measurements in single QD*

One most frequently used experimental method to derive the photon number distribution of an emitter involves measurement of second-order correlation function which is defined mathematically as:

$g^{(2)}(\tau) = \frac{\langle I(t)I(t+\tau)\rangle}{\langle I(t)\rangle^2}$ where I(t) is the measured intensity.

$g^{(2)}(\tau)$ describes the probability to measure a photon at time $\tau$ on condition that a first photon has been already detected at time $\tau = 0$. In photon correlation, $g^{(2)}(\tau)$ is proportional to the histogram of photon pairs with time $\tau$ between them. Therefore, the function $g^{(2)}(\tau)$ can be considered as a sort of "conditional probability" of observing two-photon emission from an emitter; which essentially means given that a photon has already been detected, how likely another photon can be detected after a finite time $\tau$. [21-22]

For an ideal single photon source, $g^{(2)}(0) = 0$; whereas for a coherent light source (e.g. laser), following a typical Poisson distribution, the value for $g^{(2)}(0) = 1$ and for other chaotic light sources (incoherent sources), the typical values for $g^{(2)}(0) > 1$.This difference in $g^{(2)}(\tau)$ values can be represented in a histogram as in **Figure 1.4**.

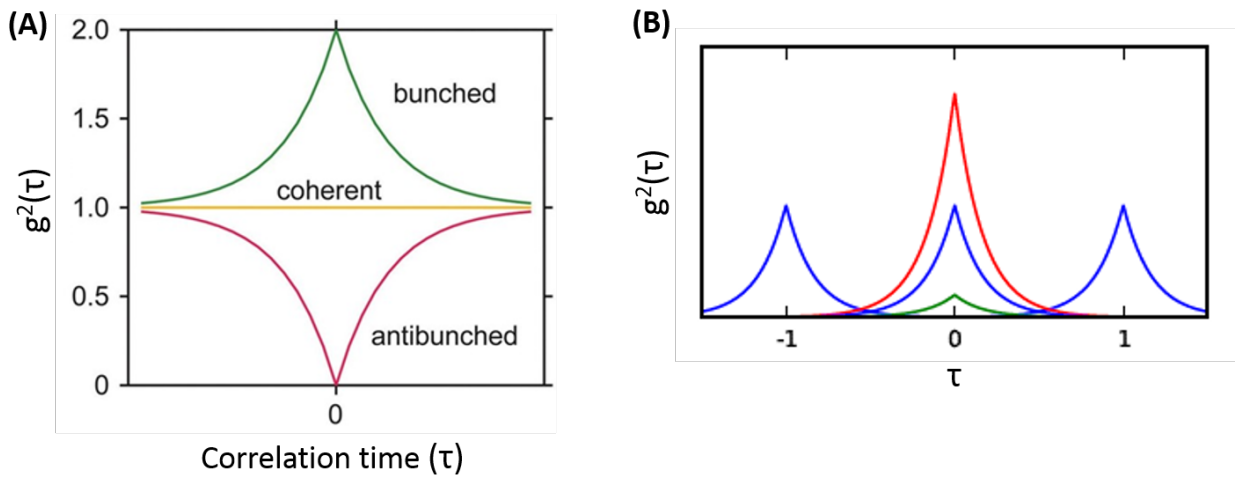


**Figure 1.4**. (A) An illustration of photon statistics, as measured using $g^{(2)}$ under continuous wave excitation. Bunched (green), Poissonian from coherent laser source (yellow) and antibunched (red) emission, as measured through $g^{(2)}(\tau)$. (B) Equivalent bunched (red), Poissonian (blue), and antibunched (green) emission, as measured under a pulsed excitation.

The pulse repetition period in our experiments is set at longer time intervals (2.5MHz i.e. 400ns time interval in our studies), a duration which is typically much longer than $\tau_{rad}$ in order to avoid the overlap of triggered photons generated by consecutive pulses. The emitted photons from the sample are collected by the same objective and further directed to a standard Hanbury-Brown and Twiss interferometric setup. It consists of a 50/50 non-polarizing beam-splitter and two (start/stop) single photon avalanche photodiodes (SPADs) with a time resolution of 300 ps and the emitted photons under inspection are collected by these two single photon detectors, where one SPAD is a "start" channel which begins counting until the other SPAD, the "stop" channel, detects a photon and ends the count. Then a histogram of the arrival time separations of photon pairs n(τ)

will be produced which is proportional to $g^2(\tau)$ as long as the measured time separation $\tau$ between photon pairs is much smaller than the mean time between detection events.[23-29] The absence of photon coincidences at zero inter-photon delay time under pulsed and continuous excitation proves that colloidal QDs can act as perfect single-photon emitters at room temperature. An ideal single-photon emitter like a single QD can also be excited by a pulsed laser source. For every single excitation pump pulse, only one photon gets emitted. If there is absolutely a single photon emission taking place, the value of $g^2(\tau)$ at $\tau = 0$ should be 0.

A typical experimental set-up that has been implemented in our studies along with the photon correlation histograms constructed from these experiments under both pulsed and continuous wave excitation has been illustrated in **Figure 1.5**. The photon antibunching observed in QDs are quite similar to that of a single atom-like discrete quantum emitting system, therefore due to this quantum confinement based discreteness in emission exhibited by the QDs led them to be often termed as "artificial atoms".[18, 26, 30-32]

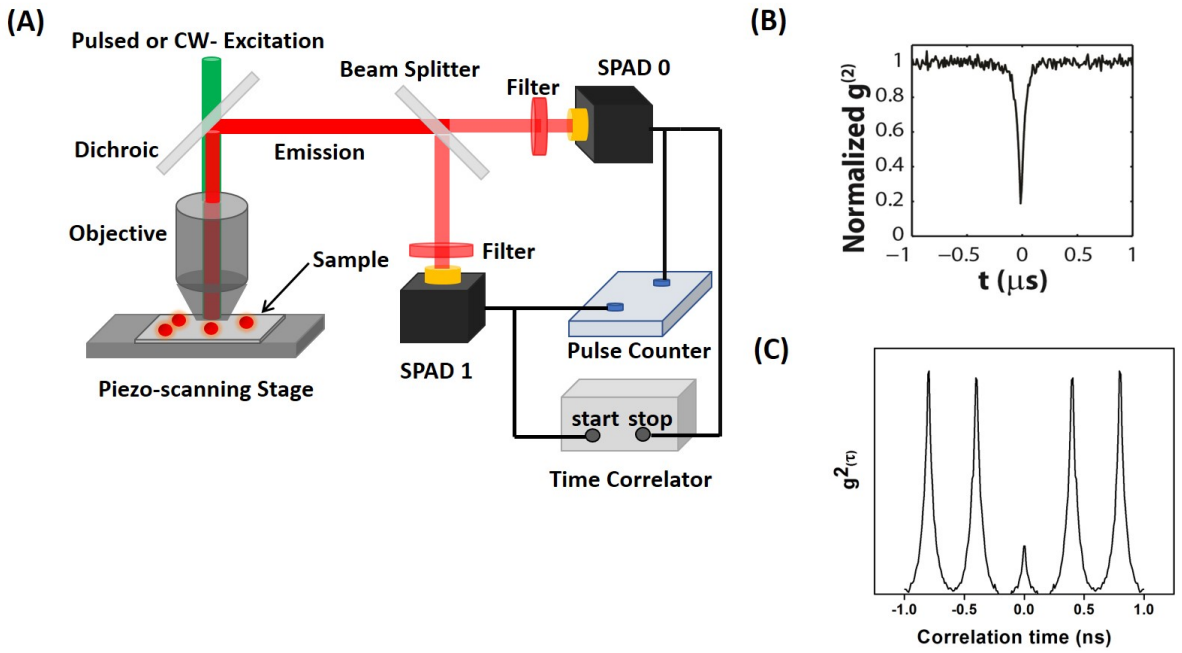


**Figure 1.5**. (A) Schematic representation of a Hanbury-Brown Twiss photon-correlation set-up.[21] Co-incidences between the counts on the two detectors (SPAD 0,1) gives access to quantitative determination of the second-order correlation function, $g^{(2)}(\tau)$; Typical photon correlation histograms obtained from a single QD under (B) a continuous-wave excitation and (C) pulsed excitation sources[33]

Traditionally, to determine biexciton lifetimes or quantum yield of QDs, QDs need to be excited using high power and complicated modeling is involved. Due to the harsh experimental conditions, it is not feasible to study biexcitons in single QDs due to the high probability of photobleaching or photo-oxidation. Here, we will use a technique recently developed by Nair et al to measure the biexciton (BX) quantum yield (QY) of single QDs under mild conditions based on photon statistics.[33] Theoretically, the BX QY can be obtained from the emitter's second-order intensity correlation function, $g^{(2)}$, which is readily measured using modern time-correlated single photon counting systems. In the limit of weak pulsed excitation regime where the average exciton

occupancy (also interpreted as the number of photons absorbed per pulse), $\langle N \rangle \rightarrow 0$, the ratio between the biexciton (BX) to exciton (X) quantum yield (QY) can be quantitatively derived as the integrated area ratio of center ($\tau = 0$) to side ($\tau = \pm t_{rep}$) peaks. Under the continuous wave excitation source, this second order correlation function in terms of ratio between BX to X quantum yield can be realized by the "dip" size in a normalized histogram. The zero-time delay peak at $\tau = 0$ as observed in these photon correlation histograms attributes to the percentage of BX QY which reflects the probability of creation and subsequent two photon emission of the emitter.[33-34]

### *1.2.4. Photoluminescence Intermittency or Blinking*

One of the most widely investigated photophysical properties of single colloidal QDs is photoluminescence intermittency or blinking. This optical phenomenon involves a random reversible stochastic switching between bright "on" and dark "off" events that extend from few milliseconds to minutes. The probability of occurrence of individual on- and off-events are characterized by a power-law distribution of "on" and "off" times[35-39] as shown in **Figure 1.6**.

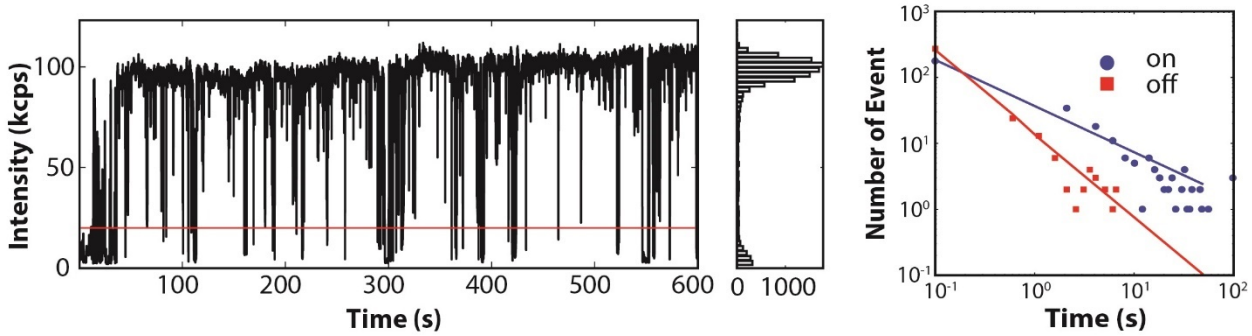


**Figure 1.6**. Time dependent PL intensity trace of a single CdSe/CdS nanocrystal under a continuous wave excitation. The red line within the PL blinking trace data indicates the threshold used to calculate the on and off-times probability distribution. The histogram of intensity distribution obtained from the intensity-time trace for the entire collection period of 600 seconds. The right-side panel shows the log-log plot of weighted on- and off-times probability distribution obtained using bin-threshold analysis exhibiting power-law statistics

Since the time this phenomenon of photoluminescence blinking has been first observed in QDs, a significant amount of research interest has been devoted to understand the underlying mechanisms involved in this process that has led to different hypotheses based on rigorous experimental and theoretical models. However, till date, the exact mechanism of this fluorescence intermittency phenomenon has not been completely understood yet, although it is believed to be strongly associated with the complex interplay between the surface chemistry of the nanocrystals itself and the fate of the photoexcited charge carriers (in terms of generation and recombination kinetics). This alternating sequence of "on" and "off" events could be distinguished by applying an appropriate threshold to the binned intensity traces. An intensity-time trace as shown in **Figure 1.6** is constructed by integrating the measured intensity (or number of detected photons) over time bins of fixed width. The probability distribution densities of "ON" and "OFF" times follow some sort of a power law function $P(\tau_{on/off}) \propto \tau^{-\propto}$ when the probability distribution function ($P_{on}$ or $P_{off}$) are plotted against time in a semi log-log plot. The value of the exponential factor $\alpha$ usually lies between the values of 1 and 2. This kind of statistical data analysis of "on" and "off" time probabilities derived from intensity-time trace is popularly known as Bin-Threshold analysis.[40-41]

One of the earlier models that was proposed to explain the mechanism of blinking assumed this random sequence of alternating dark (OFF) state and a bright (ON) state as a result of photoinduced charging-discharging processes of the QDs.[26, 42] After the QDs are optically excited, the electron-hole pair(exciton) that gets created when radiatively recombines results in an uncharged or neutral ON state. However, in presence of an excess charge carrier or if one of the charge carrier gets trapped, it results in creation of effective non-radiative Auger recombination channels which leads to an ionized or charge state that leads to a low-intensity OFF state. However

recent findings on this topic has challenged the validity of this hypothesis which seems to ignore the interplay of other factors involved in this complex phenomenon such as presence of additional charges, existence of trap states and other non-radiative pathways.[42-47] Thus, despite the tremendous studies and existence of various theoretical models, a unified explanation behind the physical origin of blinking is still yet to be answered. Thus, a rather non-blinking nanoscale light emitter will become an important breakthrough for several practical applications that is often hindered by this random intermittent on/off blinking process observed in most currently existing colloidal QDs. That the blinking behavior can be influenced by surface modifications makes us think the first steps to achieve that goal have been made. However, that's not certain as the origin of power-law kinetics still remains unknown but hopefully in the forthcoming years, we will be able to solve this puzzle and develop rigid theoretical models to better explain the underlying mechanisms behind power-law blinking in single semiconductor nanocrystals.

### 1.3. Background on Plasmon-Exciton coupling in metal-semiconductor nanocomplexes

Nano-photonics has been an active and evolving field for the past two decades that aims at creating nanoscale optics and understanding their optical properties. The fabrication and application of nano-photonic devices are widely studied across various disciplines ranging from fundamental physics, to medicine.[48] Nano-photonic elements are capable of concentrating light beyond the classical diffraction limit and manipulating light-matter interaction at the nanoscale.[49-51] Their unique optical signatures have led to the discovery of a plethora of new optical phenomena. Nowadays, the development of next generation nano-photonics heavily relies on utilizing a diverse set of building blocks to form hybrid nanostructures.[52] The hybrid structures often exhibit unconventional optoelectronic properties due to the synergetic interaction between the individual

components. By controlling parameters, like the spatial geometry and building block composition, the optical properties of the hybrid structures can be tailored for various desired applications. Two important nano-photonic elements are plasmonic metal nanoparticles (MNPs) and excitonic quantum dots (QDs). The plasmon-exciton interaction in the hybrid metal-semiconductor nanostructures alters the exciton generation and recombination dynamics of the QDs, which opens up new doors in the fields of optical communication, lasing, bio-sensing, and energy.[53-57]

It is well known that the excitation of plasmons in MNPs can dramatically modify the emission behavior of nearby fluorescent materials.[58-62] Depending on the configuration of the system, the photoluminescence (PL) of the emitters can be either enhanced or quenched at both the ensemble and single particle level, due to the strong interaction between the emitter and the metal surface.[63-72] Various time-resolved spectroscopic studies on plasmonically coupled QDs have demonstrated that the radiative decay rate, absorption cross section, and PL quantum yield of the QDs increase in the presence of metal nanostructures. An alteration in one or more of these properties can in turn modulate the excitation and emission rate of the QDs, resulting in significant modification of the exciton dynamics (generation, dissociation or recombination of electron-hole pairs). The synergistic plasmon-exciton coupling process between the QDs and metal NPs results in complex interplay of different competing interactions. Due to these interactions, several processes occur. First, the plasmonic enhancement due to metal NP increases the effective absorption cross-section and excitation rate of the quantum emitter(QD). Secondly, the radiative decay rate of the QD gets enhanced due to Purcell effect. And lastly, if the QD is located in near proximity (interparticle distance, $d \leq 50$nm) to the plasmonic nanostructures, there are extraneous non-radiative resonant energy transfer channels that open up through which energy transfer takes place from the QD to the metal NP. However, it is worth noting that this dipole-dipole coupling

between the QD and metal NP which results in some sort of non-radiative surface energy transfer follows $R^{-x}$ (x= 2-4) which is not exactly similar as conventional FRET that follows $R^{-6}$ dependence. Unlike FRET (whose efficient energy transfer range lies between 2-8 nm), non-radiative energy transfer through this process can even occur efficiently over larger inter-particle separations.[15-17]

The alteration in the radiative decay or the spontaneous emission rate of the QD when it is placed in near-proximity to a metal NP is caused due to change in local optical density of states which known as Purcell effect. The Purcell factor($F_P$) gives us an idea on the degree of change in emission rate of the quantum emitter in presence of cavity and free-space emission which is usually expressed as $F_P = \frac{k'}{k_0} = \frac{3Q\lambda^3}{4\pi^2 V}$ where $k_0$, $k'$ represent the free-space and modified emission; Q is the cavity quality factor and V is the cavity volume. Although metal NPs have been rigorously used to enhance the radiative transition rate of the emitter due to their ability to strongly confine the light beyond the diffraction limit or at sub-wavelength volumes, due to strong damping or optical losses it often deteriorates the cavity quality factor.[18-20] Nevertheless, metal NPs can act as a plasmonic cavity possessing high optical/photonic density of states with small mode volume. As a result of the strong electric field enhancement due to collective surface electron oscillations in metal NP and the confinement of light within the small nanoscopic volume, the number of available local optical density of states or the electromagnetic modes significantly increases which subsequently amplifies the radiative emission rate of the QD when it is located nearby the metal NP.[21-22] The radiating plasmon model has certain implications on the photoluminescence enhancement or quenching of QD that are present near metal NP which can be predicted from the optical properties of the metal.[23-24] According to this model, once the plasmons in the metal NP get excited, they can re-radiate into far-field or free space ($k_r^{PL}$) or they can be lost in the form of

absorption or internal damping ($k_{nr}^{PL}$). The efficiency of these processes depends strongly on the size, shape and composition of the metal NP. In regard to this, while considering the resultant emission enhancement or quenching of the nearby QD, it not only depends on the intrinsic property of the emitter but also it is directly proportional to the ratio of scattering cross-section (follows $r^6$, r = size of the metal NP) to absorption cross-section (follows $r^3$) of the metal NP itself. Therefore, radiation via scattering dominates for larger NP and absorption for smaller NP.[25-26] The total decay rate of the plasmons however is much faster, usually of the timescale(tens of fs to few hundreds of ps);so if the plasmons decay much faster compared to the QD, the rate of light emission by the QD to the far-field is $k_{far} = k_{r,0} + \frac{k'_R.k_r^{PL}}{k_r^{PL}+k_{nr}^{PL}}$ where $k_{0,r}$ is the radiative emission rate of the emitter into free space and $k'_R$ is the additional decay rate due to plasmonic coupling to the metal NP. Usually for most of the experiments, the intrinsic radiative decay rate($k_{r,0}$) << $k'_R$, therefore the far-field emission rate is not affected too much as a result of direct emission modification.

For an optimally placed QD around a metal NP, the spontaneous emission rate ($k'_R$) radiating into surface plasmon modes can exceed the $k_{r,0}$ and $k_{nr,0}$ associated with the intrinsic radiative and non-radiative decay channels of an isolated QD. This results in a highly efficient coupling associated with an enhancement in total decay rate($k_{total}^{'}$) compared to an isolated emitter ($k_{total}^{0}$). The total decay rate of an isolated emitter system $k_{total}^{0} = (k_{r,0} + k_{nr,0})$ gets modified to $k_{total}^{'} = (k_{r,0} + k_{nr,0} + k'_R + k_{ET}^{nr})$ when the QD is coupled to a metal NP. This modified total decay rate $k_{total}^{'}$ is always faster than $k_{total}^{0}$.This net change in decay rate becomes equal to $F_P$ and it can be expressed as $F_p = k_{total}^{'} / k_{total}^{0} = (k_{r,0} + k'_R)/k_{r,0}$ when we assume $k_{nr,0}$ and $k_{ET}^{nr}$ to be negligible. It is therefore necessary to consider all the different emission processes involved in a coupled QD-metal NP coupled system while understanding the complete picture of modified emission. The degree of plasmon-exciton coupling in MNP-QD systems depends on many factors, such as

interparticle distance, spectral overlap between the QD and the MNP, orientation of the electric dipole of the QDs relative to the MNP, as well as the topology of the metal surface.[73-77]

Although there have been numerous studies and reviews on the plasmonic effect on the emitting properties of QDs[78], it still remains challenging to build a quantitative relationship between the parameters mentioned above and the optical properties of the hybrid MNP-QD structures, due to the complexity of the system and the difficulty in precise control of the spatial geometry. Moreover, theoretical models need to be developed to calculate the absorption cross section, radiative/non-radiative rates, etc. to provide further insights into the fundamental mechanism of the plasmon-exciton interaction. To overcome these challenges, single particle studies are necessary, and a one-to-one MNP-to-QD conjugation system with well-defined geometry will be ideal for such studies. In this perspective, we intend to specifically focus on the research performed on single QDs situated close to plasmonic structures. We will provide a brief overview of the strategies developed and the challenges in the fabrication of the hybrid MNP-QD nanostructure. We will also discuss the plasmonic effect on photoluminescence blinking and exciton/biexciton emission statistics of single QDs, from both the experimental and theoretical point of view.

### *1.3.1. Synthesis of hybrid metal-semiconductor nanostructures*

Over the last decade, numerous synthetic strategies have been developed for fabricating hybrid MNP-QD nanostructures with well-controlled morphology and composition, in part due to the tremendous research effort in advancing nanoscale synthesis. A multi-component system composed of two or more disparate materials, like semiconductor and metal, which manifests

unique properties that often supersede the combined functionalities of the individual components. In order to obtain hybrid structures with desired optoelectronic properties, several factors including shape, size, orientation, and spatial geometry between the nano-constituents need to be considered while designing these hybrid materials.[79-80] In this section, we broadly classify the synthesis methods into two categories. One type of method relies on growing the metal (or semiconductor) component onto pre-synthesized semiconductor (or metal) nanocrystals. The other approach utilizes pre-fabricated metal and semiconductor nanocrystals as building blocks to form metal-semiconductor heterostructures by linking them with wet chemistry methods or by means of physical adsorption/forces.

Typically, one-dimensional hybrid metal-semiconductor heterostructures can be synthesized using multiple solution-based approaches. One of these methods pioneered by Banin's group involves site-selective deposition of metals (Au, Ag) onto the tips of pre-synthesized semiconductor nanocrystals in order to form segmented heterojunctions (see **Figure 1.7A** for the illustration and TEM image of Au-tipped CdS nanorods).[81-83] When excited by light, efficient charge separation occurs at the metal-semiconductor interface in these structures, making them efficient photocatalysts.[84] Another method is seed-mediated growth where metal nanocrystals serve as seeds, and one-dimensional growth of semiconductor domains occurs on specific crystal facets. Recently, our group reported a generalized seeded growth method by promoting an epitaxial growth of different metal chalcogenide (CdS, MnS, ZnS, CdSe) nanorods on Ag nanocrystal seeds. **Figure 1.7B** depicts the TEM image of Ag-CdSe hybrid metal-semiconductor nanorods. In addition to the one dimensional heterostructures, other solution-phase methods have been developed to grow metal@semiconductor core@shell nanomaterials (see **Figure 1.7C** for the

TEM image of Au@$Cu_2O$ NPs), via thermal or photo-induced heteroepitaxial nucleation and growth, hydrothermal synthesis, and aqueous phase oxidation.[85-87] In addition, Ouyang group have demonstrated a general thermodynamics driven non-epitaxial growth approach to synthesize various types of monocrystalline metal@semiconductor core@shell nanoparticles with precise control. The core@shell metal-based transition metal chalcogenides hold great promise in the fields of biomedical imaging, photothermal therapy, as well as photocatalytic and plasmon-enhanced spectroscopic applications. Nevertheless, it has always been a challenge to devise a single step, solution phase route for preparing metal@semiconductor core@shell heterojunctions because of the variable effect of ligands and solvents, lattice constant mismatch, presence of polar/non-polar facets, surface reactivity, and surface defects.

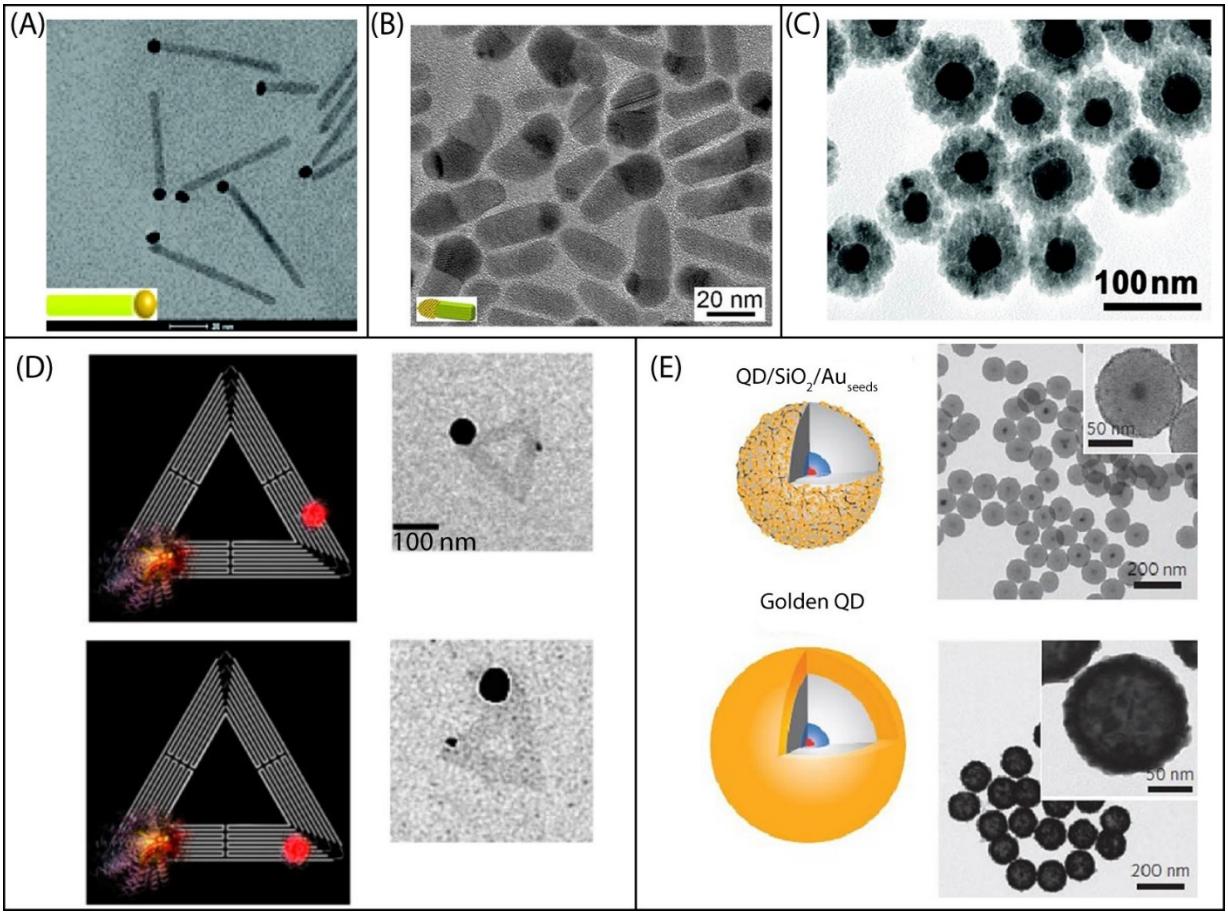


**Figure 1.7**. TEM images of hybrid metal-semiconductor nanostructures. (A) Au-tipped CdS nanorods. Scale bar =20 nm. (B) heteregenous Ag-CdSe nanorod (C) Au@$Cu_2O$ core@shell nanoparticles (D) schemes and corresponding TEM images of a Au NP and a QD assembled onto a triangle DNA origami with controlled spacing (E) Schematic representation and corresponding TEM images of QD/silica/Au seeds and QD/silica/Au nanoshell (termed as Golden QD) (A) Adapted with permission from Ref.42 © 2009 American Chemical Society (B) Reprinted with permission from Ref.44 © 2015 Royal Society of Chemistry (C) Adapted with permission from Ref.45 © 2011 American Chemical Society (D) Adapted with permission from Ref.54 © 2014

American Chemical Society (E) Reprinted with permission from Ref.62 © 2015 Macmillan Publishers Ltd. :*Nature Nanotechnology*.

In the heterostructures mentioned above, the metal and semiconductor domains are directly in contact, leading to significantly quenched photoluminescence of the semiconductor nanocrystal. To overcome this problem, various soft-chemical approaches (where reactions occur at ambient temperature) have been developed utilizing dielectric spacers to separate the metal and semiconductor components and to precisely control the interparticle distance.[65, 88-89] Different kinds of dielectric spacers have been used, for example, silica, polymers, DNA, and antigen-antibody pairs.[70, 88, 90-92] Specifically, work conducted by Liu et al.[90] and Naiki et al.[88] have reported multistep synthetic procedures of fabricating hybrid superstructures comprised of metal cores and dense layers of QDs separated by a silica shell of variable thickness. The surface of the metal NPs was modified with silica via a Stöber's reverse microemulsion method followed by specific adsorption of QDs onto amino-functionalized shells. Another method utilizes DNA origami as a template to assemble nanoscale objects, such as QDs and MNPs with high molecular precision. Reports from the groups of Yan and Liddle have demonstrated this to be a versatile platform allowing integration of different types of nanocrystals onto the same DNA origami scaffold.[93-97] For examples, **Figure 1.7D** shows the design and TEM images of one Au NP and a single QD attached onto the same triangle DNA origami with controlled interparticle spacing. Not only has DNA been used as a spacer, Lee et al. have shown that derivatives of PEG (polyethylene glycol) and NHS (N-hydroxysulfosuccinimide) have been utilized as polymer linkers to create conjugates consisted of Au NPs and CdTe QDs.[98]

Assembly of the MNPs and QDs with molecular linkers can either maintain or enhance the PL of the QDs. However, the resultant hybrid structures are relatively large in size, making them difficult to be applied as fluorescence probes, especially for biological applications. Thus, it is desired to build a more compact plasmonic/fluorescent system. In contrast to the previously described solution-based techniques of growing metal-core@semiconductor-shell systems, Jin et al.[99] and Karan et al.[100] have developed a method to grow ultrathin Au-shell around silica-encapsulated QDs based on a charged peptide-template approach. Similarly, Ji et al. have synthesized a hybrid QD/silica/gold nanoshell structure with a much thicker silica spacer and continuous gold shell around the QDs.[101] **Figure 1.7E** illustrates the schemes and TEM images of the QD/silica/Au seeds and QD/silica/Au nanoshell, respectively. The QD@silica@Au core@shell NPs exhibit stable and enhanced emission, and also provide plasmonic signatures that can be used for photo-thermal therapy.

Despite the current achievements in fabricating hybrid MNP-QD structures as mentioned above, tremendous challenges still continue to exist in understanding the complex interplay between the surfactants and the metal/semiconductor interfaces, which provides the main driving force for the self-organization during assembly. Moreover, the attachment of MNPs to QDs with controlled ratios, specifically one-to-one attachment, is especially difficult. Current methods often suggest that the assembly take place in an aqueous solution, which is not the native medium for high quality QDs, adding extra complexity to the synthesis. As an alternative approach, seed-mediated growth employing QDs as seeds to grow on the metal component, while controlling the geometry and composition may be a new direction to pursue.

### *1.3.2. Plasmonic effect on single QD PL blinking and lifetime*

Previous research has demonstrated that a nanostructured metal surface can modify the emitting properties of nearby fluorophores. More than a decade ago, Shimizu et al. reported a drastic enhancement in the radiative rate (~ 70 fold) and nonradiative rate (~ 1400 fold) of single QDs close to roughened metal surfaces at low temperature (10 K).[102] Despite the fact that the presence of the metal surface led to a lower apparent quantum yield of the QD, the overall emission intensity of the QD increased due to the enhancement from the metal surface. In addition to PL intensity for single QDs, both PL intensity intermittency ("blinking") and lifetime of the QD are subject to change when they are placed in close proximity to MNPs or metal surfaces. Although the reason why single QDs exhibit PL blinking still remains controversial, the blinking phenomenon is found to be largely reduced when QD are near plasmonic structures. For example, Tang's group reported that when single QDs were close to Ag nanoprisms or Ag nanocubes, they exhibited a significant PL enhancement accompanied by weak PL intensity fluctuation.[103-104] **Figure 1.8A** shows the schematic representation of the samples with corresponding emission traces and lifetime decay profiles of single QDs on glass and on Ag nanoprisms, respectively. A similar change in PL behavior of single QDs was observed by Ma et al. when a single QD was attached to a silica-coated Au NP or when a single silica-coated QD was close to Au NPs.[105-106] **Figure 1.8B** illustrates the PL blinking traces and lifetimes of a silica-coated QD on two different Au NP substrates with plasmon resonances at 526 and 590 nm. Compared to the isolated QDs in the absence of the Au NPs, those close to the Au NP exhibited enhanced on-state PL intensity (also increased on-time fractions) with a significant reduction in PL lifetime.

Changes in PL intensity and lifetime have also been reported earlier by Samanta et al. when an Au NP and a QD were assembled onto the same DNA origami construct.[94] A long range (> 50

nm) PL quenching of the QDs was observed, unlike conventional Förster resonance energy transfer and charge transfer processes which occur when the fluorophore is very close to the quencher (usually less than 10 nm). The long-range quenching phenomenon was suggested to be caused by the non-radiative decay channels induced by the nearby Au NPs. As a collective result of enhancement in the excitation rates and overall modification of PL quantum yield, these studies proved that there was a significant change in the emission behavior of single QDs when they were in close proximity to plasmonic substrates.

Apart from these studies, several other groups have also observed a similar change in the emission behavior of single QDs when they were coupled onto thin films fabricated from randomly deposited Au or Ag nanoparticles.[107-108] In another work by Canesson et al., "giant" shell CdSe/CdS QDs were directly deposited on a gold film, which created the strong Purcell effect that resulted in almost complete suppression of blinking.[109] Recently, Ji et al.[101] have also showed that when a single QD was encapsulated by a continuous Au nanoshell, there was a significant reduction in the emission intensity fluctuation giving rise to an almost "non-blinking" QD (see **Figure 1.8C** for the blinking traces and PL decays). In the QD/silica/Au NP, the spontaneous emission rate of the encapsulated QDs was highly increased due to the Purcell effect from the Au nanoshell resonator, and the competing non-radiative Auger relaxation became negligible. In addition to wet-chemistry methods, precise manipulation of distance between a single MNP and a single QD has been realized in some studies using scanning probe microscopic techniques implementing AFM probes and optical tweezers.[110-114] For instance, Meixner's and Li's groups have introduced self-aligned scanning probe methods for proper positioning (with lateral accuracy of 10 nm) of single QDs onto Au NPs to investigate the near-field plasmonic effect on the emission

behavior of single QDs.[110-111] Again, optical studies performed on the hybrid system showed enhanced emission and change in the blinking behavior of single QDs close to the MNPs.

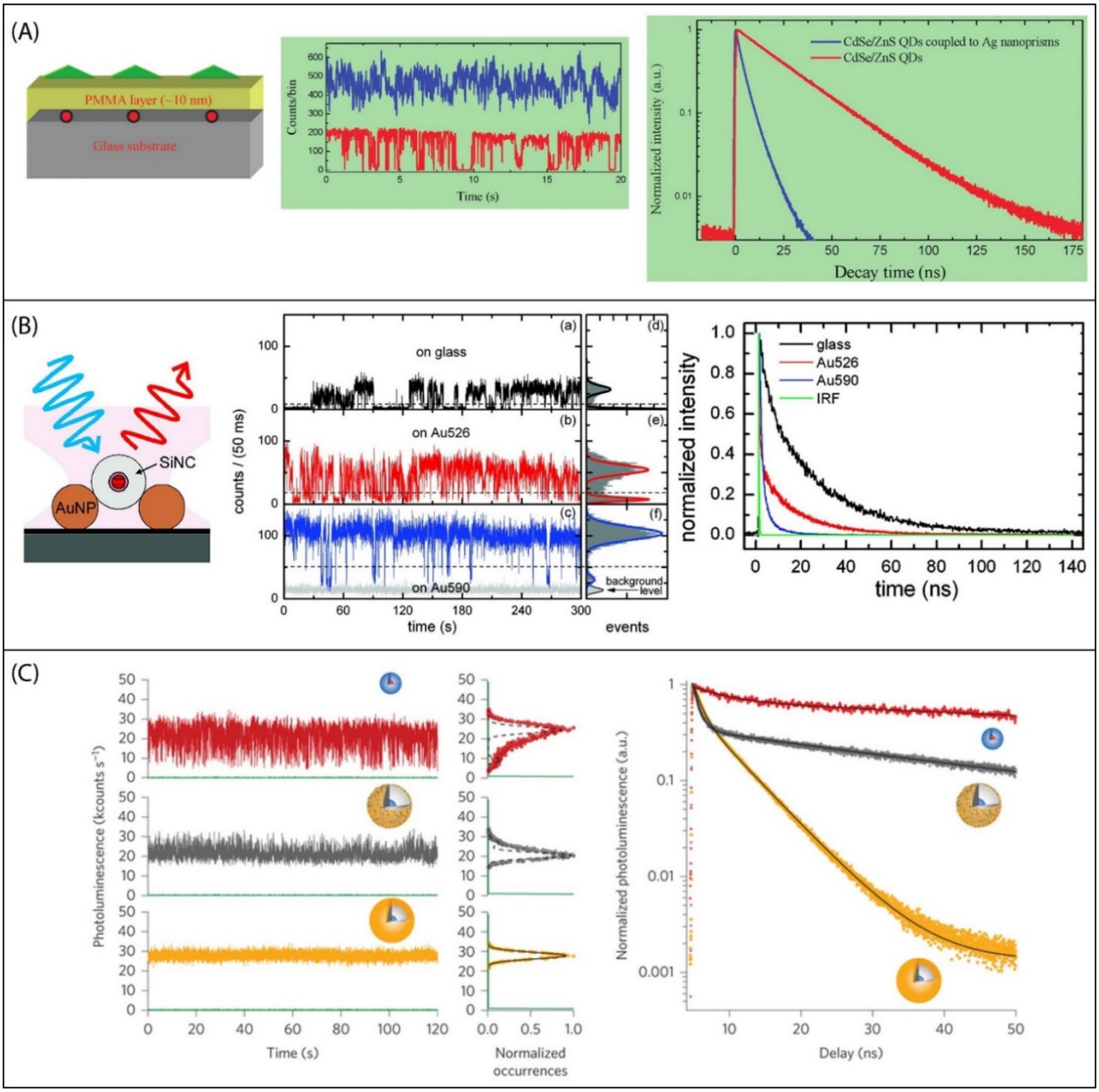


**Figure 1.8**. (A) Sketch of sample configuration of CdSe/ZnS QDs coupled to Ag nanoprisms, PL intensity time traces (10 ms binning time) and time-dependent PL decays of single QDs on glass (red) and on Ag nanoprisms (blue). (B) Schematic of the sample, emission traces (a,b,c) and

corresponding intensity distributions (d,e,f) and lifetime decay profiles of single QD on glass, Au 526 and Au 590 substrate, respectively. Binning time is 50 ms and dashed lines in the emission trace plots represent the "on"/"off" threshold. (C) Left: Fluorescence intensity time traces (binning time = 10 ms) and corresponding intensity distributions of single CdSe/CdS QDs (red), QD/silica/Au seeds (gray) and Golden QDs (orange). Right: Corresponding fluorescence decays of the three-different type of nanoparticles. (A) Adapted with permission from Ref.64 © 2009 American Chemical Society (B) Adapted with permission from Ref.67 © 2010 American Chemical Society (C) Adapted with permission from Ref.62 © 2015 Macmillan Publishers Ltd: *Nature Nanotechnology*.

### *1.3.3. Plasmonic effect on multiexciton emission of single QDs*

Multiple studies on the effect of plasmon on QD emission focus on the change in PL intensity of the QDs. However, the plasmonic effect on multiexciton emission of single QDs is rarely investigated, largely due to the lack of a proper method to measure the single QD multiexciton emission efficiency. In 2011, Nair et al.[33] developed a method based on second-order photon intensity correlation ($g^{(2)}(\tau)$ function) to determine the biexciton quantum yield of individual QDs. Using time-dependent photon statistics under the low excitation regime, the ratio of biexciton to exciton quantum yields of single QDs can be readily determined from the relative size of the 0-time $g^{(2)}$ peak. The quantum yield of higher order excitons are usually low due to effective and fast (on the order of few hundred picoseconds) non-radiative Auger recombination

processes. Thus, exploiting plasmon coupling to generate multiexciton emission from single QDs has induced a significant amount of interest. Enhancement in the multiexcitonic quantum yield from single QDs has been recently observed in quite a few studies when the QDs were coupled to roughened metallic films.[107-109] For instance, LeBlanc et al. observed enhanced multiphoton emission and, at the same time, decreased single photon emission of individual QDs when they were deposited on a roughened Au film.[107] As shown in **Figure 1.9A**, the representative photon correlation histograms of three individual QDs near the Au film have very high 0-time peak of the $g^{(2)}$ function compared to the ones on the poly(methyl methacrylate) (PMMA) film. The origin of the phenomenon was explained as that the surface plasmon modes of the Au film greatly enhanced the radiative rate of biexciton, making it much faster than that of the single exciton, thereby effectively increasing the biexciton quantum yield. In another work by Park et al, the transition in the photon emission behavior of single QDs from sub-Poissonian (incomplete antibunching) to super-Poissonian (strong bunching) statistics was observed when they were coupled to a film of Ag nanoflakes.[108] As depicted in **Figure 1.9B**, the $g^{(2)}$ function of single QD deposited on rough Ag surface has a 0-time peak higher than the side peaks, where that of the single QD on quartz has the reverse trend. In this system, both the single exciton and biexciton emission was quenched by the metal surface. Nevertheless, the quantum yield of biexciton became higher than that of the exciton, making the emitted photons "bunched". The authors suggested that photon bunching may be a result of new non-radiative recombination pathways involving defect states produced at the metal-ligand or metal-QD interface. Increased multiexciton emission was also observed earlier by Masuo and co-workers when single CdSe/ZnS core/shell QDs interacted with Ag NPs[115] (see **Figure 1.9C**). Although the radiative relaxation and non-radiative Auger recombination processes

compete with each other in the presence of Ag NPs, the probability of multiphoton emission increases when the fast radiative recombination dominates the multiexciton relaxation process.

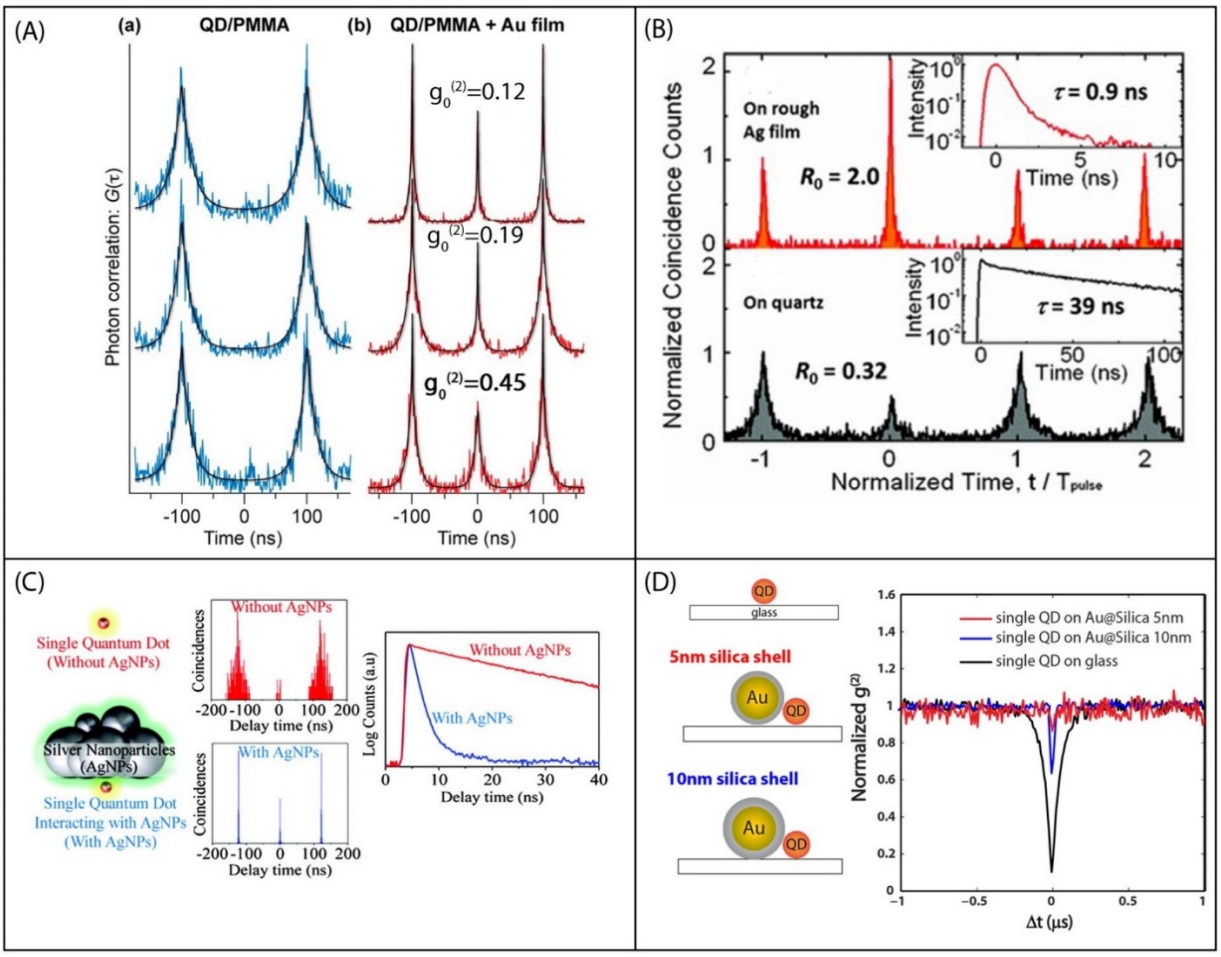


**Figure 1.9**. (A) Representative photon correlation histograms of three single QDs on PMMA and on PMMA near gold film. (B) Normalized $g^{(2)}$ functions and lifetime decay plots (insets) of single CdSe/ZnS QDs dispersed on rough Ag film and on quartz substrate, respectively (C) Schematic, photon correlation histograms and fluorescence decay profiles of single QDs with and without Ag NPs. (D) Schematic of the substrates and representative normalized $g^{(2)}$ data of single QDs on glass and on Au@silica (5 nm and 10 nm silica shell thickness) substrates. (A) Adapted with permission from Ref.68 © 2013 American Chemical Society (B) Adapted with permission from Ref.69 ©

2013 American Physical Society (C) Adapted with permission from Ref.78 © 2011 American Chemical Society.

However, most of these studies were performed on thin metallic films, which do not have well-defined geometry and plasmon band. Lack of such control makes it difficult to study the mechanisms causing the change in multiexciton emission efficiency. In addition to this, theoretical models explaining the change in the quantum yields of exciton and multiexcitons were lacking in these studies. Thus, an in-depth, quantitative explanation behind exciton-plasmon interaction is still required to understand the dynamics of biexcitons. Recently, our group has performed a mechanistic investigation of the biexcitonic quantum yield enhancement of single QDs near $Au@SiO_2$ NPs.[116] From the $g^{(2)}(\tau)$ data, we observed a significant increase in the biexciton/exciton quantum yield ratio of single QDs on an Au NP substrate (**Figure 1.9D**). An electrodynamics model was developed to calculate the change in emission intensity, quantum yield, and lifetimes of exciton and biexciton as a result of the exciton-plasmon coupling. This model was used earlier by Zou and co-workers to study the effect of MNPs on the lifetime and emission intensity of a nearby dye molecule and was adapted for QDs.[117] When applying this model to our system, we found that not only the relative position of the QDs with respect to Au NPs can impact the QD emission, but also the orientation of the electric field can regulate the emission properties of the exciton and biexciton.

### *1.3.4. Theoretical modeling of the exciton/multiexciton recombination mechanism in the QD-MNP system*

In contrast to the remarkable experimental effort devoted to studying exciton-plasmon interaction, theoretical studies on this topic are rather limited. Fortunately, ever since the 1970s, theoretical models have been developed on the radiative and nonradiative relaxation of molecules in close proximity to metal surfaces/nanoparticles.[118-121] In these models, the excited molecule is often treated as an oscillating dipole with resonance at the molecular transition frequency. By solving Maxwell's equations, the radiative rate of the system (molecule and the MNP) is found to be proportional to the square of the magnitude of the total dipole moment, while the rate of the nonradiative energy transfer between the molecule and the particle is determined by the integral of the local electric field intensity over the particle volume.[122] In these systems, both the total radiative and non-radiative relaxation rates can be enhanced compared to the isolated molecule. Whether the fluorescence of the molecule gets enhanced or quenched depends on many factors, such as particle size and composition, spectral overlap, excitation wavelength, the distance between the molecule and the particle, and orientation of the molecule relative to the metal surface. It is worth noting that the "surface energy transfer" efficiency between the molecule and the MNP has $R^{-x}$ (x=2-4) molecule-to-metal distance dependence, while that for Förster resonance energy transfer between small molecules follows $R^{-6}$ dependence.[93, 123]

When considering exciton relaxation in hybrid QD-MNP systems, similar models can be applied. In the study by Samanta et al., the fluorescence quenching of a single QD by Au NP was found to have ~ $R^{-3}$ dependence, where R is the distance between the QD and Au NP, controlled by DNA linkers.[93] The discrepancy between the theory and experiments suggests that QDs are not

as simple as small molecules. When dealing with QDs, the surface and internal structure of the QDs should be considered, which can significantly affect their fluorescent properties. The ligands and surface of the QDs may interact with the MNPs, giving rise to new non-radiative decay channels, as suggested by several experimental studies.[108, 124] Moreover, the density of states of the QDs is much higher than that of molecules. The "hot exciton" in the QDs may directly interact with the plasmon-induced "hot electrons". Another factor that complicates the picture is that when core/shell QDs are used, the delocalization of the electron and hole wave functions should be considered. In other words, QDs are much more complex than molecules and the model that is developed for molecules needs to be modified for QDs.

Compared to the single exciton, it is more challenging to model the multiexciton (n excitons) relaxation processes in QD-MNP conjugates, which do not exist in the molecule-MNP model. To generate multiexcitons in a QD, multiple photons need to be absorbed. Assuming the absorption events are independent, we expect the excitation to be enhanced by $|E|^{2n}$, where $|E|^2$ is enhancement in the square of the magnitude of the electric field around the MNP, and n is the number of excitons (e.g., n=2 for biexciton). This idea has been applied to our recent study to explain biexciton emission enhancement of single QDs close to Au@$SiO_2$ NPs. When considering the relaxation of n excitons in the QD, the intrinsic non-radiative decay rate is a lot faster than that of the single exciton due to the fast Auger rate. Thus, the plasmonic effect on the relaxation of the biexciton or higher order excitons is different from that on the single exciton. Our group and several others have shown that the non-radiative energy transfer between QD and MNPs reduces the exciton emission much more than biexciton emission.[108, 116] Moreover, to calculate the relaxation rate of the n-th exciton of the QD in the presence of the MNP, more factors need to be

considered; for example, the interaction between the higher order exciton and hot electrons, and the competing thermal and Auger relaxations. The complex metal-ligands-semiconductor interaction requires both theoretical and experimental studies to elucidate the multiexciton relaxation mechanism in QD-MNP systems.

## 1.4. Conclusions

Manipulation of exciton/multiexciton emission efficiency of QDs by plasmonic structures has been demonstrated to be successful. This not only complements the endeavor in perfecting QD synthesis to obtain QDs with high emission efficiency, but also brings new optical behaviors beyond the intrinsic properties of the QDs. However, further effort is still needed to better understand the hybrid excitonic/plasmonic nanosystems, such as what regulates the strength of exciton-plasmon interaction, how new recombination pathways are formed in the hybrid structures, what the relationship is between the structure and the properties. New synthetic methods, time-resolved optical spectroscopies and theoretical modeling are the key to answer these questions. With a profound understanding of the fundamental physical processes, the hybrid metal/semiconductor nanomaterials are able to transform many areas including quantum communication, photocatalysis, and optoelectronic devices.

## 1.5. References


1. Michler, P.; Kiraz, A.; Becher, C.; Schoenfeld, W. V.; Petroff, P. M.; Zhang, L.; Hu, E.; Imamoglu, A., A Quantum Dot Single-Photon Turnstile Device. *Science* **2000,** *290* (5500), 2282-2285.
2. Moreau, E.; Robert, I.; Manin, L.; Thierry-Mieg, V.; Gérard, J. M.; Abram, I., Quantum Cascade of Photons in Semiconductor Quantum Dots. *Phys. Rev. Lett.* **2001,** *87* (18), 183601.
3. Bayer, M.; Reinecke, T. L.; Weidner, F.; Larionov, A.; McDonald, A.; Forchel, A., Inhibition and Enhancement of the Spontaneous Emission of Quantum Dots in Structured Microresonators. *Phys. Rev. Lett.* **2001,** *86* (14), 3168-3171.
4. Santori, C.; Fattal, D.; Pelton, M.; Solomon, G. S.; Yamamoto, Y., Polarization-correlated photon pairs from a single quantum dot. *Phys. Rev. B* **2002,** *66* (4), 045308.
5. Stevenson, R. M.; Thompson, R. M.; Shields, A. J.; Farrer, I.; Kardynal, B. E.; Ritchie, D. A.; Pepper, M., Quantum dots as a photon source for passive quantum key encoding. *Phys. Rev. B* **2002,** *66* (8), 081302.
6. Regelman, D. V.; Mizrahi, U.; Gershoni, D.; Ehrenfreund, E.; Schoenfeld, W. V.; Petroff, P. M., Semiconductor Quantum Dot: A Quantum Light Source of Multicolor Photons with Tunable Statistics. *Phys. Rev. Lett.* **2001,** *87* (25), 257401.
7. Michler, P.; Imamoglu, A.; Mason, M. D.; Carson, P. J.; Strouse, G. F.; Buratto, S. K., Quantum correlation among photons from a single quantum dot at room temperature. *Nature* **2000,** *406* (6799), 968-970.
8. Shields, A. J., Semiconductor quantum light sources. *Nat. Photon.* **2007,** *1* (4), 215-223.
9. Gisin, N.; Ribordy, G.; Tittel, W.; Zbinden, H., Quantum cryptography. *Rev. Mod. Phys.* **2002,** *74* (1), 145-195.
10. Bouwmeester, D.; Pan, J.-W.; Mattle, K.; Eibl, M.; Weinfurter, H.; Zeilinger, A., Experimental quantum teleportation. *Nature* **1997,** *390* (6660), 575-579.
11. Waks, E.; Inoue, K.; Santori, C.; Fattal, D.; Vuckovic, J.; Solomon, G. S.; Yamamoto, Y., Secure communication: Quantum cryptography with a photon turnstile. *Nature* **2002,** *420* (6917), 762-762.
12. Sonia, B.; Kelley, R.; Jelena, V., Engineered quantum dot single-photon sources. *Rep. Prog. Phys.* **2012,** *75* (12), 126503.
13. Breitenbach, G.; Schiller, S.; Mlynek, J., Measurement of the quantum states of squeezed light. *Nature* **1997,** *387* (6632), 471-475.
14. SomaschiN; GieszV; De Santis, L.; Loredo, J. C.; Almeida, M. P.; HorneckerG; Portalupi, S. L.; GrangeT; AntónC; DemoryJ; GómezC; SagnesI; Lanzillotti-Kimura, N. D.; LemaítreA; AuffevesA; White, A. G.; LancoL; SenellartP, Near-optimal single-photon sources in the solid state. *Nat. Photon.* **2016,** *10* (5), 340-345.
15. Glauber, R. J., Coherent and Incoherent States of the Radiation Field. *Phys. Rev.* **1963,** *131* (6), 2766-2788.
16. Davidovich, L., Sub-Poissonian processes in quantum optics. *Rev. Mod. Phys.* **1996,** *68* (1), 127-173.
17. Brahim, L.; Michel, O., Single-photon sources. *Rep. Prog. Phys.* **2005,** *68* (5), 1129.
18. Basché, T.; Moerner, W. E.; Orrit, M.; Talon, H., Photon antibunching in the fluorescence of a single dye molecule trapped in a solid. *Phys. Rev. Lett.* **1992,** *69* (10), 1516-1519.
19. Kurtsiefer, C.; Mayer, S.; Zarda, P.; Weinfurter, H., Stable Solid-State Source of Single Photons. *Phys. Rev. Lett.* **2000,** *85* (2), 290-293.

20. Shigeki, T., Recent progress in single-photon and entangled-photon generation and applications. *Jap.J. Appl. Phys.* **2014,** *53* (3), 030101.
21. Cui, J.; Beyler, A. P.; Bischof, T. S.; Wilson, M. W. B.; Bawendi, M. G., Deconstructing the photon stream from single nanocrystals: from binning to correlation. *Chem. Soc. Rev.* **2014,** *43* (4), 1287-1310.
22. Kiraz, A.; Fälth, S.; Becher, C.; Gayral, B.; Schoenfeld, W. V.; Petroff, P. M.; Zhang, L.; Hu, E.; Imamoğlu, A., Photon correlation spectroscopy of a single quantum dot. *Phys. Rev. B* **2002,** *65* (16), 161303.
23. Zou, X. T.; Mandel, L., Photon-antibunching and sub-Poissonian photon statistics. *Phys. Rev. A* **1990,** *41* (1), 475-476.
24. Brown, R. H.; Twiss, R. Q., Interferometry of the Intensity Fluctuations in Light. I. Basic Theory: The Correlation between Photons in Coherent Beams of Radiation. *Proc. Royal Society of London. Series A. Mathematical and Physical Sciences* **1957,** *242* (1230), 300.
25. Brown, R. H.; Twiss, R. Q., Interferometry of the Intensity Fluctuations in Light II. An Experimental Test of the Theory for Partially Coherent Light. *Proc. Royal Society of London. Series A. Mathematical and Physical Sciences* **1958,** *243* (1234), 291.
26. Kimble, H. J.; Dagenais, M.; Mandel, L., Photon Antibunching in Resonance Fluorescence. *Phys. Rev. Lett.* **1977,** *39* (11), 691-695.
27. Lippitz, M.; Kulzer, F.; Orrit, M., Statistical Evaluation of Single Nano-Object Fluorescence. *Chem.Phys.Chem.* **2005,** *6* (5), 770-789.
28. Orrit, M., Photon statistics in the fluorescence of single molecules and nanocrystals: Correlation functions versus distributions of on- and off-times. *J. Chem. Phys.* **2003,** *119* (4), 2214-2222.
29. Fleury, L.; Segura, J. M.; Zumofen, G.; Hecht, B.; Wild, U. P., Nonclassical Photon Statistics in Single-Molecule Fluorescence at Room Temperature. *Phys. Rev. Lett.* **2000,** *84* (6), 1148-1151.
30. Lounis, B.; Bechtel, H. A.; Gerion, D.; Alivisatos, P.; Moerner, W. E., Photon antibunching in single CdSe/ZnS quantum dot fluorescence. *Chem. Phys. Lett.* **2000,** *329* (5–6), 399-404.
31. Lounis, B.; Moerner, W. E., Single photons on demand from a single molecule at room temperature. *Nature* **2000,** *407* (6803), 491-493.
32. Santori, C.; Pelton, M.; Solomon, G.; Dale, Y.; Yamamoto, Y., Triggered Single Photons from a Quantum Dot. *Phys. Rev. Lett.* **2001,** *86* (8), 1502-1505.
33. Nair, G.; Zhao, J.; Bawendi, M. G., Biexciton Quantum Yield of Single Semiconductor Nanocrystals from Photon Statistics. *Nano Lett.* **2011,** *11* (3), 1136-1140.
34. Zwiller, V.; Jonsson, P.; Blom, H.; Jeppesen, S.; Pistol, M.-E.; Samuelson, L.; Katznelson, A. A.; Kotelnikov, E. Y.; Evtikhiev, V.; Björk, G., Correlation spectroscopy of excitons and biexcitons on a single quantum dot. *Phys. Rev. A* **2002,** *66* (5), 053814.
35. Alivisatos, A. P., Semiconductor Clusters, Nanocrystals, and Quantum Dots. *Science* **1996,** *271* (5251), 933.
36. Nirmal, M.; Dabbousi, B. O.; Bawendi, M. G.; Macklin, J. J.; Trautman, J. K.; Harris, T. D.; Brus, L. E., Fluorescence intermittency in single cadmium selenide nanocrystals. *Nature* **1996,** *383* (6603), 802-804.
37. M. Kuno, D. P. F., H. F. Hamann, A. Gallagher, D. J. Nesbitt, Nonexponential "blinking" kinetics of single CdSe quantum dots: A universal power law behavior. *J. Chem. Phys.* **2000,** *112* (7), 3117-3120.

38. M. Kuno, D. P. F., H. F. Hamann, A. Gallagher, D. J. Nesbitt, "On"/"off" fluorescence intermittency of single semiconductor quantum dots. *J. Chem. Phys.* **2001,** *115* (2), 1028-1040.
39. Kuno, M.; Fromm, D. P.; Johnson, S. T.; Gallagher, A.; Nesbitt, D. J., Modeling distributed kinetics in isolated semiconductor quantum dots. *Phys. Rev. B* **2003,** *67* (12), 125304.
40. Crouch, C. H.; Sauter, O.; Wu, X.; Purcell, R.; Querner, C.; Drndic, M.; Pelton, M., Facts and Artifacts in the Blinking Statistics of Semiconductor Nanocrystals. *Nano Lett.* **2010,** *10* (5), 1692-1698.
41. Osborne, M. A.; Fisher, A. A. E., Charge-tunnelling and self-trapping: common origins for blinking, grey-state emission and photoluminescence enhancement in semiconductor quantum dots. *Nanoscale* **2016,** *8* (17), 9272-9283.
42. Efros, A. L.; Nesbitt, D. J., Origin and control of blinking in quantum dots. *Nat. Nano.* **2016,** *11* (8), 661-671.
43. Galland, C.; Ghosh, Y.; Steinbruck, A.; Sykora, M.; Hollingsworth, J. A.; Klimov, V. I.; Htoon, H., Two types of luminescence blinking revealed by spectroelectrochemistry of single quantum dots. *Nature* **2011,** *479* (7372), 203-207.
44. Galland, C.; Ghosh, Y.; Steinbrück, A.; Hollingsworth, J. A.; Htoon, H.; Klimov, V. I., Lifetime blinking in nonblinking nanocrystal quantum dots. *Nat. Commun.* **2012,** *3*, 908.
45. Peterson, J. J.; Nesbitt, D. J., Modified Power Law Behavior in Quantum Dot Blinking: A Novel Role for Biexcitons and Auger Ionization. *Nano Lett.* **2009,** *9* (1), 338-345.
46. Ye, M.; Searson, P. C., Blinking in quantum dots: The origin of the grey state and power law statistics. *Phys. Rev. B* **2011,** *84* (12), 125317.
47. Cordones, A. A.; Bixby, T. J.; Leone, S. R., Evidence for Multiple Trapping Mechanisms in Single CdSe/ZnS Quantum Dots from Fluorescence Intermittency Measurements over a Wide Range of Excitation Intensities. *J. Phys. Chem. C* **2011,** *115* (14), 6341-6349.
48. Koenderink, A. F.; Alù, A.; Polman, A., Nanophotonics: Shrinking light-based technology. *Science* **2015,** *348* (6234), 516.
49. Fratalocchi, A., Nano-optics gets practical. *Nat. Nano.* **2015,** *10* (1), 11-15.
50. Krenn, J. R., Nanoparticle waveguides: Watching energy transfer. *Nat. Mater.* **2003,** *2* (4), 210-211.
51. Barnes, W. L.; Dereux, A.; Ebbesen, T. W., Surface plasmon subwavelength optics. *Nature* **2003,** *424* (6950), 824-830.
52. Yan, R.; Gargas, D.; Yang, P., Nanowire photonics. *Nat. Photon.* **2009,** *3* (10), 569-576.
53. Kwon, S.-H.; Kang, J.-H.; Seassal, C.; Kim, S.-K.; Regreny, P.; Lee, Y.-H.; Lieber, C. M.; Park, H.-G., Subwavelength Plasmonic Lasing from a Semiconductor Nanodisk with Silver Nanopan Cavity. *Nano Lett.* **2010,** *10* (9), 3679-3683.
54. Mizaikoff, B., Waveguide-enhanced mid-infrared chem/bio sensors. *Chem. Soc. Rev.* **2013,** *42* (22), 8683-8699.
55. Schuller, J. A.; Barnard, E. S.; Cai, W.; Jun, Y. C.; White, J. S.; Brongersma, M. L., Plasmonics for extreme light concentration and manipulation. *Nat. Mater.* **2010,** *9* (3), 193-204.
56. Anker, J. N.; Hall, W. P.; Lyandres, O.; Shah, N. C.; Zhao, J.; Van Duyne, R. P., Biosensing with plasmonic nanosensors. *Nat. Mater.* **2008,** *7* (6), 442-453.
57. Green, M. A.; Pillai, S., Harnessing plasmonics for solar cells. *Nat. Photon.* **2012,** *6* (3), 130-132.
58. Pelton, M., Modified spontaneous emission in nanophotonic structures. *Nat. Photon.* **2015,** *9* (7), 427-435.

59. Zhao, W.-W.; Yu, P.-P.; Shan, Y.; Wang, J.; Xu, J.-J.; Chen, H.-Y., Exciton-Plasmon Interactions between CdS Quantum Dots and Ag Nanoparticles in Photoelectrochemical System and Its Biosensing Application. *Anal. Chem.* **2012,** *84* (14), 5892-5897.
60. Zhou, N.; Yuan, M.; Gao, Y.; Li, D.; Yang, D., Silver Nanoshell Plasmonically Controlled Emission of Semiconductor Quantum Dots in the Strong Coupling Regime. *ACS Nano* **2016,** *10* (4), 4154-4163.
61. Tam, F.; Goodrich, G. P.; Johnson, B. R.; Halas, N. J., Plasmonic Enhancement of Molecular Fluorescence. *Nano Lett.* **2007,** *7* (2), 496-501.
62. Vasa, P.; Pomraenke, R.; Schwieger, S.; Mazur, Y. I.; Kunets, V.; Srinivasan, P.; Johnson, E.; Kihm, J. E.; Kim, D. S.; Runge, E.; Salamo, G.; Lienau, C., Coherent Exciton-Surface-Plasmon-Polariton Interaction in Hybrid Metal-Semiconductor Nanostructures. *Phys. Rev. Lett.* **2008,** *101* (11), 116801.
63. Cohen-Hoshen, E.; Bryant, G. W.; Pinkas, I.; Sperling, J.; Bar-Joseph, I., Exciton–Plasmon Interactions in Quantum Dot–Gold Nanoparticle Structures. *Nano Lett.* **2012,** *12* (8), 4260-4264.
64. Ackerman, P. J.; Mundoor, H.; Smalyukh, I. I.; van de Lagemaat, J., Plasmon–Exciton Interactions Probed Using Spatial Coentrapment of Nanoparticles by Topological Singularities. *ACS Nano* **2015,** *9* (12), 12392-12400.
65. Fedutik, Y.; Temnov, V.; Woggon, U.; Ustinovich, E.; Artemyev, M., Exciton−Plasmon Interaction in a Composite Metal−Insulator−Semiconductor Nanowire System. *J. Am. Chem. Soc.* **2007,** *129* (48), 14939-14945.
66. Ozel, T.; Hernandez-Martinez, P. L.; Mutlugun, E.; Akin, O.; Nizamoglu, S.; Ozel, I. O.; Zhang, Q.; Xiong, Q.; Demir, H. V., Observation of Selective Plasmon-Exciton Coupling in Nonradiative Energy Transfer: Donor-Selective versus Acceptor-Selective Plexcitons. *Nano Lett.* **2013,** *13* (7), 3065-3072.
67. Wei, H.; Ratchford, D.; Li, X.; Xu, H.; Shih, C.-K., Propagating Surface Plasmon Induced Photon Emission from Quantum Dots. *Nano Lett.* **2009,** *9* (12), 4168-4171.
68. Song, M.; Wu, B.; Chen, G.; Liu, Y.; Ci, X.; Wu, E.; Zeng, H., Photoluminescence Plasmonic Enhancement of Single Quantum Dots Coupled to Gold Microplates. *J. Phys. Chem. C* **2014,** *118* (16), 8514-8520.
69. Chen, H.; Xia, Y., Compact Hybrid (Gold Nanodendrite-Quantum Dots) Assembly: Plasmon Enhanced Fluorescence-Based Platform for Small Molecule Sensing in Solution. *Anal. Chem.* **2014,** *86* (22), 11062-11069.
70. Pons, T.; Medintz, I. L.; Sapsford, K. E.; Higashiya, S.; Grimes, A. F.; English, D. S.; Mattoussi, H., On the Quenching of Semiconductor Quantum Dot Photoluminescence by Proximal Gold Nanoparticles. *Nano Lett.* **2007,** *7* (10), 3157-3164.
71. Marinica, D. C.; Lourenço-Martins, H.; Aizpurua, J.; Borisov, A. G., Plexciton Quenching by Resonant Electron Transfer from Quantum Emitter to Metallic Nanoantenna. *Nano Lett.* **2013,** *13* (12), 5972-5978.
72. Fu, Y.; Zhang, J.; Lakowicz, J. R., Silver-enhanced fluorescence emission of single quantum dot nanocomposites. *Chem. Commun.* **2009,** (3), 313-315.
73. Jin, S.; DeMarco, E.; Pellin, M. J.; Farha, O. K.; Wiederrecht, G. P.; Hupp, J. T., Distance-Engineered Plasmon-Enhanced Light Harvesting in CdSe Quantum Dots. *J. Phys. Chem. Lett.* **2013,** *4* (20), 3527-3533.
74. Chen, Y.; Munechika, K.; Ginger, D. S., Dependence of Fluorescence Intensity on the Spectral Overlap between Fluorophores and Plasmon Resonant Single Silver Nanoparticles. *Nano Lett.* **2007,** *7* (3), 690-696.

75. Zhang, X.; Marocico, C. A.; Lunz, M.; Gerard, V. A.; Gun'ko, Y. K.; Lesnyak, V.; Gaponik, N.; Susha, A. S.; Rogach, A. L.; Bradley, A. L., Experimental and Theoretical Investigation of the Distance Dependence of Localized Surface Plasmon Coupled Förster Resonance Energy Transfer. *ACS Nano* **2014,** *8* (2), 1273-1283.
76. Munechika, K.; Chen, Y.; Tillack, A. F.; Kulkarni, A. P.; Plante, I. J.-L.; Munro, A. M.; Ginger, D. S., Spectral Control of Plasmonic Emission Enhancement from Quantum Dots near Single Silver Nanoprisms. *Nano Lett.* **2010,** *10* (7), 2598-2603.
77. Govorov, A. O.; Bryant, G. W.; Zhang, W.; Skeini, T.; Lee, J.; Kotov, N. A.; Slocik, J. M.; Naik, R. R., Exciton−Plasmon Interaction and Hybrid Excitons in Semiconductor−Metal Nanoparticle Assemblies. *Nano Lett.* **2006,** *6* (5), 984-994.
78. Achermann, M., Exciton−Plasmon Interactions in Metal−Semiconductor Nanostructures. *J. Phys. Chem. Lett.* **2010,** *1* (19), 2837-2843.
79. Banin, U.; Ben-Shahar, Y.; Vinokurov, K., Hybrid Semiconductor–Metal Nanoparticles: From Architecture to Function. *Chem. Mater.* **2014,** *26* (1), 97-110.
80. Feng, X.; Hu, G.; Hu, J., Solution-phase synthesis of metal and/or semiconductor homojunction/heterojunction nanomaterials. *Nanoscale* **2011,** *3* (5), 2099-2117.
81. Mokari, T.; Sztrum, C. G.; Salant, A.; Rabani, E.; Banin, U., Formation of asymmetric one-sided metal-tipped semiconductor nanocrystal dots and rods. *Nat. Mater.* **2005,** *4* (11), 855-863.
82. Mokari, T.; Rothenberg, E.; Popov, I.; Costi, R.; Banin, U., Selective Growth of Metal Tips onto Semiconductor Quantum Rods and Tetrapods. *Science* **2004,** *304* (5678), 1787.
83. Menagen, G.; Macdonald, J. E.; Shemesh, Y.; Popov, I.; Banin, U., Au Growth on Semiconductor Nanorods: Photoinduced versus Thermal Growth Mechanisms. *J. Am. Chem. Soc.* **2009,** *131* (47), 17406-17411.
84. Costi, R.; Saunders, A. E.; Elmalem, E.; Salant, A.; Banin, U., Visible Light-Induced Charge Retention and Photocatalysis with Hybrid CdSe−Au Nanodumbbells. *Nano Lett.* **2008,** *8* (2), 637-641.
85. Chen, S.; Thota, S.; Reggiano, G.; Zhao, J., Generalized seeded growth of Ag-based metal chalcogenide nanorods via controlled chalcogenization of the seeds. *J. Mater. Chem. C* **2015,** *3* (45), 11842-11849.
86. Zhang, L.; Blom, D. A.; Wang, H., Au–Cu2O Core–Shell Nanoparticles: A Hybrid Metal-Semiconductor Heteronanostructure with Geometrically Tunable Optical Properties. *Chem. Mater.* **2011,** *23* (20), 4587-4598.
87. Kuo, C.-H.; Hua, T.-E.; Huang, M. H., Au Nanocrystal-Directed Growth of Au−Cu2O Core−Shell Heterostructures with Precise Morphological Control. *J. Am. Chem. Soc.* **2009,** *131* (49), 17871-17878.
88. Naiki, H.; Masuhara, A.; Masuo, S.; Onodera, T.; Kasai, H.; Oikawa, H., Highly Controlled Plasmonic Emission Enhancement from Metal-Semiconductor Quantum Dot Complex Nanostructures. *J. Phys. Chem. C* **2013,** *117* (6), 2455-2459.
89. Liu, N.; Prall, B. S.; Klimov, V. I., Hybrid Gold/Silica/Nanocrystal-Quantum-Dot Superstructures: Synthesis and Analysis of Semiconductor−Metal Interactions. *J. Am. Chem. Soc.* **2006,** *128* (48), 15362-15363.
90. Li, M.; Cushing, S. K.; Wang, Q.; Shi, X.; Hornak, L. A.; Hong, Z.; Wu, N., Size-Dependent Energy Transfer between CdSe/ZnS Quantum Dots and Gold Nanoparticles. *J. Phys. Chem. Lett.* **2011,** *2* (17), 2125-2129.
91. Gueroui, Z.; Libchaber, A., Single-Molecule Measurements of Gold-Quenched Quantum Dots. *Phys. Rev. Lett.* **2004,** *93* (16), 166108.

92. Ribeiro, T.; Prazeres, T. J. V.; Moffitt, M.; Farinha, J. P. S., Enhanced Photoluminescence from Micellar Assemblies of Cadmium Sulfide Quantum Dots and Gold Nanoparticles. *J. Phys. Chem. C* **2013,** *117* (6), 3122-3133.
93. Samanta, A.; Zhou, Y.; Zou, S.; Yan, H.; Liu, Y., Fluorescence Quenching of Quantum Dots by Gold Nanoparticles: A Potential Long Range Spectroscopic Ruler. *Nano Lett.* **2014,** *14* (9), 5052-5057.
94. Samanta, A.; Deng, Z.; Liu, Y., Infrared emitting quantum dots: DNA conjugation and DNA origami directed self-assembly. *Nanoscale* **2014,** *6* (9), 4486-4490.
95. Ko, S. H.; Du, K.; Liddle, J. A., Quantum-Dot Fluorescence Lifetime Engineering with DNA Origami Constructs. *Angew. Chem. Int. Ed.* **2013,** *52* (4), 1193-1197.
96. Du, K.; Ko, S. H.; Gallatin, G. M.; Yoon, H. P.; Alexander Liddle, J.; Berglund, A. J., Quantum dot-DNA origami binding: a single particle, 3D, real-time tracking study. *Chem. Commun.* **2013,** *49* (9), 907-909.
97. Deng, Z.; Samanta, A.; Nangreave, J.; Yan, H.; Liu, Y., Robust DNA-Functionalized Core/Shell Quantum Dots with Fluorescent Emission Spanning from UV–vis to Near-IR and Compatible with DNA-Directed Self-Assembly. *J. Am. Chem. Soc.* **2012,** *134* (42), 17424-17427.
98. Lee, J.; Govorov, A. O.; Kotov, N. A., Nanoparticle Assemblies with Molecular Springs: A Nanoscale Thermometer. *Angew. Chem. Int. Ed.* **2005,** *44* (45), 7439-7442.
99. Jin, Y.; Gao, X., Plasmonic fluorescent quantum dots. *Nat. Nano.* **2009,** *4* (9), 571-576.
100. Karan, N. S.; Keller, A. M.; Sampat, S.; Roslyak, O.; Arefin, A.; Hanson, C. J.; Casson, J. L.; Desireddy, A.; Ghosh, Y.; Piryatinski, A.; Iyer, R.; Htoon, H.; Malko, A. V.; Hollingsworth, J. A., Plasmonic giant quantum dots: hybrid nanostructures for truly simultaneous optical imaging, photothermal effect and thermometry. *Chem. Sci.* **2015,** *6* (4), 2224-2236.
101. Ji, B.; Giovanelli, E.; Habert, B.; Spinicelli, P.; Nasilowski, M.; Xu, X.; Lequeux, N.; Hugonin, J.-P.; Marquier, F.; Greffet, J.-J.; Dubertret, B., Non-blinking quantum dot with a plasmonic nanoshell resonator. *Nat. Nano.* **2015,** *10* (2), 170-175.
102. Shimizu, K. T.; Woo, W. K.; Fisher, B. R.; Eisler, H. J.; Bawendi, M. G., Surface-Enhanced Emission from Single Semiconductor Nanocrystals. *Phys. Rev. Lett.* **2002,** *89* (11), 117401.
103. Yuan, C. T.; Yu, P.; Ko, H. C.; Huang, J.; Tang, J., Antibunching Single-Photon Emission and Blinking Suppression of CdSe/ZnS Quantum Dots. *ACS Nano* **2009,** *3* (10), 3051-3056.
104. Yuan, C. T.; Wang, Y. C.; Cheng, H. W.; Wang, H. S.; Kuo, M. Y.; Shih, M. H.; Tang, J., Modification of Fluorescence Properties in Single Colloidal Quantum Dots by Coupling to Plasmonic Gap Modes. *J. Phys. Chem. C* **2013,** *117* (24), 12762-12768.
105. Ma, X.; Fletcher, K.; Kipp, T.; Grzelczak, M. P.; Wang, Z.; Guerrero-Martínez, A.; Pastoriza-Santos, I.; Kornowski, A.; Liz-Marzán, L. M.; Mews, A., Photoluminescence of Individual Au/CdSe Nanocrystal Complexes with Variable Interparticle Distances. *J. Phys. Chem. Lett.* **2011,** *2* (19), 2466-2471.
106. Ma, X.; Tan, H.; Kipp, T.; Mews, A., Fluorescence Enhancement, Blinking Suppression, and Gray States of Individual Semiconductor Nanocrystals Close to Gold Nanoparticles. *Nano Lett.* **2010,** *10* (10), 4166-4174.
107. LeBlanc, S. J.; McClanahan, M. R.; Jones, M.; Moyer, P. J., Enhancement of Multiphoton Emission from Single CdSe Quantum Dots Coupled to Gold Films. *Nano Lett.* **2013,** *13* (4), 1662-1669.
108. Park, Y.-S.; Ghosh, Y.; Chen, Y.; Piryatinski, A.; Xu, P.; Mack, N. H.; Wang, H.-L.; Klimov, V. I.; Hollingsworth, J. A.; Htoon, H., Super-Poissonian Statistics of Photon Emission

from Single CdSe-CdS Core-Shell Nanocrystals Coupled to Metal Nanostructures. *Phys. Rev. Lett.* **2013,** *110* (11), 117401.
109. Canneson, D.; Mallek-Zouari, I.; Buil, S.; Quélin, X.; Javaux, C.; Mahler, B.; Dubertret, B.; Hermier, J. P., Strong Purcell effect observed in single thick-shell CdSe/CdS nanocrystals coupled to localized surface plasmons. *Phys. Rev. B* **2011,** *84* (24), 245423.
110. Lee, S. Y.; Nakaya, K.; Hayashi, T.; Hara, M., Quantitative study of the gold-enhanced fluorescence of CdSe/ZnS nanocrystals as a function of distance using an AFM probe. *Phys. Chem. Chem. Phys.* **2009,** *11* (21), 4403-4409.
111. Fulmes, J.; Jager, R.; Brauer, A.; Schafer, C.; Jager, S.; Gollmer, D. A.; Horrer, A.; Nadler, E.; Chasse, T.; Zhang, D.; Meixner, A. J.; Kern, D. P.; Fleischer, M., Self-aligned placement and detection of quantum dots on the tips of individual conical plasmonic nanostructures. *Nanoscale* **2015,** *7* (35), 14691-14696.
112. Garno, J. C.; Yang, Y.; Amro, N. A.; Cruchon-Dupeyrat, S.; Chen, S.; Liu, G.-Y., Precise Positioning of Nanoparticles on Surfaces Using Scanning Probe Lithography. *Nano Lett.* **2003,** *3* (3), 389-395.
113. Ratchford, D.; Shafiei, F.; Kim, S.; Gray, S. K.; Li, X., Manipulating Coupling between a Single Semiconductor Quantum Dot and Single Gold Nanoparticle. *Nano Lett.* **2011,** *11* (3), 1049-1054.
114. Masuo, S.; Kanetaka, K.; Sato, R.; Teranishi, T., Direct Observation of Multiphoton Emission Enhancement from a Single Quantum Dot Using AFM Manipulation of a Cubic Gold Nanoparticle. *ACS Photon.* **2016,** *3* (1), 109-116.
115. Naiki, H.; Masuo, S.; Machida, S.; Itaya, A., Single-Photon Emission Behavior of Isolated CdSe/ZnS Quantum Dots Interacting with the Localized Surface Plasmon Resonance of Silver Nanoparticles. *J. Phys. Chem. C* **2011,** *115* (47), 23299-23304.
116. Dey, S.; Zhou, Y.; Tian, X.; Jenkins, J. A.; Chen, O.; Zou, S.; Zhao, J., An experimental and theoretical mechanistic study of biexciton quantum yield enhancement in single quantum dots near gold nanoparticles. *Nanoscale* **2015,** *7* (15), 6851-6858.
117. Wang, H.; Zou, S., A generalized electrodynamics model for surface enhanced Raman scattering and enhanced/quenched fluorescence calculations. *RSC Adv.* **2013,** *3* (44), 21489-21493.
118. Kuhn, H., Classical Aspects of Energy Transfer in Molecular Systems. *J. Chem. Phys.* **1970,** *53* (1), 101-108.
119. Giannini, V.; Sánchez-Gil, J. A.; Muskens, O. L.; Rivas, J. G., Electrodynamic calculations of spontaneous emission coupled to metal nanostructures of arbitrary shape: nanoantenna-enhanced fluorescence. *J. Opt. Soc. Am. B* **2009,** *26* (8), 1569-1577.
120. Carles Curutchet, R. C., Self-consistent quantum mechanical model for the description of excitation energy transfers in molecules at interfaces. *J. Chem. Phys.* **2006,** *125* (5), 054710.
121. Persson, B. N. J.; Lang, N. D., Electron-hole-pair quenching of excited states near a metal. *Phys. Rev. B* **1982,** *26* (10), 5409-5415.
122. Sukharev, M.; Freifeld, N.; Nitzan, A., Numerical Calculations of Radiative and Non-Radiative Relaxation of Molecules Near Metal Particles. *J. Phys. Chem. C* **2014,** *118* (20), 10545-10551.
123. Carminati, R.; Greffet, J. J.; Henkel, C.; Vigoureux, J. M., Radiative and non-radiative decay of a single molecule close to a metallic nanoparticle. *Opt. Commun.* **2006,** *261* (2), 368-375.
124. Nagpal, P.; Klimov, V. I., Role of mid-gap states in charge transport and photoconductivity in semiconductor nanocrystal films. *Nat. Commun.* **2011,** *2*, 486.

# Chapter Two .

# An Experimental and Theoretical Mechanistic Study of Biexciton Quantum Yield Enhancement in Single Quantum Dots near Gold Nanoparticles



## 2.1 Abstract

In this work, we systematically investigated the plasmonic effect on blinking, photon antibunching behavior and biexciton emission of single CdSe/CdS core/shell quantum dots (QDs) near gold nanoparticles (NPs) with a silica shell (Au@$SiO_2$). In order to obtain strong interaction between the plasmons and excitons, the Au@$SiO_2$ NPs and CdSe/CdS QDs of proper sizes were chosen so that the plasmon resonance overlaps with the absorption and emission of the QDs. We observed that in the regime of low excitation power, the photon antibunching and blinking properties of single QDs were modified significantly when the QDs were on the Au@$SiO_2$ substrates compared to on glass. Most significantly, second-order photon intensity correlation data shows that the presence of plasmons increases the ratio of biexciton quantum yield over exciton quantum yield ($QY_{BX}/QY_X$). An electrodynamics model was developed to quantify the effect of plasmons on the lifetime, quantum yield, and emission intensity of the biexcitons for the QDs. Good agreement was obtained between the experimentally measured and calculated changes in $QY_{BX}/QY_X$ due to Au@$SiO_2$ NPs, showing the validity of the developed model. The theoretical studies also indicated that the relative position of the QDs to the Au NPs and the orientation of electric field are important factors that regulate the emission properties of the excitons and

biexcitons of QDs. The study suggests that the multiexciton emission efficiency in QD systems can be manipulated by employing properly designed plasmonic structures.

## 2.2 Introduction

Over the past few decades, significant interest has been shown in semiconductor nanocrystals, also popularly known as quantum dots (QDs). The distinct size-dependent optical properties of QDs combined with high quantum efficiency make them ideal candidates as tunable absorbers and emitters for applications ranging from nanoelectronics to biological imaging.[1-8] The properties of excitons (Xs) and multiexcitons (MXs) in QDs are key elements that determine their optical and electrical behaviors, which control the usability of QDs in specific applications. For example, single QDs with sufficiently low MX emission efficiencies are promising solid-state single photon emitters for quantum optics including quantum computation and quantum cryptography.[9-10] On the other hand, QDs with high MX emission efficiency are excellent materials to increase optical gain for lasing applications.[11-12] Furthermore, studies in carrier multiplication (also known as multiexciton generation) efficiency in QDs provide new insights into exploring their applications in photovoltaics.[4, 13-14]

Once synthesized, the optical properties of QDs largely depend on the quality of the material itself. To adapt the synthesized QDs to various applications with different requirements of X and MX emission behavior, a feasible solution is to place the QDs close to plasmonic metal nanostructures or nanoparticles (NPs) and thus to modify the optical properties of QDs. [15-27] As a result of the excitation of localized surface plasmon resonance (LSPR) in these metal nanostructures, the local electric field around the metal nanostructures is greatly enhanced which could alter the absorption cross-section and the excitation rate of the QDs adsorbed to them.[15-17, 20, 26, 28] Moreover, the radiative decay rates of the QDs may change and additional recombination

channels may open up due to the presence of the metal nanostructures. For example, Mews and co-workers observed distance-dependent X emission of single CdSe QDs adsorbed on an Au@$SiO_2$ NP with varying silica shell thickness and demonstrated that the CdSe QDs exhibit greater "on" fractions when adsorbed to the Au@$SiO_2$ NP.[17] On the other hand, limited studies have been conducted on quantifying the plasmonic effect on the MX emission of single QDs.[29-33] For instance, two reports showed that MX emission efficiency of single QDs was altered when they were deposited on roughened Ag or Au thin films.[29-30] Due to the lack of well-defined geometry and plasmon resonance band in these metal films, the mechanism of the MX emission efficiency change due to plasmons is still not well understood. In addition to this lack in understanding, a quantitative explanation of the changes in the X/MX emission intensity, lifetimes, and quantum yields is missing. This work presents our effort to elucidate the effect of plasmon resonance on MX emission of single QDs, and to quantitatively determine the MX quantum yield (QY), lifetimes, etc.

In our study, we performed single QD fluorescence measurements on LSPR substrates consisted of core@shell Au@$SiO_2$ NPs immobilized on glass, and compared the results to that obtained from single QDs on glass. The substrates have well defined LSPR peaks, in stark contrast to the LSPR peaks observed for thin metal films in previous studies.[29-30] In addition to this system having well defined peaks, the system allows us to investigate the effect of nanostructure geometry, as well as the interparticle distance between the NPs and QDs on the near-field exciton-plasmon interaction.[17, 31-34] From second-order photon intensity correlation ($g^{(2)}(\tau)$) measurements, we observed a significant difference in the photon-antibunching "dips" in the single QDs on Au@$SiO_2$ NP substrates compared to the QDs on glass. Specifically, the $g^{(2)}(\tau)$ dips of the QDs on Au@$SiO_2$ NP are much smaller than those of the QDs on glass, indicating an increase in the ratio of biexciton

BX QY over X QY.[35] In order to determine whether the increase is due to changes in radiative rates, QYs, or other factors, an electrodynamics model based on Xs was extended to quantitatively calculate the emission intensity, QYs and lifetimes of BXs of QDs close to Au@$SiO_2$ NPs. Varying geometry, electric field orientation, and interparticle distances were explored in the modeling to examine their roles in controlling the plasmonic effect on X and MX emission. The results have shown that the BX QY of the QDs is increased, while the X QY is decreased due to the presence of Au NPs. These findings are in good agreement with the experimental observations. Thus, both the experimental and theoretical studies clarified the plasmonic effect on X and BX emission of single QDs and identified important factors that regulate the exciton-plasmon interaction, such as interparticle distance, geometry, and electric field orientation. The experimental method and model can be applied to QDs close to any plasmonic nanostructures, to realize quantitative control of the MX emission efficiency of QDs by plasmons.

## 2.3 Experimental Methods

### *2.3.1 LSPR substrate preparation*

The Au NPs (average diameter~120 nm) were synthesized by a two-step citrate reduction method.[36] The Au NPs were then coated with silica shells with thickness ranging from 4 to 10 nm based on a method developed by Li et al.[37] To immobilize Au@$SiO_2$ nanoparticles on glass, No 1.5 glass coverslips (Fisher Scientific) were cleaned, sonicated and functionalized with APTES((3-Aminopropyl)triethoxysilane) (Sigma Aldrich). The pretreated glass coverslips were incubated in Au@$SiO_2$ nanoparticles overnight and rinsed roughly to remove excess nanoparticles. The SEM images of the Au@$SiO_2$ nanoparticles on the glass substrate were taken using a JEOL JSM-6335F scanning electron microscope (SEM) operated with a resolution of 1.5 nm at 15kV.

### *2.3.2 CdSe/CdS QD synthesis*

CdSe/CdS core/shell QDs were synthesized following a modified procedure developed by Chen et al.[59] The photoluminescence (PL) quantum yield (QY) of these QDs in toluene is 94.9%, as determined by comparison to Rhodamine B in ethanol. The shape and size distribution of the QDs was characterized using a JEOL2010 transmission electron microscope (TEM) operated at 200kV.

### *2.3.3 Optical Characterization*

The absorption and emission spectra of QDs in solution were measured using a Cary-60 (Agilent) UV-Vis spectrophotometer and Cary Eclipse (Agilent) spectrofluorometer, respectively. The fluorescence of individual QDs was collected with a home-built confocal fluorescence microscope using a Nikon Ti-u microscope equipped with a piezo stage (PI 320, Physik Instrument). The QDs were excited using a Sapphire 532 LP CW-Laser (Coherent) focused through a 100x oil-immersion objective (Nikon, NA = 1.3). The emission of the QDs was collected by the same objective, split with a 50/50 beam splitter, and directed onto two single-photon detectors (τ-SPAD**,** Picoquant) in a Hanbury-Brown and Twiss (HBT) geometry. The time-dependent single photon counting measurements were performed using a PicoHarp 300 (Picoquant) in time-tagged time-resolved mode (TTTR) with a timing resolution of 32 ps. The time resolution of the τ-SPAD is ~ 600ps. Considering all these factors, the time resolution was high enough to resolve the $g^{(2)}$ function of the QDs. The PL intensity time traces of single QDs were simultaneously recorded using pulse counters (National Instruments). The corresponding $g^2(\tau)$ data were processed with Sympho Time 64 software (Picoquant). We varied the sampling size and the time window used for the $g^2(\tau)$ analysis and confirmed that these parameters had a

negligible effect on the $g^2(\tau)$ data. For the fluorescence lifetime measurements, QDs on $Au@SiO_2$ NPs and on glass were excited with a 405 nm pulsed laser (pulse width of 40 ps and repetition rate of 2.5 MHz, Picoquant). All the measurements were performed at room temperature.

## 2.4 Results and Discussion

For the optical studies, we prepared the single QDs on $Au@SiO_2$ NP substrates following two steps, as illustrated in **Figure 2.1A**. First, $Au@SiO_2$ NPs were synthesized and immobilized on silanized glass. Next home-made CdSe/CdS QDs were dispersed in toluene and spun-cast onto $Au@SiO_2$ NP coated glass coverslips. The QDs were also deposited on blank glass coverslips for comparison. The QD solution was diluted enough so that the density of the QDs on the substrates was appropriate for single QD measurements. As evidenced by the TEM in **Figure 2.1B**, the average diameter of the QDs is 9.2 ± 1.2 nm. **Figure 2.1D** shows the SEM images of the substrate comprised of $Au@SiO_2$ NPs with diameter of 120 nm and silica shell thickness of 9.6 ± 1.2 nm. $Au@SiO_2$ NP with 5.1± 1.0 nm silica shell was also used as a substrate as shown in the SEM images in **Figure 2.1C**. The insets in the figures are the corresponding high resolution TEM images of the $Au@SiO_2$ NPs.

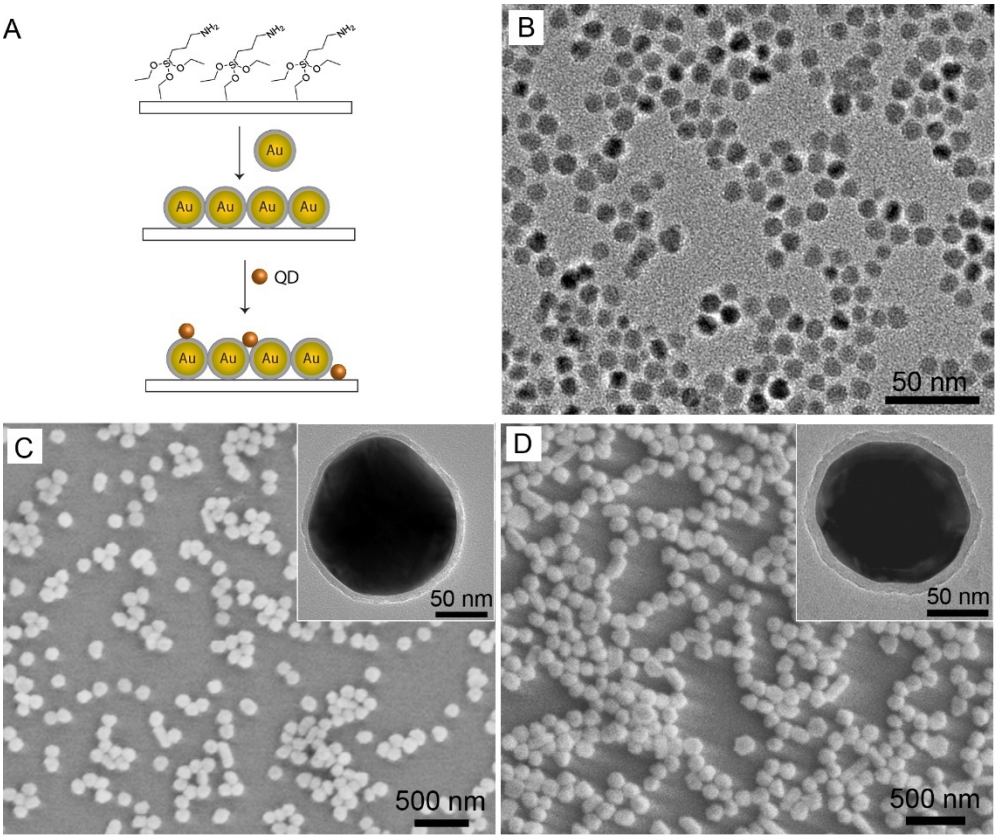


**Figure 2.1**. (A) Schematic representation of QD on Au@$SiO_2$ sample preparation. (B) TEM image of the CdSe/CdS QDs. (C) SEM image of the Au@$SiO_2$-10nm NPs;(inset) HR-TEM image of a Au@$SiO_2$-10nm NP.

### *2.4.1 Spectral position of LSPR and absorption/emission*

Exciton-plasmon coupling is highly dependent on the spectral overlap between the LSPR of the metal NPs and the absorption/emission of the QDs.[19, 32-34] In our study, the absorption spectrum of the CdSe/CdS QDs shows distinct excitonic features and the emission spectrum is narrow (full width at half maximum = 29 nm) with a peak at 629 nm as illustrated in **Figure 2.2A**. The LSPR of Au@$SiO_2$-5 nm peaks at 597 nm and Au@$SiO_2$-10 nm peaks at 612 nm as shown in **Figure 2.2B**. The LSPR of Au@$SiO_2$-10 nm is red-shifted (15 nm) from that of Au@$SiO_2$-5 nm,

because the local dielectric constant of the Au NP is increased when the silica shell is thicker. The spectra show that there is a substantial overlap between the LSPR bands of Au@$SiO_2$ NPs and the absorption/emission wavelengths of the CdSe/CdS QDs. To ensure both the LSPR of the Au@$SiO_2$ NPs and the QDs were excited, a 532 nm continuous wave laser was used. The excitation power density was kept very low, ~ 6.4 W/$cm^2$. We estimated the average photons absorbed (<N>) by a QD within its exciton lifecycle was ~ 0.0015. The low excitation power ensured low multiexciton excitation probability in the experiments. We also ensure background scattering or fluorescence from the Au@$SiO_2$ NPs, if any, is negligible.

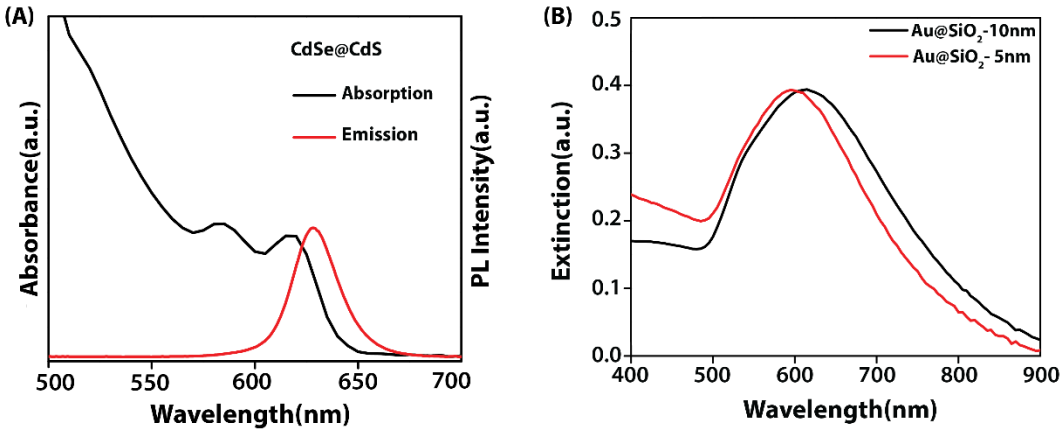


**Figure 2.2**. (A) Absorption (black) and emission (red) spectra of CdSe/CdS QDs in toluene solution. (B) Extinction spectra of Au@$SiO_2$-5nm and Au@$SiO_2$-10nm nanoparticles in water.

### *2.4.2 $g^2(\tau)$ and blinking traces of single QDs on glass and Au NPs*

In order to understand the effect of plasmons on the X and BX emission efficiency of single QDs with varying interparticle distance between the QDs and NPs, we simultaneously measured the PL intensity blinking traces and the second-order photon intensity cross correlation ($g^2(\tau)$) for single QDs on glass and Au@$SiO_2$-10 nm. $g^2(\tau)$ gives the histogram of single-photon coincidence events.[38-39] Mathematically, $g^{(2)}(\tau)$ is calculated by $g^{(2)}(\tau) = \frac{\langle I(t) \cdot I(t+\tau) \rangle}{\langle I(t) \rangle \cdot \langle I(t+\tau) \rangle}$ where I(t) is the time-dependent emission intensity of the system and $\tau$ is the time difference between the detection of two emitted photons by the two single photon detectors in a Hanbury Brown and Twiss geometry.[40-41] In single QD studies, photon antibunching is often used to prove that the probed emitters are truly single QDs.[42] However, if the BX emission of single QDs was not negligible, the $g^{(2)}(\tau)$ function can be conveniently used to determine the BX to X QY ratio, as recently demonstrated by Nair and coworkers, and also in some following studies.[35, 43-45]

**Figure 2.3A**, **Figure 2.3D** and **Figure 2.3G** show representative $g^2(\tau)$ data of a single QD on the glass, Au@$SiO_2$-5 nm and Au@$SiO_2$-10 nm substrates, respectively. The $g^2(\tau)$ data clearly revealed a drastic change in the normalized $g^2(\tau)$ dip value of the single QDs when they are on glass and on Au substrates. For the QD on glass, the $g^2(\tau)$ dip value is low, ~ 0.2, with a relatively slow decay. For the QDs on Au@$SiO_2$ NPs, the $g^2(\tau)$ dip value is significantly higher, ~ 0.6 from **Figure 2.3G**, with a much faster decay. Such high $g^2(\tau)$ dip values for the QDs on Au@$SiO_2$ NPs raise the question if they are clusters of QDs instead of single QDs. The corresponding PL blinking traces of the same QDs in **Figure 2.3E** showed distinct "on"/"off" blinking, indicating it is indeed single QDs.

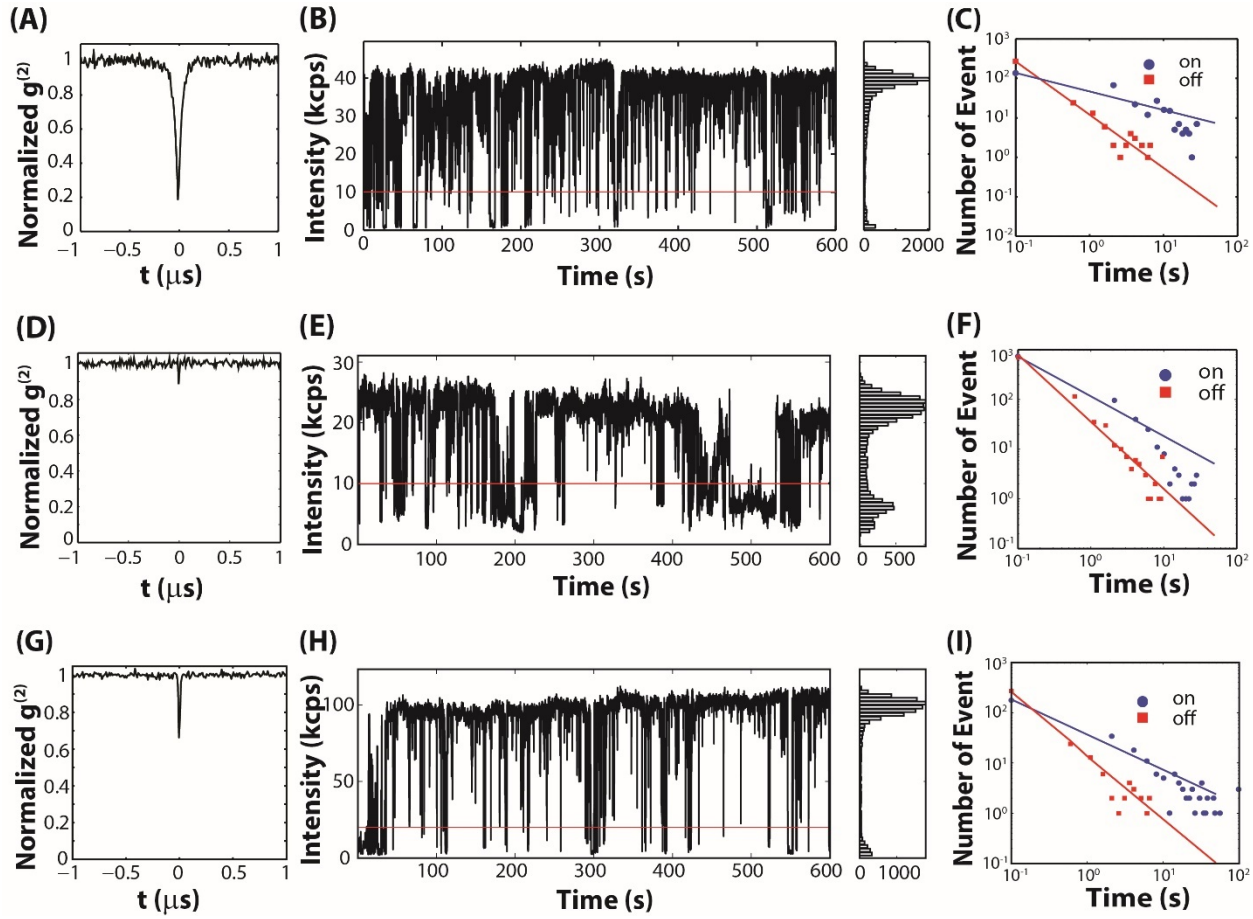


**Figure 2.3**. Representative $g^{(2)}$ measurements (A and D) blinking traces (B and E) of single QDs, and log-log plots of the "on","off" time statistics (C and F) of QDs on different substrates. (A-C) on glass, (D-F) on Au@$SiO_2$-5nm and (G-F) on Au@$SiO_2$-10nm respectively. The red lines in B and E denote the threshold between the "on" and "off" events. Histograms indicating the distribution of intensities observed in the time trace. The distribution fit well to power-law distribution where $\boldsymbol{Number\ of\ events} \propto \boldsymbol{t_{on/off}}^{-\boldsymbol{\alpha_{on/off}}}$ where $\boldsymbol{\alpha_{on}}$= 0.85 and $\boldsymbol{\alpha_{off}}$ = 1.5 for QDs on glass, and both $\boldsymbol{\alpha_{on}}$ and $\boldsymbol{\alpha_{off}}$= 1.5 for QDs on Au@$SiO_2$-10nm.

Similar changes in the $g^2(\tau)$ dip values of single QDs on Au@$SiO_2$ NPs was observed in QDs on Au@$SiO_2$-5 nm substrate as well as observed in **Figure 2.4**.The QDs show much higher $g^2(\tau)$ dips but their corresponding traces still exhibit a clear two-state blinking behavior.

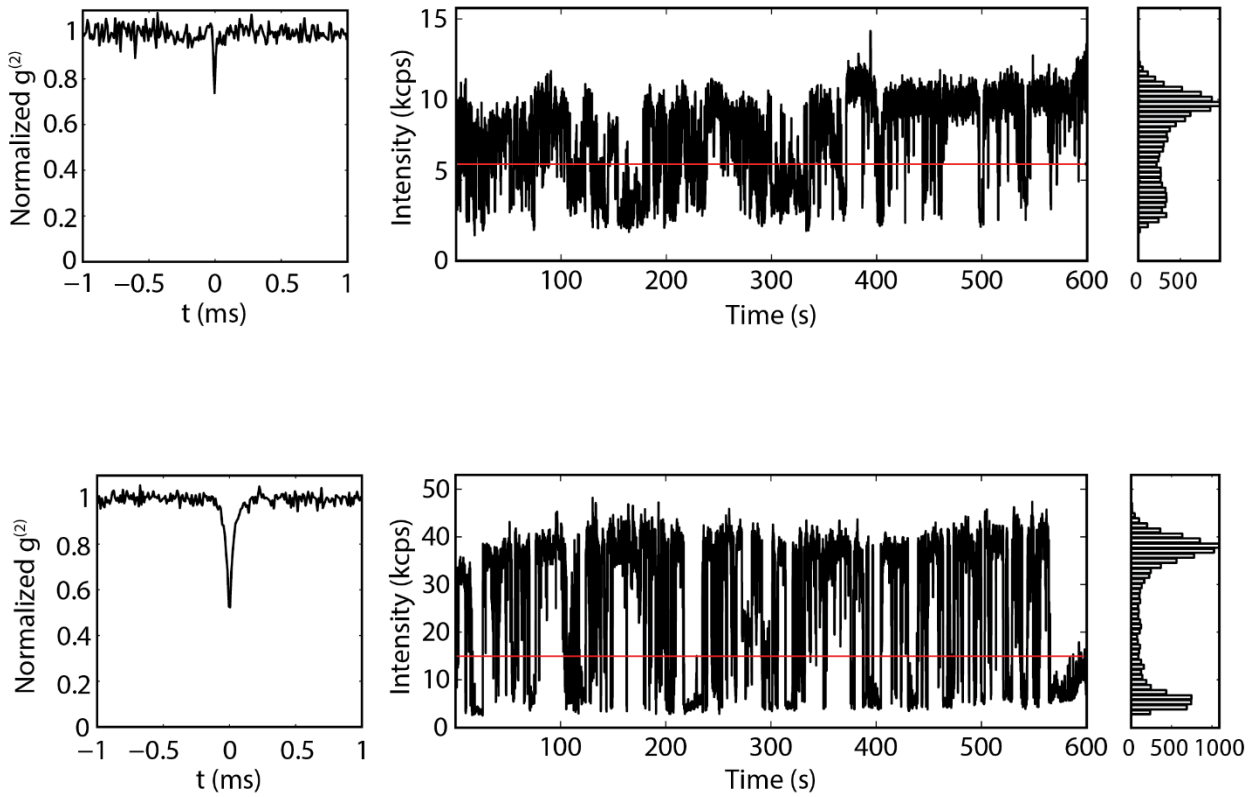


**Figure 2.4**. Representative $g^{(2)}$ measurements and corresponding blinking traces of single QDs on Au@$SiO_2$-5nm substrate.

Figure 2.5 shows some representative $g^2(\tau)$ data and the corresponding blinking traces for single QDs deposited on Au@$SiO_2$-10nm substrate. The photoluminescence intensity shows a certain degree of enhancement as compared to the QDs on Au@$SiO_2$-5nm substrate with also an increased dwell time for "on" fractions.

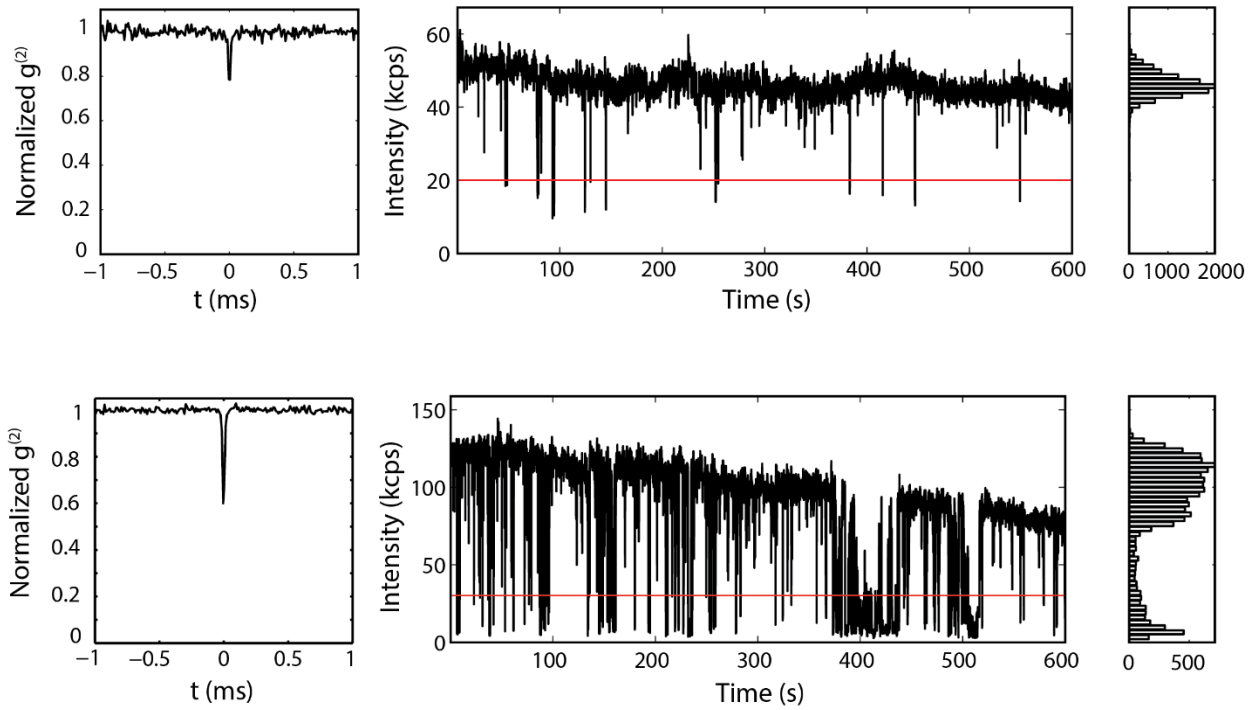


**Figure 2.5**. Representative g (2) measurements and corresponding blinking traces of single QDs on Au@SiO2-10nm substrate.

From the blinking traces, we analyzed the distributions for "on" and "off" event durations and they all fit well to power-law distribution where $Number\ of\ events \propto {t_{on/off}}^{-\alpha_{on/off}}$, as shown in **Figure 2.3C**,**Figure 2.3F** and **Figure 2.3I**. The powers $\alpha_{on/off}$ are different for QDs on Au@$SiO_2$ NPs compared to the QDs on glass, showing that plasmons can effectively modify the dwell times of the "on"/"off" events of the single QDs. The PL blinking traces and intensity histograms of single QDs (shown in **Figure 2.3B**, **Figure 2.3E** and **Figure 2.3H**) clearly demonstrate that the QDs all exhibit a two-state blinking with well-defined "on" and "off" states whether they are on glass or Au@$SiO_2$ NPs. The red lines in these denote the threshold between the "on" and "off" events. For quantitative analysis, the corresponding statistics of "on" and "off" times are calculated from the blinking traces and plotted in **Figure 2.3B** and **Figure 2.3E**. The

lines in the plots are the power-law fit for the "on"/ "off" statistics. All the distributions for "on" and "off" event durations fit well to power-law distribution where $Number\ of\ events \propto t_{on/off}{}^{-\alpha_{on/off}}$. In the power-law function, $t_{on/off}$ represents the time intervals that a QD stays in an "on" or "off" state, and $\alpha_{on/off}$ represents the power-law exponents. For the CdSe/CdS QDs on glass, $\alpha_{on}$= 0.85 and $\alpha_{off}$ = 1.5. The small $\alpha_{on}$ for the QDs is consistent with previous study and showing that the QDs have long "on" times. When the QDs were adsorbed on Au@SiO2 NP substrates, the "on"/"off" statistics still follows power-law distribution but values of $\alpha_{on/off}$ have changed. And more interestingly, the values of $\alpha_{on}$ and $\alpha_{off}$ are similar for the QDs on Au@SiO2 NP. The calculated $\alpha_{on/off}$for QDs on Au@$SiO_2$ NP with ~ 5 nm silica shell are $\alpha_{on}$= 1.8 and $\alpha_{off}$ = 1.85; and for QDs on Au@$SiO_2$ NP with ~ 10 nm silica shell, both $\alpha_{on}$ and $\alpha_{off}$ are 1.5. The dwell times for the "on"/"off" events of the single QDs are altered by the presence of the Au NPs, especially the "on" events. The results indicate the plasmonic structures may be used to modify the photo darkening process in QD films, important for their application in light emitting devices.

As shown in **Figure 2.6**, the $g^2(\tau)$ dip distribution of single QDs was significantly different for QDs on glass and NP substrates. For the single QDs on the glass substrate, a majority (75%) of the $g^2(\tau)$ data showed a dip between the range of 0.1 – 0.2 (**Figure 2.6A**). The small $g^2(\tau)$ dip values, verifying that we were probing single QDs, indicate that a majority of the QDs have low BX QYs.[46-52] A small portion (6%) of the QDs on glass have $g^2(\tau)$ dips values greater than 0.5. The corresponding blinking traces of these QDs have clear two-state blinking, confirming they are single QDs. The high $g^2(\tau)$ dip values of these QDs are due to the high BX QY in these QDs, consistent with previous observations in CdSe/CdS QDs.[44] For QDs on Au@$SiO_2$-10 nm substrate, the $g^2(\tau)$ dip distribution has become much broader. About 90% of the QDs have $g^2(\tau)$ dip values in the range of 0.4 – 1.

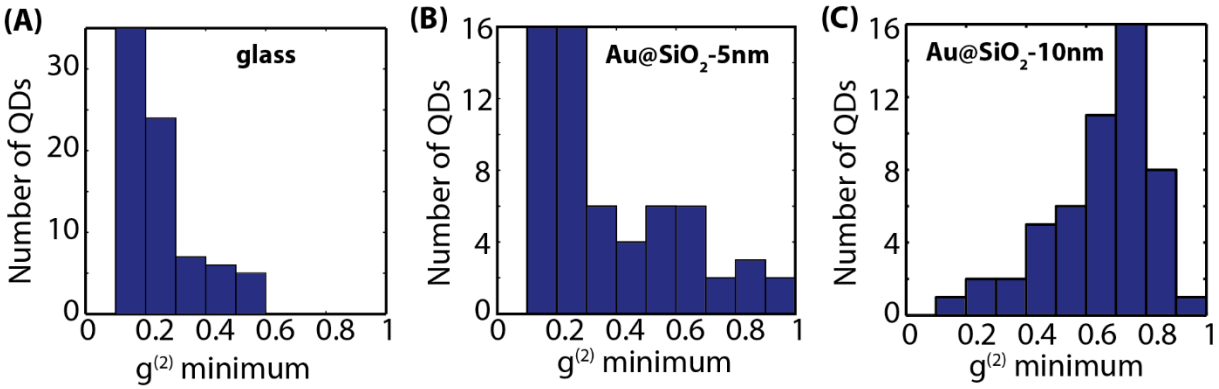


**Figure 2.6**. Histograms of the $g^{(2)}$ minimum data of single QDs on different substrates (A) on glass, (B) Au@$SiO_2$-5 nm and (C) on Au@$SiO_2$-10nm.

Similar phenomenon was observed in QDs on Au@$SiO_2$-5 nm substrate as observed in **Figure 2.6B**. To understand the distribution of $g^2(\tau)$, we note that the QDs were randomly spin-coated on the substrates and their distance to Au NP is not controlled. Since plasmonic effect is near-field in nature and decays fast from the metal surface, for QDs far away from the NPs, their X and BX emission is much less affected than the QDs close to or on the NPs. The small portion of QDs with $g^2(\tau)$ dip values of 0.1-0.2 are likely to be situated far from the NPs thus behave like the QDs on bare glass. Nevertheless, the drastic change in the $g^2(\tau)$ dip distribution of QDs on NPs compared to on glass demonstrates that the presence of plasmons can effectively change the emission of Xs and MXs by different ratios. The fact that majority of the QDs on Au@$SiO_2$ NPs have high $g^2(\tau)$ dip values suggest that the ratio of BX QY to X QY of these QDs is significantly higher than the QDs on glass. The difference in the $g^2(\tau)$ values distribution of QDs on Au@SiO2 NP substrates may be related to how the Au@SiO2 NPs were distributed on glass. We reexamined the SEM images of the Au@$SiO_2$-5 nm (**Figure 2.1C**) and Au@$SiO_2$-10 nm (**Figure 2.1D**) substrates. It is clear from the SEM images of the Au@$SiO_2$-5 nm and Au@$SiO_2$-10 nm substrates that the packing density of the Au@$SiO_2$ NPs is different on those two substrates. The Au@$SiO_2$-

5 nm substrate has much more void space without the NPs compared to the Au@ $SiO_2$-10 nm substrate. A quantitative analysis revealed the packing density of the NPs on the Au@$SiO_2$-5 nm substrate is 60% lower than that of the Au@ $SiO_2$-10 nm substrate. Since the QDs were randomly spin-coated on the substrates, there is a much higher chance for the QDs to fall on empty glass than on the Au@ $SiO_2$-5 nm substrate. Since plasmonic effect is near-field in nature and decays fast from the metal surface, the X and BX emission of the QDs with a large distance from the NPs is much less affected than the QDs close to or on the NPs. The QDs with $g^2(\tau)$ dip values of 0.1-0.2 are likely to be situated far from the NPs thus behave like the QDs on bare glass. The two population of QDs lead to the broad distribution of $g^2(\tau)$ dip values. We also show in the calculations that not only the distance between the QD and NP, but also the relative position and the orientation of the QD/NP complex determines the exciton-plasmon coupling strength.

### *2.4.3 PL decays of QDs on NPs*

To further investigate the decay process and the recombination dynamics of the QDs near Au NPs, the ensemble PL decay of single QDs on different substrates was plotted in **Figure 2.7**. In the experiment, a defocusing lens was added in the laser path so that a large number of isolated QDs were excited simultaneously. The PL decay of the QDs on glass (**Figure 2.7a**, black curve) fits well with a bi-exponential decay function of $y = 2.23e^{-t/25.4} + 1.83e^{-t/53.2}$. The PL decays of the QDs attached to or near Au NPs are much shorter and experience much faster decay than the QDs on glass. For the QDs on Au@$SiO_2$-10 nm, the PL decay (**Figure 2.7c**, blue line) fits with $y = 2.49\times10^2e^{-t/8.28} + 1.57e^{-t/45.5}$. The fittings show that for the QDs on NP substrate, the decay process was dominated by a fast decay at shorter times and a much slower decay at longer times.

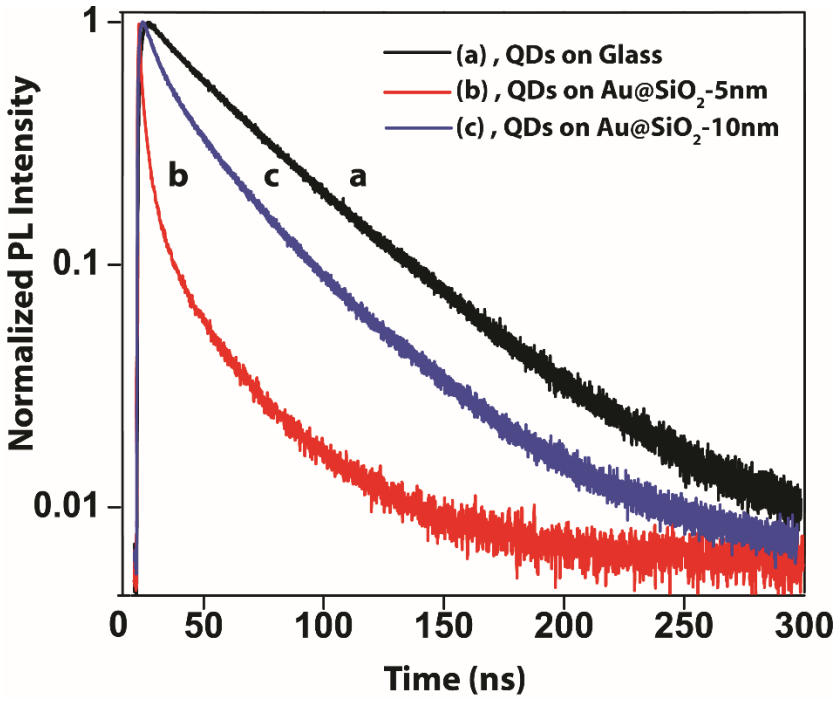


**Figure 2.7**. Ensemble PL decay CdSe/CdS QDs on different substrates (a) on glass (b) on Au@SiO2-5nm (c) on Au@SiO2-10nm.

The PL decay of the QDs on glass (**Figure 2.7a**, black curve) fits well with a biexponential decay function of $y = 2.23e^{-t/25.4} + 1.83e^{-t/53.2}$. For the QDs on Au@$SiO_2$-5 nm, the PL decay (**Figure 2.7b**, red line) fits with $y = 5.81 \times 104e^{-t/4.03} + 0.69e^{-t/28.8}$. For the QDs on Au@$SiO_2$-10 nm, the PL decay (**Figure 2.7c**, blue line) fits with $y = 2.49 \times 102e^{-t/8.28} + 1.57e^{-t/45.5}$. The fittings show that for the QDs on MNP substrate, the decay process was dominated by a fast decay at shorter times and there was also a much slower decay at longer times.

### *2.4.4 Electrodynamics Modeling*

In order to understand the exciton-plasmon coupling in the QD/Au NP systems, we developed an electrodynamics model to calculate the X and BX emission lifetimes and intensities.[53-54] In a previous study, Wang and Zou studied the effect of metal nanoparticle on the

fluorescence lifetime and intensity of a dye molecule in close proximity when varying the nanoparticle size, and the distance between the emitter and the metal nanoparticle.[53] In this work, we extended the model to quantitatively calculate intensity, quantum yield, and lifetime change of BXs. Due to the relatively big size of the Au NPs used in the experiments (~ 120 nm), we also modified the model to include higher order plasmon excitations in the calculations.

For an isolated QD, its QY can be calculated by

$$\boldsymbol{\eta} = \frac{\boldsymbol{k_r}}{\boldsymbol{k_r}+\boldsymbol{k_{nr}}} \qquad \text{Equation 2.1}$$

where η is the QY of an isolated QD, $k_r$ and $k_{nr}$ represent the radiative and non-decay rates of the QD. When the QD is placed near a metal NP, its QY will be modified and the new QY (η') can be calculated with the following equations:

$$\boldsymbol{\eta'} = \frac{\boldsymbol{k_r'}}{\boldsymbol{k_r'}+\boldsymbol{k_{NP}}+\boldsymbol{k_{nr}}} = \frac{\boldsymbol{f_r}\times\boldsymbol{k_r}}{\boldsymbol{f_t}\times\boldsymbol{k_r}+\boldsymbol{k_{nr}}} \qquad \text{Equation 2.2}$$

$$\frac{\boldsymbol{\eta'}}{\boldsymbol{\eta}} = \frac{\boldsymbol{f_r}}{\boldsymbol{f_t}\times\boldsymbol{\eta}+\mathbf{1}-\boldsymbol{\eta}}\ , \qquad \text{Equation 2.3}$$

where $f_r$ (= $k_r'/k_r$) represents the enhancement factor of the radiative decay rate for the QD when a metal NP is placed near to it, and $k_r$, $k_r'$ are the radiative rates of the QD without and with a nanoparticle nearby. Note that $k_r'$ is the enhanced radiative rate of the QD due to the presence of the NP. $f_t = f_r + k_{NP}/k_r$, where $k_{NP}$ represents the non-radiative energy transfer rate from the QD to the metal NP. Also note that $k_{NP}$ does not include the intrinsic non-radiative decay rate of the QDs, $k_{nr}$. **Figure 2.8A** shows a schematic illustration of these processes.

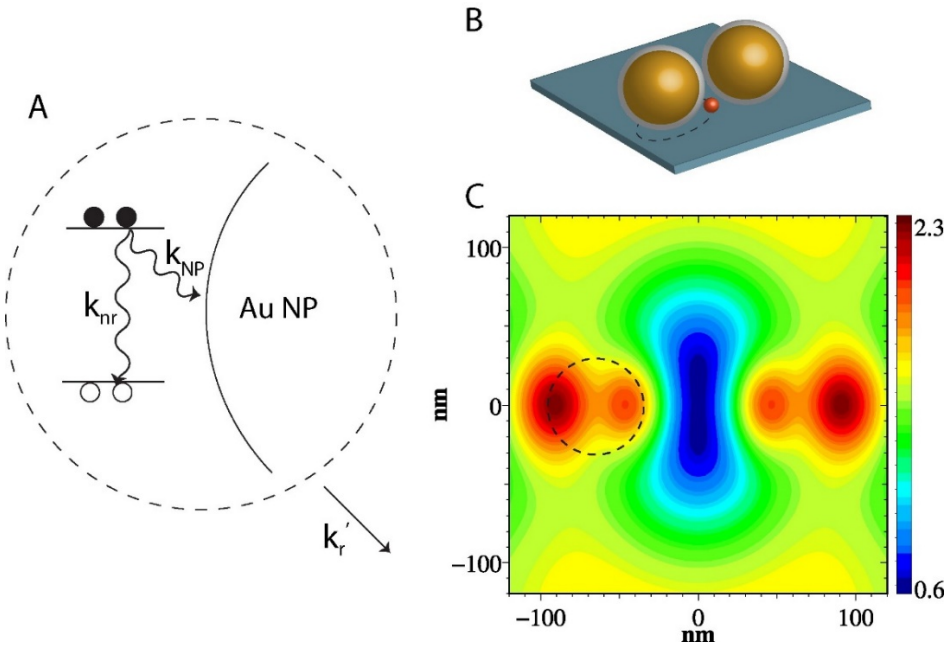


**Figure 2.8**. (A) Scheme of radiative and non-radiative recombination processes in the QD/Au NP system. $k_r$' represents the radiative rate of the QD/Au NP system, $k_{nr}$ represents the intrinsic non-radiative recombination of the QD, and $k_{NP}$ represents the non-radiative energy transfer rate from the QD to the Au NP. (B) Scheme of the geometry of a QD placed near an Au@$SiO_2$ dimer on glass. (C) Electric field distribution of the plane where the QD is positioned. To account for the varying geometries of the QD/Au NP system, the QD is allowed to move along the dashed circles in (B) and (C).

For a QD with a QY of $\eta_1$, the emission intensity of the QD when placed near a metal NP relative to that without a NP can be calculated using

$$\frac{I_1}{I_0} = |E|^2 \frac{\eta'}{\eta_1} = |E|^2 \frac{f_r}{f_t \times \eta_1 + 1 - \eta_1} \quad \text{Equation 2.4}$$

where $I_0$ and $I_1$ are the emission intensities of the QD without and with the presence of a nearby metal NP. $|E|^2$ is the magnitude of the enhancement of the electric field where the QD is

located at a wavelength of 532 nm (the laser excitation wavelength). $|E|^2$ indicates the enhanced excitation rate of the QD due to the presence of the metal NP. The second term on the right side of **Equation 2.4** shows the enhancement factor of the QY of QD without and with the presence of a nearby metal NP. The lifetime change of the QD, $\tau_1/\tau_0$, (after/ before) the presence of Au NP can be calculated using equation

$$\frac{\tau_1}{\tau_0} = \frac{1}{f_t \times \eta_1 + 1 - \eta_1} \qquad \text{Equation 2.5}$$

The above equations were used for the calculations of the excitonic process. For the biexcitonic process, there are no immediate equations available. Since two photons are absorbed by the QD and the interactions between excited QD (dipoles) and metal NPs are fundamentally the same in the excitionic and biexcitonic radiative decay processes, we can reasonably assume that the BX excitation rate is proportional to the fourth power of the electric field and modify the above equations for the biexcitonic process. **Equation 2.4** can be modified as

$$\frac{I_2}{I_0} = |E|^4 \frac{f_r}{f_t \times \eta_2 + 1 - \eta_2} \qquad \text{Equation 2.6}$$

where $I_0$ and $I_2$ are the BX emission intensities of QD without and with the presence of a nearby metal NP, $\eta_2$ represents the QY of BX emission, $|E|$, $f_r$, and $f_t$ have the same meaning as those in **Equation 2.4**. The only change is that $|E|^4$ is used instead of $|E|^2$ in **Equation 2.6** compared to **Equation 2.4**. The model can be extended to multiexcitons, where for the n-th exciton excitation, $|E|^{2n}$ will be used in the above equation. The lifetime change of the BX process can be calculated with **Equation 2.5** by replacing the QY of the X ($\eta_1$) with the QY of BX($\eta_2$). We recognize that the different emission behavior of X and BX could be resolved by analyzing the center and side

peaks in $g^{(2)}$ curve under pulsed excitation when varying the excitation power or <N>, which in turn changes the electric field in **Equation 2.4** and **Equation 2.6**.[29-30] We expect the $g^{(2)}$ dip values of the single QD to vary when the excitation power is increased. Since BX excitation has $|E|^4$ dependence while X excitation has $|E|^2$ dependence from the theoretical study, the relative BX and X QY of single QD will get further enhanced when the excitation power is increased. Experimental attempts were made but the stability of the thin-shell CdSe/CdS QDs under high excitation power without using protective polymer matrix needed to be improved. Future experiments will be carried out by using a pulsed excitation source and packaging the samples under oxygen-free condition.

### *2.4.5 Geometry and interparticle distance dependence*

Using the above equations, we calculated the lifetime, QY, and emission intensity change of both the X and the BX when a single QD is adsorbed to Au@$SiO_2$-10 nm NPs and the results agree well with the experimental measurements. In the calculations, the QY of X is taken as 0.95 as determined by the experimental measurement, and the value of 0.1 is used for the BX QY as measured for similar QD sample in previous work.[44] We have considered two geometries in which the QD is placed near one isolated Au NP or near an Au NP dimer (as seen in **Figure 2.8B** and **Figure 2.8C**). The QD is allowed to move along the dashed circles in **Figure 2.8B** and **Figure 2.8C** to account for varying geometries of the QD/Au NP system. We also modelled the system by including more Au NPs and found that only the Au nanoparticle immediately close to the QD had a major effect on the lifetime, QY, and emission intensity for both the X and BX. The effects of the Au NPs on the QD emission become significantly weaker as they are placed farther away from the QD. The calculated data from an Au NP dimer are used in the discussion below.

In the experiments, it was difficult to determine the position of the QD relative to the axis defined by the center of the two nanoparticles in the dimer Assuming that the QD is randomly distributed, we report here (**Table 2.1**) the calculation results that have been averaged over all possible locations.

**Table 2.1**. Theoretical results of the averaged X, BX intensity, lifetime and quantum yield of a QD on an Au@$SiO_2$ dimer.

| **Average** | **Silica shell thickness = 10 nm** |
|---|---|
| $\|E\|^2$ | 1.9 |
| Rel. X PL Intensity | 0.96 |
| Rel. BX PL Intensity | 4.67 |
| Rel. X PL lifetime | 0.38 |
| Rel. BX PL lifetime | 0.83 |
| X PL QY | 0.48 |
| BX PL QY | 0.13 |
| Ratio (BX QY/ X QY) | 0.27 |

We also averaged over different incident polarizations to account for the unpolarized excitation light used in the experiment (data shown in Table S2 in Supporting Information). The calculations show that X and BX lifetime of the QD on Au@$SiO_2$-10 nm NP is reduced to 0.38 and 0.83 times relative to that of a QD on glass, respectively. The result is consistent with the fast PL decay of QDs on Au@$SiO_2$ substrates in **Figure 2.7**.

**Table 2.2**. Theoretical results of the averaged X, BX intensity, lifetime and quantum yield of a QD on a Au@SiO2 dimer with varying angle of QD relative to the Au-Au NP center axis. The incident polarization is either parallel or perpendicular to the Au-Au NP center axis.

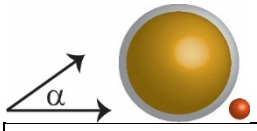


| | **Silica shell thickness = 5 nm** | | | | | **Average** |
|---|---|---|---|---|---|---|
| **α** | **0** | **30** | **45** | **60** | **90** | |
| $\|E\|^2$ | 2.01 | 1.87 | 1.73 | 1.59 | 1.45 | 1.73 |
| **Rel. X PL Intensity** | 0.75 | 0.64 | 0.52 | 0.38 | 0.24 | 0.50 |
| **Rel. BX PL Intensity** | 7.83 | 5.85 | 4.11 | 2.60 | 1.31 | 4.34 |
| **Rel. X PL lifetime** | 0.10 | 0.11 | 0.12 | 0.15 | 0.17 | 0.13 |
| **Rel. BX PL lifetime** | 0.51 | 0.54 | 0.58 | 0.62 | 0.67 | 0.58 |
| **X PL QY** | 0.35 | 0.32 | 0.28 | 0.23 | 0.15 | 0.27 |
| **BX PL QY** | 0.19 | 0.17 | 0.14 | 0.10 | 0.06 | 0.13 |
| **Ratio (BX QY/ X QY)** | 0.55 | 0.52 | 0.48 | 0.45 | 0.40 | 0.48 |

| | Silica shell thickness = 10 nm | | | | | Average |
|---|---|---|---|---|---|---|
| **α** | **0** | **30** | **45** | **60** | **90** | |
| $\|E\|^2$ | 1.74 | 1.68 | 1.63 | 1.57 | 1.52 | 1.63 |
| **Rel. X PL Intensity** | 1.02 | 0.93 | 0.83 | 0.70 | 0.53 | 0.80 |
| **Rel. BX PL Intensity** | 5.82 | 4.68 | 3.58 | 2.52 | 1.49 | 3.62 |
| **Rel. X PL lifetime** | 0.22 | 0.26 | 0.30 | 0.37 | 0.48 | 0.33 |
| **Rel. BX PL lifetime** | 0.73 | 0.77 | 0.81 | 0.85 | 0.90 | 0.81 |
| **X PL QY** | 0.55 | 0.52 | 0.48 | 0.43 | 0.33 | 0.47 |
| **BX PL QY** | 0.19 | 0.16 | 0.14 | 0.10 | 0.07 | 0.13 |
| **Ratio (BX QY/ X QY)** | 0.35 | 0.31 | 0.28 | 0.24 | 0.20 | 0.27 |

In addition, the X emission intensity is reduced to 0.96 of its original value while intensity for the BX is enhanced by a factor of 4.7 for the QD on the Au@$SiO_2$-10 nm NP. Overall, both the lifetimes of X and BX are reduced; however, the emission intensity for X is reduced while for BX is enhanced.

**Table 2.3**. Theoretical results of the averaged X, BX intensity, lifetime and quantum yield of a QD on a Au@$SiO_2$ dimer with varying angle of QD relative to the Au-Au NP center axis. The incident polarization is either parallel or perpendicular to the Au-Au NP center axis.

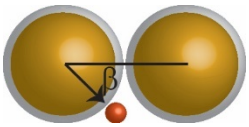


| | **Silica shell thickness = 5 nm** | | | | | | | | | **Ave-rage** |
|---|---|---|---|---|---|---|---|---|---|---|
| **β** | **0** | **30** | **45** | **60** | **90** | **120** | **135** | **150** | **180** | |
| **$\|E\|^2$ (\|\|)** | 1.69 | 1.64 | 1.60 | 1.55 | 1.76 | 1.93 | 2.07 | 2.21 | 1.78 | 1.96 |
| **(⊥)** | 1.79 | 2.00 | 2.20 | 2.39 | 2.54 | 2.34 | 2.17 | 2.02 | 1.88 | |
| **Rel. X PL Int (\|\|)** | 0.86 | 0.77 | 0.64 | 0.45 | 0.25 | 0.54 | 0.71 | 0.83 | 0.94 | 0.70 |
| **(⊥)** | 0.38 | 0.65 | 0.86 | 1.04 | 1.13 | 0.88 | 0.72 | 0.57 | 0.43 | |
| **Rel. BX PL Int (\|\|)** | 7.16 | 5.63 | 4.00 | 2.35 | 1.07 | 3.25 | 5.15 | 7.00 | 9.00 | 5.64 |
| **(⊥)** | 1.93 | 4.37 | 7.34 | 10.6 | 12.8 | 8.16 | 5.62 | 3.77 | 2.33 | |
| **Rel. X PL lifetime (\|\|)** | 0.11 | 0.14 | 0.17 | 0.23 | 0.30 | 0.22 | 0.19 | 0.16 | 0.15 | 0.20 |
| **(⊥)** | 0.29 | 0.22 | 0.18 | 0.15 | 0.14 | 0.17 | 0.20 | 0.24 | 0.28 | |
| **Rel. BX PL lifetime (\|\|)** | 0.54 | 0.59 | 0.66 | 0.73 | 0.79 | 0.72 | 0.67 | 0.64 | 0.61 | 0.68 |
| **(⊥)** | 0.79 | 0.72 | 0.66 | 0.62 | 0.59 | 0.65 | 0.69 | 0.74 | 0.78 | |
| **X PL QY (\|\|)** | 0.48 | 0.45 | 0.38 | 0.28 | 0.15 | 0.29 | 0.35 | 0.38 | 0.40 | 0.36 |
| **(⊥)** | 0.21 | 0.32 | 0.39 | 0.44 | 0.44 | 0.38 | 0.33 | 0.28 | 0.23 | |
| **BX PL QY (\|\|)** | 0.25 | 0.21 | 0.16 | 0.10 | 0.05 | 0.10 | 0.14 | 0.16 | 0.18 | 0.14 |
| **(⊥)** | 0.06 | 0.11 | 0.15 | 0.18 | 0.20 | 0.15 | .0.12 | 0.09 | 0.07 | |
| **Ratio(BXQY/XQY) (\|\|)** | 0.52 | 0.47 | 0.41 | 0.35 | 0.29 | 0.36 | 0.40 | 0.43 | 0.45 | 0.39 |
| **(⊥)** | 0.30 | 0.36 | 0.41 | 0.45 | 0.47 | 0.42 | 0.38 | 0.34 | 0.30 | |
| | **Silica shell thickness = 10 nm** | | | | | | | | | |

| β | 0 | 30 | 45 | 60 | 90 | 120 | 135 | 150 | 180 | Ave-rage |
|---|---|---|---|---|---|---|---|---|---|---|
| $\|E\|^2$ (\|\|) | 1.54 | 1.54 | 2.15 | 1.56 | 1.63 | 1.80 | 1.89 | 1.98 | 2.05 | 1.90 |
| (⊥) | 2.00 | 2.08 | 2.15 | 2.22 | 2.23 | 2.10 | 2.03 | 1.96 | 1.90 | |
| **Rel. X PL Int (\|\|)** | 0.97 | 0.92 | 0.84 | 0.72 | 0.54 | 0.83 | 0.99 | 1.10 | 1.20 | 0.96 |
| **(⊥)** | 0.68 | 0.97 | 1.15 | 1.28 | 1.31 | 1.13 | 1.00 | 0.88 | 0.74 | |
| **Rel. BX PL Int (\|\|)** | 5.17 | 4.33 | 3.39 | 2.36 | 1.45 | 3.15 | 4.56 | 5.92 | 7.31 | 4.67 |
| **(⊥)** | 2.12 | 4.15 | 6.20 | 8.11 | 8.99 | 6.26 | 4.71 | 3.46 | 2.37 | |
| **Rel. X PL lifetime (\|\|)** | 0.21 | 0.26 | 0.32 | 0.43 | 0.58 | 0.43 | 0.35 | 0.30 | 0.27 | 0.38 |
| **(⊥)** | 0.61 | 0.44 | 0.34 | 0.28 | 0.26 | 0.32 | 0.38 | 0.45 | 0.56 | |
| **Rel. BX PL lifetime (\|\|)** | 0.71 | 0.76 | 0.81 | 0.87 | 0.93 | 0.87 | 0.83 | 0.80 | 0.77 | 0.83 |
| **(⊥)** | 0.93 | 0.87 | 0.82 | 0.78 | 0.76 | 0.81 | 0.84 | 0.88 | 0.92 | |
| **X PL QY (\|\|)** | 0.60 | 0.57 | 0.36 | 0.44 | 0.31 | 0.44 | 0.49 | 0.53 | 0.55 | 0.48 |
| **(⊥)** | 0.32 | 0.45 | 0.50 | 0.54 | 0.56 | 0.50 | 0.47 | 0.43 | 0.37 | |
| **BX PL QY (\|\|)** | 0.22 | 0.18 | 0.14 | 0.10 | 0.05 | 0.10 | 0.13 | 0.15 | 0.17 | 0.13 |
| **(⊥)** | 0.05 | 0.10 | 0.13 | 0.17 | 0.18 | 0.14 | 0.11 | 0.09 | 0.06 | |
| **Ratio(BXQY/XQY) (\|\|)** | 0.37 | 0.32 | 0.27 | 0.22 | 0.17 | 0.22 | 0.26 | 0.29 | 0.31 | 0.25 |
| **(⊥)** | 0.16 | 0.22 | 0.26 | 0.30 | 0.32 | 0.28 | 0.24 | 0.21 | 0.18 | |

The interparticle distance between the QDs and Au NP plays an important role in determining the exciton-plasmon interaction. When preparing the single QD study sample, the QDs were spin-coated onto the Au@$SiO_2$ NP substrates, there is chance that the QDs fall on the glass near the Au NPs but not attached to the NPs. Therefore, the interparticle distance between the QD and Au NP not only depends on the silica shell thickness, but also the location of QD relative to the Au NP. To account for the uncertainty in the interparticle distance, we varied the

distance between the QD and the Au NP and calculated the ratio between BX QY and X QY of the single QD as shown in **Figure 2.9**.

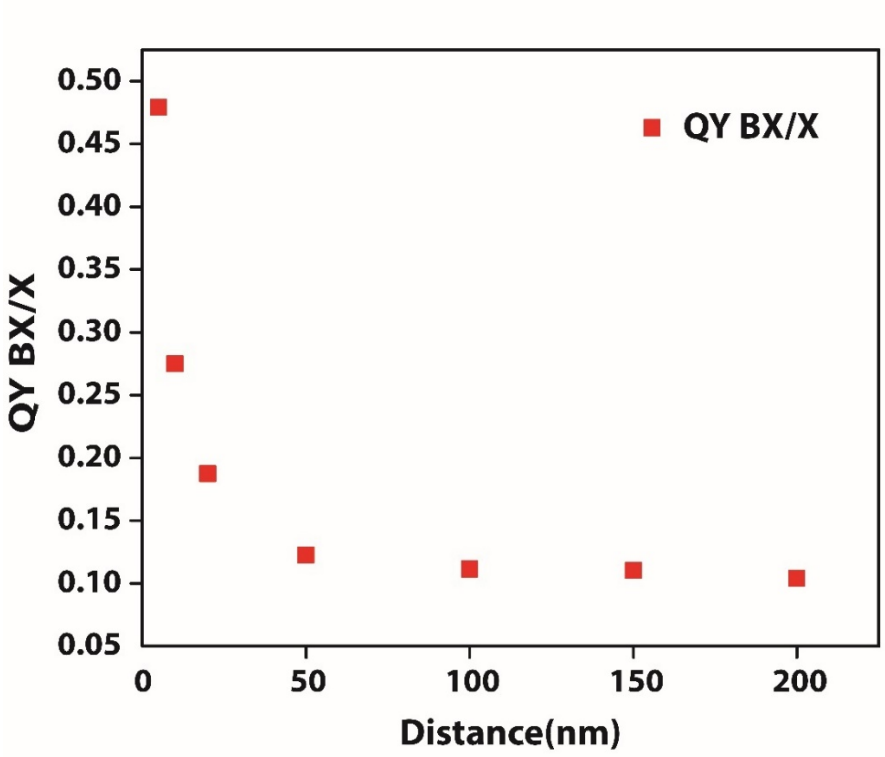


**Figure 2.9**. Theoretically calculated interparticle distance dependence on ratio of BX QY to X QY of a single QD near an Au@$SiO_2$ nanoparticle.

The calculations reveal that $QY_{BX}/QY_X$ is high when the QD is close to the Au NP (interparticle distance $\leq$ 10 nm) and it decreases quickly as the QD is moved away from the Au NP since plasmonic effect is near-field in feature. When the interparticle distance is above 50 nm, the plasmon of Au NP does not have much effect on the ratio between BX and X QYs. The

calculations also explain the broad distribution of $g^2(\tau)$ dip values in **Figure 2.6B** and **Figure 2.6C** respectively.

### *2.4.6 Mechanism of BX emission enhancement*

Our experimental data show that the $QY_{BX}/QY_X$ is significantly enhanced by the plasmon coupling. However, it is not clear what causes this enhancement in the previous reports. In previous attempts, the cause was attributed to the greater enhancement of MX radiative rate compared to that for X[29], or to the smaller reduction of BX QY than the reduction of X QY.[30] Our model suggests that two mechanisms are responsible for the BX emission enhancement, as detailed below.

First, the plasmon coupling results in a higher enhancement of BX excitation relative to X excitation. As mentioned in **Equation 2.4** and **Equation 2.6**, the BX excitation rate is proportional to the fourth power of the local electric field while for X, the excitation rate is proportional to the square of the local electric field. The averaged enhancement of the local electric field, $|E|^2$, is 1.9 for the Au-dimer. The calculations indicate that the excitation rate for the BX is increased about twice as that of the X. Since emission intensity is proportional to excitation rate, the emission intensity of BX is enhanced more than that of X.

Second, the BX QY is increased while X QY is decreased in our QD/Au NP system compared to isolated QDs. From **Equation 2.3**, the change in the QY of X or BX is determined by $f_r$, $f_t$ and its original QY. For the QDs in our study, the QY ($QY=\frac{k_r}{k_r+k_{nr}}$) of X is 0.95, thus the non-radiative rate of X is $k_{nr,X}=0.05k_{r,X}$. Since BX is 2e-2h configuration and X is 1e-1h configuration, the radiative rate of BX $k_{r,BX}=4k_{r,X}$[56]; and the QY of BX is 0.1, thus the non-radiative rate of BX is $k_{nr,BX}=36k_{r,X}$. In the emission process, the radiative rates of X and BX of

the QD/Au NP system are both increased due to the enhanced local electric field around the Au NP at the emission wavelength of the QD. Meanwhile, additional non-radiative process ($k_{NP,X}$ or $k_{NP,BX}$ ) appears due to the energy transfer from the QD to the Au NP. The calculations show that $k_{NP,X} = 1.4k_{r,X}$ and $k_{NP,BX} = 5.6k_{r,BX}$ for QD on Au@$SiO_2$-10 nm. The non-radiative energy transfers are fast compare to the radiative rates, and this non-radiative process has a bigger impact on X QY than on BX QY because $k_{nr,X}$ ( $= 0.05k_{r,X}$) is much smaller than $k_{NP,X}$ ($= 1.4k_{r,X}$) while $k_{nr,BX}$ (=$36k_{r,X}$) is bigger than $k_{NP,BX}$ ($= 5.6k_{r,X}$). Therefore, the X QY is reduced to 0.48 and the BX QY is increased to 0.13 for QDs on Au@$SiO_2$-10 nm relative to those on glass. Hence, the ratio of the BX and X QYs increases from ~ 0.11 to 0.27 when the QDs are placed near Au@$SiO_2$-10 nm NP dimer. The same trend was obtained for QDs on Au@$SiO_2$-5 nm NPs. The increase in the ratio of the BX and X QYs are consistent with the experimental observations.

To summarize, the mechanisms of BX emission enhancement in the QDs near Au@$SiO_2$ NPs are: (1) the greater enhancement in the BX excitation rate than that for X; and (2) increased BX QY but decreased X QY in our system resulting from the exciton-plasmon coupling.

## 2.5 Conclusions

We have studied the plasmonic effect on the BX emission efficiency of single colloidal QDs near Au NPs with distinct plasmon resonance peaks that overlap with both the excitation and emission wavelengths of QDs. Au NPs over coated with a silica shell of controlled thickness of 10 nm (and 5 nm) were used as the plasmonic substrates. The fluorescence blinking statistics of single QDs were modified when they were near Au NPs, and a drastic change in the $g^{(2)}$ dip values was observed. We have developed an electrodynamics model to evaluate the degree of fluorescence intensity enhancement/quenching of single QDs in the presence of plasmonic Au NPs, as well as

the X and BX lifetimes and QYs. It was observed that in the presence of Au NPs, although the QDs exhibited a decrease in their X QY, their BX QY was enhanced. The enhanced BX emission is caused by two main reasons. Firstly, QDs experience a strong enhanced electric field ultimately leading to a greater enhanced excitation rate for BX than for X. And secondly, the presence of the Au NPs opens up non-radiative energy transfer channels between the QD and the Au NPs, and the non-radiative process has a bigger impact on X emission than BX emission. The plasmonic effect due to metal NPs results in changes of X, BX lifetimes and QYs in single QDs. We hope these findings will open up new routes to investigate and manipulate the multiexcitonic processes of QDs, and modify their properties for desired applications.

## 2.6 Acknowledgement

JZ thanks the UCONN Startup Fund and Faculty Large Grant. SZ thanks the National Science Foundation (NSF ECCS-1238738) and the Office of Naval Research (ONR N00014-0-1-1118) for the support of the research.

## 2.7 References

1. Klein, D. L.; Roth, R.; Lim, A. K. L.; Alivisatos, A. P.; McEuen, P. L. A single-electron transistor made from a cadmium selenide nanocrystal. *Nature* **1997,** *389* (6652), 699-701.
2. Biju, V.; Itoh, T.; Ishikawa, M. Delivering quantum dots to cells: bioconjugated quantum dots for targeted and nonspecific extracellular and intracellular imaging. *Chem. Soc. Rev.* **2010,** *39* (8), 3031-3056.
3. Alivisatos, P. The use of nanocrystals in biological detection. *Nat. Biotech.* **2004,** *22* (1), 47-52.
4. Klimov, V. I. Mechanisms for Photogeneration and Recombination of Multiexcitons in Semiconductor Nanocrystals: Implications for Lasing and Solar Energy Conversion. *J. Phys. Chem. B* **2006,** *110* (34), 16827-16845.
5. Klimov, V. I.; Ivanov, S. A.; Nanda, J.; Achermann, M.; Bezel, I.; McGuire, J. A.; Piryatinski, A. Single-exciton optical gain in semiconductor nanocrystals. *Nature* **2007,** *447* (7143), 441-446.

6. Klimov, V. I.; Mikhailovsky, A. A.; Xu, S.; Malko, A.; Hollingsworth, J. A.; Leatherdale, C. A.; Eisler, H.-J.; Bawendi, M. G. Optical Gain and Stimulated Emission in Nanocrystal Quantum Dots. *Science* **2000,** *290* (5490), 314-317.
7. Medintz, I. L.; Uyeda, H. T.; Goldman, E. R.; Mattoussi, H. Quantum dot bioconjugates for imaging, labelling and sensing. *Nat. Mater.* **2005,** *4* (6), 435-446.
8. Robel, I.; Subramanian, V.; Kuno, M.; Kamat, P. V. Quantum Dot Solar Cells. Harvesting Light Energy with CdSe Nanocrystals Molecularly Linked to Mesoscopic TiO2 Films. *J. Am. Chem. Soc.* **2006,** *128* (7), 2385-2393.
9. Knill, E.; Laflamme, R.; Milburn, G. J. A scheme for efficient quantum computation with linear optics. *Nature* **2001,** *409* (6816), 46-52.
10. O'Brien, J. L.; Furusawa, A.; Vuckovic, J. Photonic quantum technologies. *Nat. Photon.* **2009,** *3* (12), 687-695.
11. Achermann, M.; Hollingsworth, J. A.; Klimov, V. I. Multiexcitons confined within a subexcitonic volume: Spectroscopic and dynamical signatures of neutral and charged biexcitons in ultrasmall semiconductor nanocrystals. *Phys. Rev. B* **2003,** *68* (24), 245302.
12. Nozik, A. J. Multiple exciton generation in semiconductor quantum dots. *Chem. Phys. Lett.* **2008,** *457* (1–3), 3-11.
13. Shabaev, A.; Efros, A. L.; Nozik, A. J. Multiexciton Generation by a Single Photon in Nanocrystals. *Nano Lett.* **2006,** *6* (12), 2856-2863.
14. Nair, G.; Chang, L.-Y.; Geyer, S. M.; Bawendi, M. G. Perspective on the Prospects of a Carrier Multiplication Nanocrystal Solar Cell. *Nano Lett.* **2011,** *11* (5), 2145-2151.
15. Cohen-Hoshen, E.; Bryant, G. W.; Pinkas, I.; Sperling, J.; Bar-Joseph, I. Exciton–Plasmon Interactions in Quantum Dot–Gold Nanoparticle Structures. *Nano Lett.* **2012,** *12* (8), 4260-4264.
16. Chan, Y.-H.; Chen, J.; Wark, S. E.; Skiles, S. L.; Son, D. H.; Batteas, J. D. Using Patterned Arrays of Metal Nanoparticles to Probe Plasmon Enhanced Luminescence of CdSe Quantum Dots. *ACS Nano* **2009,** *3* (7), 1735-1744.
17. Achermann, M. Exciton−Plasmon Interactions in Metal−Semiconductor Nanostructures. *J. Phys. Chem. Lett.* **2010,** *1* (19), 2837-2843.
18. Govorov, A. O.; Bryant, G. W.; Zhang, W.; Skeini, T.; Lee, J.; Kotov, N. A.; Slocik, J. M.; Naik, R. R. Exciton−Plasmon Interaction and Hybrid Excitons in Semiconductor−Metal Nanoparticle Assemblies. *Nano Lett.* **2006,** *6* (5), 984-994.
19. Ozel, T.; Hernandez-Martinez, P. L.; Mutlugun, E.; Akin, O.; Nizamoglu, S.; Ozel, I. O.; Zhang, Q.; Xiong, Q.; Demir, H. V. Observation of Selective Plasmon-Exciton Coupling in Nonradiative Energy Transfer: Donor-Selective versus Acceptor-Selective Plexcitons. *Nano Lett.* **2013,** *13* (7), 3065-3072.
20. Ma, X.; Fletcher, K.; Kipp, T.; Grzelczak, M. P.; Wang, Z.; Guerrero-Martínez, A.; Pastoriza-Santos, I.; Kornowski, A.; Liz-Marzán, L. M.; Mews, A. Photoluminescence of Individual Au/CdSe Nanocrystal Complexes with Variable Interparticle Distances. *J. Phys. Chem. Lett.* **2011,** *2* (19), 2466-2471.
21. Pons, T.; Medintz, I. L.; Sapsford, K. E.; Higashiya, S.; Grimes, A. F.; English, D. S.; Mattoussi, H. On the Quenching of Semiconductor Quantum Dot Photoluminescence by Proximal Gold Nanoparticles. *Nano Lett.* **2007,** *7* (10), 3157-3164.
22. Yuan, C. T.; Yu, P.; Ko, H. C.; Huang, J.; Tang, J. Antibunching Single-Photon Emission and Blinking Suppression of CdSe/ZnS Quantum Dots. *ACS Nano* **2009,** *3* (10), 3051-3056.

23. Kinkhabwala, A.; Yu, Z.; Fan, S.; Avlasevich, Y.; Mullen, K.; Moerner, W. E. Large single-molecule fluorescence enhancements produced by a bowtie nanoantenna. *Nat. Photon.* **2009,** *3* (11), 654-657.
24. Fu, Y.; Zhang, J.; Lakowicz, J. R. Silver-enhanced fluorescence emission of single quantum dot nanocomposites. *Chem. Commun.* **2009,** (3), 313-315.
25. Gómez, D. E.; Vernon, K. C.; Mulvaney, P.; Davis, T. J. Surface Plasmon Mediated Strong Exciton−Photon Coupling in Semiconductor Nanocrystals. *Nano Lett.* **2009,** *10* (1), 274-278.
26. Ratchford, D.; Shafiei, F.; Kim, S.; Gray, S. K.; Li, X. Manipulating Coupling between a Single Semiconductor Quantum Dot and Single Gold Nanoparticle. *Nano Lett.* **2011,** *11* (3), 1049-1054.
27. Samanta, A.; Zhou, Y.; Zou, S.; Yan, H.; Liu, Y. Fluorescence Quenching of Quantum Dots by Gold Nanoparticles: A Potential Long Range Spectroscopic Ruler. *Nano Lett.* **2014,** *14* (9), 5052-5057.
28. Funston, A. M.; Jasieniak, J. J.; Mulvaney, P. Complete Quenching of CdSe Nanocrystal Photoluminescence by Single Dye Molecules. *Adv. Mater.* **2008,** *20* (22), 4274-4280.
29. LeBlanc, S. J.; McClanahan, M. R.; Jones, M.; Moyer, P. J. Enhancement of Multiphoton Emission from Single CdSe Quantum Dots Coupled to Gold Films. *Nano Lett.* **2013,** *13* (4), 1662-1669.
30. Park, Y.-S.; Ghosh, Y.; Chen, Y.; Piryatinski, A.; Xu, P.; Mack, N. H.; Wang, H.-L.; Klimov, V. I.; Hollingsworth, J. A.; Htoon, H. Super-Poissonian Statistics of Photon Emission from Single CdSe-CdS Core-Shell Nanocrystals Coupled to Metal Nanostructures. *Phys. Rev. Lett.* **2013,** *110* (11), 117401.
31. Reineck, P.; Gómez, D.; Ng, S. H.; Karg, M.; Bell, T.; Mulvaney, P.; Bach, U. Distance and Wavelength Dependent Quenching of Molecular Fluorescence by Au@SiO2 Core–Shell Nanoparticles. *ACS Nano* **2013,** *7* (8), 6636-6648.
32. Munechika, K.; Chen, Y.; Tillack, A. F.; Kulkarni, A. P.; Plante, I. J.-L.; Munro, A. M.; Ginger, D. S. Spectral Control of Plasmonic Emission Enhancement from Quantum Dots near Single Silver Nanoprisms. *Nano Lett.* **2010,** *10* (7), 2598-2603.
33. Munechika, K.; Chen, Y.; Tillack, A. F.; Kulkarni, A. P.; Jen-La Plante, I.; Munro, A. M.; Ginger, D. S. Quantum Dot/Plasmonic Nanoparticle Metachromophores with Quantum Yields That Vary with Excitation Wavelength. *Nano Lett.* **2011,** *11* (7), 2725-2730.
34. Chen, Y.; Munechika, K.; Jen-La Plante, I.; Munro, A. M.; Skrabalak, S. E.; Xia, Y.; Ginger, D. S. Excitation enhancement of CdSe quantum dots by single metal nanoparticles. *Appl. Phys. Lett.* **2008,** *93* (5), 053106.
35. Nair, G.; Zhao, J.; Bawendi, M. G. Biexciton Quantum Yield of Single Semiconductor Nanocrystals from Photon Statistics. *Nano Lett.* **2011,** *11* (3), 1136-1140.
36. G.Frens. Controlled Nucleation for the Regulation of the Particle Size in Monodisperse Gold Suspensions. *Nature* **1973,** *241*, 20-22.
37. Lim, B.; Kobayashi, H.; Yu, T.; Wang, J.; Kim, M. J.; Li, Z.-Y.; Rycenga, M.; Xia, Y. Synthesis of Pd−Au Bimetallic Nanocrystals via Controlled Overgrowth. *J. Am. Chem. Soc.* **2010,** *132* (8), 2506-2507.
38. Kiraz, A.; Fälth, S.; Becher, C.; Gayral, B.; Schoenfeld, W. V.; Petroff, P. M.; Zhang, L.; Hu, E.; Imamoğlu, A. Photon correlation spectroscopy of a single quantum dot. *Phys. Rev. B* **2002,** *65* (16), 161303.

39. Press, D.; Götzinger, S.; Reitzenstein, S.; Hofmann, C.; Löffler, A.; Kamp, M.; Forchel, A.; Yamamoto, Y. Photon Antibunching from a Single Quantum-Dot-Microcavity System in the Strong Coupling Regime. *Phys. Rev. Lett.* **2007,** *98* (11), 117402.
40. R.Hanbury Brown, R. Q. T. Correlation between Photons in two Coherent Beams of Light. *Nature* **1956,** *177* (4497), 27-29.
41. Fernee, M. J.; Tamarat, P.; Lounis, B. Spectroscopy of single nanocrystals. *Chem. Soc. Rev.* **2014,** *43* (4), 1311-1337.
42. Lounis, B.; Bechtel, H. A.; Gerion, D.; Alivisatos, P.; Moerner, W. E. Photon antibunching in single CdSe/ZnS quantum dot fluorescence. *Chem. Phys. Lett.* **2000,** *329* (5–6), 399-404.
43. Park, Y. S.; Malko, A. V.; Vela, J.; Chen, Y.; Ghosh, Y.; García-Santamaría, F.; Hollingsworth, J. A.; Klimov, V. I.; Htoon, H. Near-Unity Quantum Yields of Biexciton Emission from Nanocrystals Measured Using Single-Particle Spectroscopy. *Phys. Rev. Lett.* **2011,** *106* (18), 187401.
44. Zhao, J.; Chen, O.; Strasfeld, D. B.; Bawendi, M. G. Biexciton Quantum Yield Heterogeneities in Single CdSe (CdS) Core (Shell) Nanocrystals and Its Correlation to Exciton Blinking. *Nano Lett.* **2012,** *12* (9), 4477-4483.
45. Malko, A. V.; Park, Y.-S.; Sampat, S.; Galland, C.; Vela, J.; Chen, Y.; Hollingsworth, J. A.; Klimov, V. I.; Htoon, H. Pump-Intensity- and Shell-Thickness-Dependent Evolution of Photoluminescence Blinking in Individual Core/Shell CdSe/CdS Nanocrystals. *Nano Lett.* **2011,** *11* (12), 5213-5218.
46. Fisher, B.; Caruge, J. M.; Zehnder, D.; Bawendi, M. Room-Temperature Ordered Photon Emission from Multiexciton States in Single CdSe Core-Shell Nanocrystals. *Phys. Rev. Lett.* **2005,** *94* (8), 087403.
47. Vion, C.; Spinicelli, P.; Coolen, L.; Schwob, C.; Frigerio, J.-M.; Hermier, J.-P.; Maître, A. Controlled modification of single colloidal CdSe/ZnS nanocrystal fluorescence through interactions with a gold surface. *Opt. Express* **2010,** *18* (7), 7440-7455.
48. Thomas, A.; Valéry, Z.; Oliver, B. Visible single-photon generation from semiconductor quantum dots. *New J. Phys.* **2004,** *6* (1), 90.
49. Wu, X.-W.; Gong, M.; Dong, C.-H.; Cui, J.-M.; Yang, Y.; Sun, F.-W.; Han, Z.-F.; Guo, G.-C. Anti-bunching and luminescence blinking suppression from plasmon-interacted single CdSe/ZnS quantum dot. *Opt. Express* **2010,** *18* (6), 6340-6346.
50. Zwiller, V.; Jonsson, P.; Blom, H.; Jeppesen, S.; Pistol, M.-E.; Samuelson, L.; Katznelson, A. A.; Kotelnikov, E. Y.; Evtikhiev, V.; Björk, G. Correlation spectroscopy of excitons and biexcitons on a single quantum dot. *Phys. Rev. A* **2002,** *66* (5), 053814.
51. Peterson, J. J.; Nesbitt, D. J. Modified Power Law Behavior in Quantum Dot Blinking: A Novel Role for Biexcitons and Auger Ionization. *Nano Lett.* **2008,** *9* (1), 338-345.
52. Zwiller, V.; Blom, H.; Jonsson, P.; Panev, N.; Jeppesen, S.; Tsegaye, T.; Goobar, E.; Pistol, M.-E.; Samuelson, L.; Björk, G. Single quantum dots emit single photons at a time: Antibunching experiments. *Appl. Phys. Lett.* **2001,** *78* (17), 2476-2478.
53. Wang, H.; Zou, S. A generalized electrodynamics model for surface enhanced Raman scattering and enhanced/quenched fluorescence calculations. *RSC Adv.* **2013,** *3* (44), 21489-21493.
54. Weitz, D. A.; Garoff, S.; Gersten, J. I.; Nitzan, A. The enhancement of Raman scattering, resonance Raman scattering, and fluorescence from molecules adsorbed on a rough silver surface. *J. Chem. Phys.* **1983,** *78* (9), 5324-5338.

# Chapter Three .

# Excitation Wavelength Dependent Multiexciton Emission of Single Quantum Dots near Gold Nanostructures

## 3.1. Abstract

The change in photon emission statistics of single CdSe/CdS core/shell quantum dots on dielectric modified gold nanoparticle substrates as a function of excitation wavelength has been investigated in this study. Upon coupling to metal substrates, even at the low excitation pulse regime, we directly observed a significant change in photoluminescence emission behavior of single QDs getting transformed from their usual incomplete photon antibunching (sub-Poissonian distribution) to a complete bunching (super-Poissonian distribution) as the excitation is changed from "off" resonance to "on" resonance condition. Further theoretical studies were performed based on electrodynamics modeling which suggested that such a hybrid system when excited at "on" resonance condition, because of a more pronounced electric field enhancement due to Au NPs, it resulted in an increased population of higher order excited states of the QDs effectively modifying the photon flux and emission statistics. This was also manifested as the additional peaks appearing in PL spectra of single QDs even at low excitation flux regime. These results provided evidence that not only the plasmonic nanostructures but also the excitation wavelength can play an effective role in controlling and manipulating the photon emission statistics of single QDs. Manipulating multiexciton-plasmon interactions in hybrid complexes like this could possibly open up new doors for applications such as entangled photon pair generation, broadband tunable plasmon-assisted lasers or even plasmon-enhanced solar cells.

## 3.2. Introduction

Colloidal quantum dots (QDs) have been under the spotlight of various research fields over the past few decades because of their unique light absorption and emission properties. In particular, the broad absorption and high photoluminescence (PL) quantum yield (QY) offered by QDs make them promising building blocks for light emitting devices, and desirable fluorescent probes for biological imaging and tracking.[1-7] Nowadays, QDs with near-unity single exciton PL QY have been routinely synthesized owing to the advancement in the synthetic approaches of QDs. However, the PL QY of multiexcitons in typical QDs is often low due to the fast non-radiative Auger recombination, limiting the applications of QDs for lasing and quantum communication.[8-10] An effective method to increase the multiexciton QY of QDs is to couple them to metal nanoparticles (MNPs). [11-15] Multiexciton emission of QDs can be enhanced when QDs are deposited on roughened gold and silver thin films, as well as on silica-coated silver and gold nanoparticles.[11, 13, 16-18] This emission enhancement originates from the interaction of multiexcitons in QDs with the highly increased electric field around the MNPs, which is due to the excitation of localized surface plasmon resonance (LSPR) in the MNPs. The exciton-plasmon interaction can even change the statistical distribution of emitted photons of single QDs from sub-Poissonian to super-Poissonian distribution, as reported by Park et al.[13] Although strong plasmonic effect on the radiative and non-radiative recombination of multiexcitons has been observed by several groups independently, inconsistency exists in the literature about the multiexciton-plasmon interaction mechanism.[11, 13-14, 18-20] Moreover, since the electric field associated with plasmon is highly dependent on the excitation wavelength, we expect the excitation conditions will strongly

impact the multiexciton-plasmon interaction and the photon statistics of single QDs. However, there is currently a lack of such studies.

Usually, photons emitted by a single QD follow sub-Poissonian photon statistics, or are anti-bunched.[21-25] Photon statistics (how photons are distributed in time) of a single QD can be conveniently determined by measuring the second order photon intensity correlation function $g^{(2)}(\tau)$. The $g^{(2)}$ function has been directly manifested to represent the biexciton QY of single QDs in previous work by Nair et al.[26] That is, the biexciton QY of single QDs can be calculated from the relative area ratio of the center ($\tau$=0) to side ($\tau$= time interval between pulses) peaks under pulsed excitation at low pump fluence, where the averaged photon absorbed per pulse $\langle N \rangle \rightarrow 0$. This method has been applied in the previous studies on multiexciton emission of single QDs near metal films or nanoparticles.[11, 13, 27-29]

However, when QDs are located close to MNPs, the absorption cross section is greatly increased due to the enhanced electric field from plasmons, thus resulting in an increased $\langle N \rangle$. Even the pump power from the excitation source is maintained low, the probability of forming multiexcitons in QDs near MNPs is much higher comparing to that of the isolated QDs. In this scenario, it becomes difficult to determine the biexciton QY of single QDs near MNPs without performing any population modeling.[26] Thus, the previous model of using $g^{(2)}(\tau)$ function to calculate biexciton QY of single QD needs to be revisited for the QDs near MNPs.

In this work, we investigated how altering the excitation wavelength could promote multiexciton emission of single QDs close to dielectric-modified Au NPs even under low excitation fluence. Surprisingly, we found that by simply varying the excitation wavelength from "off" to "on" plasmon resonance, the statistics of photons emitted by single QDs near Au NPs

changed drastically from a sub-Poissonian to a super-Poissonian distribution. To understand this phenomenon, we re-evaluated the relationship between $g^{(2)}(\tau)$ function and multiexciton emission QY of QDs in the hybrid QD-MNP system. Electrodynamics modeling was also applied to quantitatively determine the absorption and emission rates of single and biexcitons at "on" and "off" plasmon resonance conditions.

## 3.3. Experimental Methods

### *3.3.1. Gold Nanoparticle Synthesis*

A two-step seed mediated process was used to prepare 120nm gold colloids, as previously reported.[30-31] The first step involves the reduction of hydrogen tetrachloroaurate (III) trihydrate ($HAuCl_4$, Acros Organics) with sodium citrate (Fisher Scientific) by the Frens' Method. 1060μL of $HAuCl_4$ (0.0254M) solution was brought to a boil in 99mL of deionized (DI) water while stirring. Once boiling, 1000 μL of sodium citrate solution (0.0388M) was added to the boiling solution. After 15 minutes, the solution was allowed to cool to room temperature. 4mL of the as-made nanoparticle solution synthesized in step one was added to 52mL of DI water. The seeds were stirred at room temperature for one hour with 1000 μL sodium citrate (0.0388M), 900μL $HAuCl_4$ (0.0254M), and 1400 μL hydroxylamine hydrochloride (0.0101M) (Sigma-Aldrich). The nanoparticles were used directly from the growth solution.

### *3.3.2. CdSe/CdS QD synthesis*

CdSe/CdS core/shell QDs were synthesized following a modified procedure developed by Chen et al.[32] The photoluminescence (PL) quantum yield (QY) of these QDs in Toluene is 94.9%, as determined by comparison to Rhodamine B in ethanol. The shape and size distribution of the QDs was characterized using a JEOL2010 transmission electron microscope (TEM) operated at 200kV.

### *3.3.3. LSPR Substrate Preparation*

The glass substrates were prepared using commercially available glass coverslips (Fisher Scientific, 22x22mm, #2). The glass coverslips were cleaned by sonicating in a dilute alkaline detergent for 15 minutes. They were sonicated in deionized (DI) water several times to completely remove the detergent. The coverslips were further cleaned by immersing into a 1:1 (v/v) solution of hydrochloric acid and methanol for 30 minutes. They were thoroughly rinsed with DI water until a neutral pH was obtained. After cleaning, the glass coverslips were immersed in a 10% (v/v) solution of 3-aminopropyltriethoxysilane (APTES, Sigma-Aldrich) in ethanol for 20 minutes to silanize the surface. The coverslips were sonicated in ethanol several times and annealed in the oven at 120°C for 3 hours. The silanized glass substrates were immersed in the Au NP solution overnight so the nanoparticles adsorbed to the glass substrate. After immobilization of the gold NPs on glass, the substrate was rinsed with DI water to remove any excess gold nanoparticles, then dried in air.

### *3.3.4. Atomic Layer Deposition on Gold Nanoparticle Substrates*

Alumina films of ~20nm thickness were fabricated on the gold nanoparticle substrates inside an ALD reactor constructed from stainless steel components. Trimethylaluminum (TMA) and deionized $H_2O$ vapors were alternately pulsed through the reaction chamber, utilizing $N_2$ as the carrier gas, at a mass flow rate of 360 sccm (standard cubic center per minute), a pressure of 1 Torr, and a growth temperature of 50 °C. One complete ALD cycle takes ~42 s and includes four steps: (1) TMA reactant exposure time, 1 s; (2) $N_2$ purge following TMA exposure time, 10 s; (3) $H_2O$ reactant exposure time, 1 s; and (4) $N_2$ purge following $H_2O$ exposure time, 30 s. Long purge times are necessary at low temperatures to prevent chemical vapor deposition of alumina. The thickness of alumina on Au surfaces was calculated based on a layer-by-layer growth of alumina with an average growth rate ∼1 Å/cycle.

### *3.3.5. Structural Characterization of Alumina-Modified Gold Nanoparticle Substrates*

A UV-vis spectrometer (Cary 60, Agilent Technologies) was used to determine the extinction spectrum of the gold nanoparticles in solution. A home-built LSPR setup was used to measure the UV-vis extinction spectra of the immobilized AuNPs on the glass substrate. In this setup, a halogen light source was fiber coupled and focused with convex lens on the Au NPs to a spot of ~ 0.5 cm diameter. The transmitted light after passing through the Au NPs was focused onto fiber coupled a spectrometer (QE65 Pro, Ocean Optics) by placing the Au NP substrates into a home-built flow cell. The scanning electron microscopy (SEM) image of the Au NPs on glass

substrates was obtained using a JEOL JSM-6330F scanning electron microscope(SEM) operated with a resolution of 1.5nm at 15kV.

### *3.3.6. Single QD Optical Characterization*

Single particle optical measurements were performed using a home-built confocal epifluorescence Nikon Ti-U microscope equipped with a piezo-scanning XY-stage (PI 320, Physik Instrumente). To excite our nanocrystal sample at different excitation wavelengths, a supercontinuum pulsed laser (model Solea, PicoQuant, ~100-120ps pulse duration, 2.5MHz repetition rate) was used and the emission signal was collected through a 100x oil-immersion objective (N.A.=1.3). The emitted light was allowed to pass through 50/50 non-polarizing beam-splitter and spectrally filtered using a 630/60 band-pass filters (Thorlabs) before being directed onto two single photon detectors (τ-SPAD, Pico-Quant, average time resolution is ~600ps) oriented in a Hanbury-Brown Twiss detection geometry for characterizing the emission photon statistics. Time-dependent photon correlation histograms and simultaneous acquisition of emission intensity-time traces were performed using a time correlated single photon counting system PicoHarp-300 (PicoQuant) operated in a time-tagged time-resolved (TTTR) mode with a timing resolution of 32ps. All the measurements were performed at room temperature. The $g^2(\tau)$ data were processed with a commercial Sympho Time 64 software (Picoquant).

The PL spectra of single QDs dispersed on both glass and on Au substrates were simultaneously monitored by directing the emission signal to an imaging spectrometer(IsoPlane SCT 320) mounted with a charge coupled device(CCD, Pixis 1024,Princeton Instruments).The CCD spectral resolution of our setup when using a 150 lines/mm grating around the centre

wavelength of 600nm is approximately 0.565nm.The emitted signal was allowed to pass through the a 600nm long-pass filter in order to cut off the excitation light and obtain a spectrally resolved PL data. Considering the average signal to noise ratio from the samples, for both excitation wavelength and pump power dependent PL measurements, we typically varied the acquisition times between 15-30 seconds. The entrance slit width was adjusted accordingly which served as a means to minimize the influence of other QDs present outside the central wavelength region. All data from confocal microscopic PL measurements were collected using an in-built WinSpec software.

### 3.4. Results and Discussion

The system we studied is composed of individual CdSe/CdS core/shell QDs dispersed on a substrate of Au NPs coated with alumina. **Figure 3.1A** shows the schematic representation of the substrate preparation.

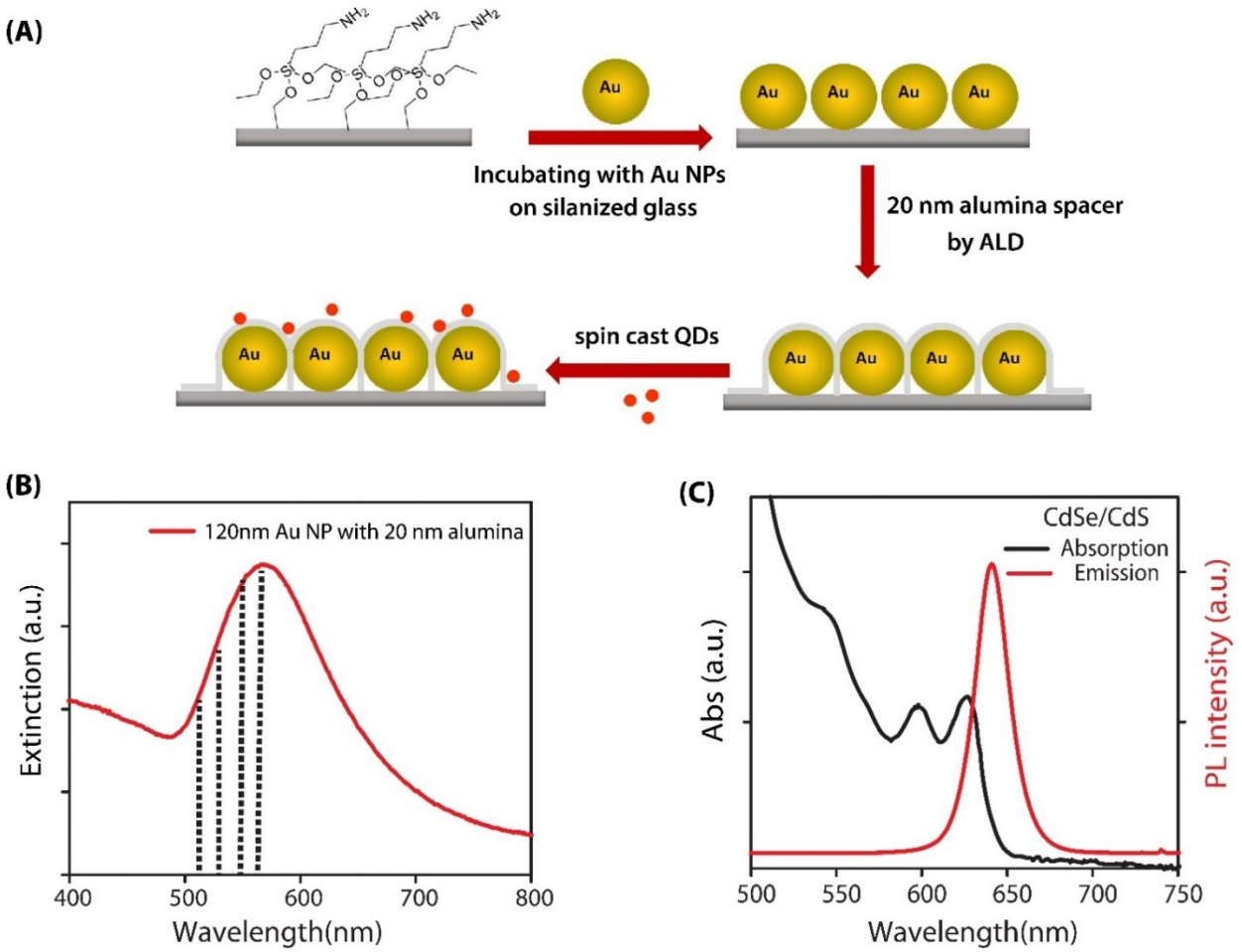


**Figure 3.1**. (A) Schematic representation of substrate preparation for single particle optical measurements. (B) Absorption and emission spectra of CdSe/CdS QDs dispersed in hexane. (C) Extinction spectra of 120 nm Au nanoparticles with 20 nm thick alumina spacer (dotted lines represent different excitation wavelengths used for the single particle studies at 510 nm,530 nm,550 nm and 580 nm).

The Au NPs substrates were fabricated by immobilizing 120 nm Au NPs on glass, following a previously developed protocol. A 20-nm thick alumina layer was then grown over the Au NPs using atomic layer deposition to prevent complete quenching of QD emission. Core/shell CdSe/CdS QDs with a quantum yield of 95% in hexane were diluted and spun-cast onto the Au

NP-alumina substrate. **Figure 3.1C** shows the absorption and PL spectra of the CdSe/CdS QDs dispersed in hexane. The absorption spectrum shows several distinct excitonic features associated with discrete electronic transitions in the QDs. The emission spectrum is narrow (FWHM~21 nm) with a peak at 638 nm. The Au NP-alumina substrate has a LSPR peak at ~590 nm as shown in **Figure 3.1B**. The LSPR of the Au NPs has a substantial overlap with the PL spectrum of the QDs, leading to a strong exciton-plasmon interaction. The dotted lines on the extinction spectra in **Figure 3.1B** represent different laser excitation wavelengths (510, 530, 550 and 580 nm) used in our study. **Figure 3.2** shows the high resolution TEM and SEM images of CdSe/CdS and 20nm thick alumina modified gold nanoparticle substrates respectively.

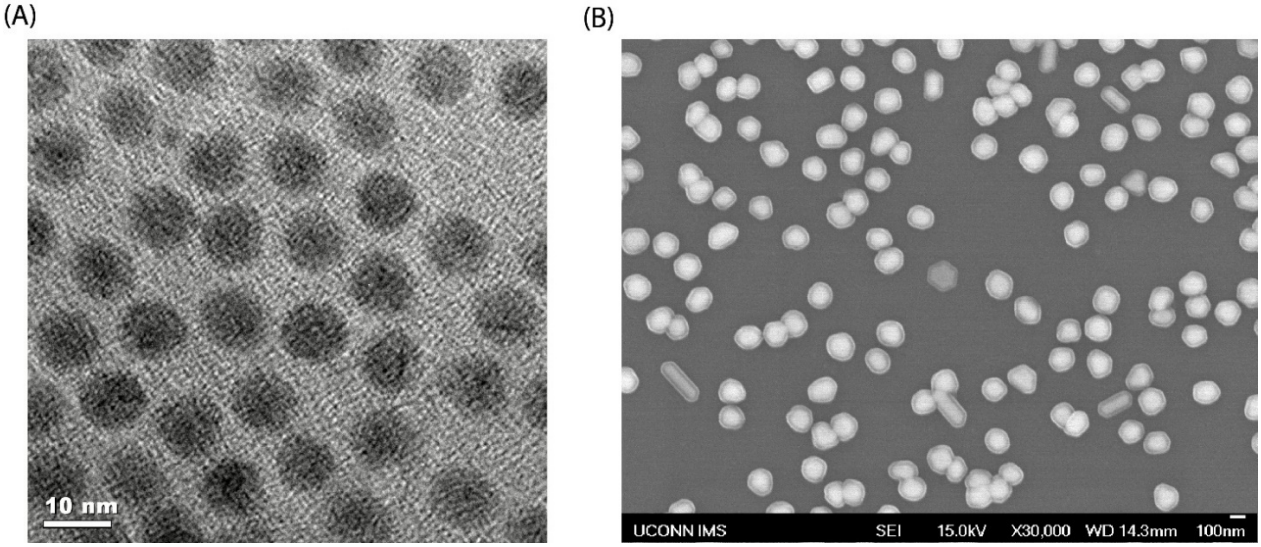


**Figure 3.2**. (A) HR-TEM image of CdSe/CdS nanocrystals with an average calculated diameter of 9.2 ± 1.2 nm (B) SEM image of 20nm alumina modified gold nanoparticle substrates

To obtain the $g^{(2)}(\tau)$ function of the QDs as well as the PL intensity time traces, single QDs on Au NP/alumina substrate were excited with a pump power of 50 nW at 510, 530, 550 and 580 nm. $\langle N \rangle$ was estimated to be 0.045 for 510 nm, 0.027 for 530 nm, 0.023 for 550 nm, and 0.021 for 580 nm excitations. To ensure the QDs did not undergo photon degradation during the measurements, we varied the order of which excitation wavelength the QDs were exposed to and no obvious difference in the PL intensity time trace was observed.

**Figure 3.3** shows the $g^{(2)}(\tau)$ functions with the corresponding PL time traces for a single QD on Au NPs substrates acquired at 510 nm,530 nm,550 nm and 580 nm excitation, respectively. The PL time traces show clearly binary-state (on and off) blinking, confirming that the signal is from a single QD. From the $g^{(2)}(\tau)$ functions, there is a drastic increase of the center peaks (at $\tau$ = 0 ns) when the excitation wavelength was increased from 510 nm (off-resonance) to 580 nm (on-resonance). The high center peak of the $g^{(2)}(\tau)$ function shows that the multiexciton emission of QDs is highly enhanced when they are close to MNPs, consistent with previous reports.[11, 13-14] Moreover, the intensity of the center peak became even higher than that of the side peak at 580 nm excitation.

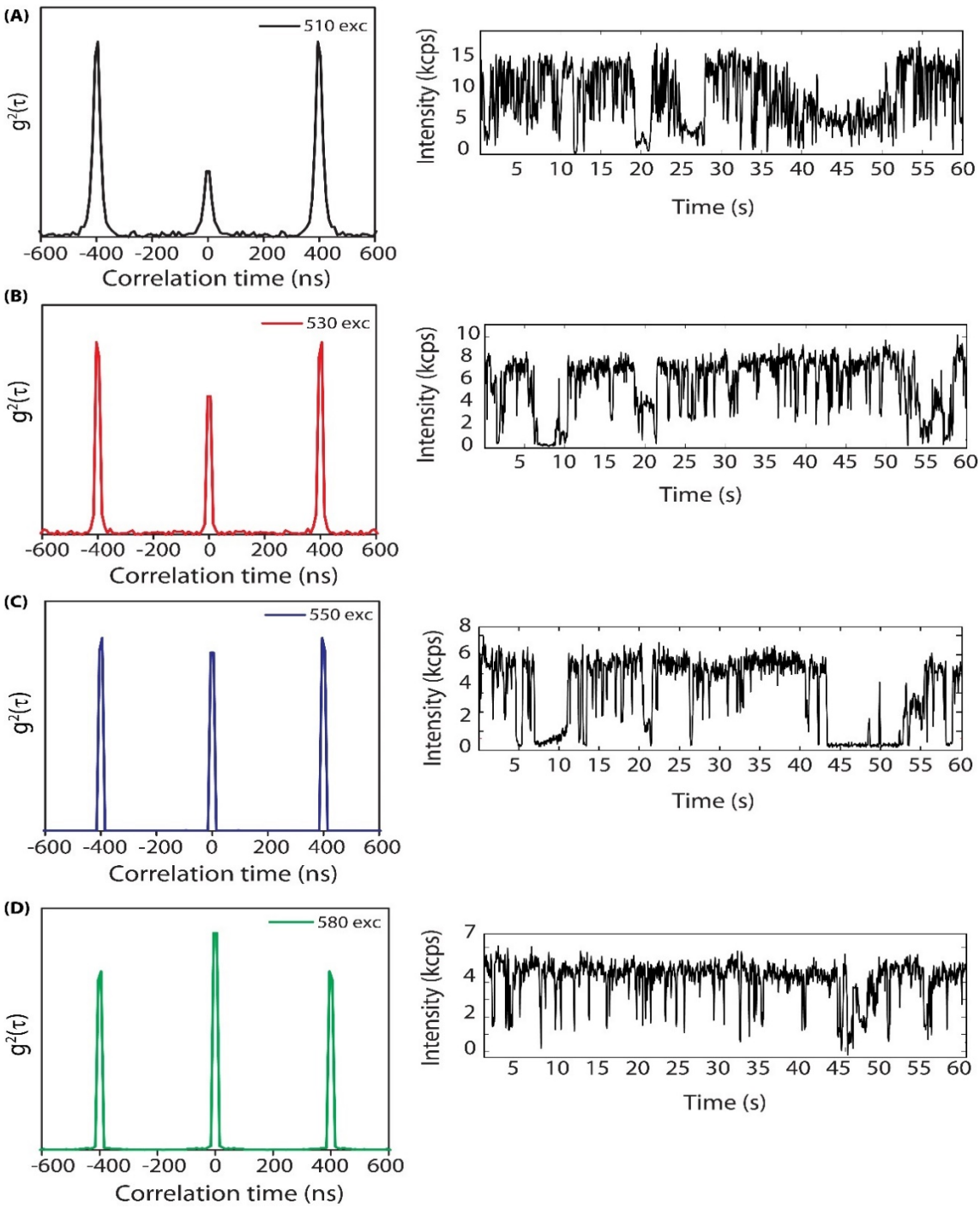


**Figure 3.3**. Representative time-dependent second order photon intensity correlation functions ($g^{(2)}(\tau)$ functions) and the corresponding intensity-time traces of a single QD deposited on Au NP with 20 nm alumina substrates at excitation wavelengths (A) 510 nm (B) 530 nm (C) 550 nm and (D) 580nm.

Additional representative photon correlation histograms from individual QDs on Au NP substrates acquired under different excitation wavelengths are shown below in **Figure 3.4**. The data consistently exhibited the distinct change i.e. enhancement of the center to side peak area ratio as excited closer to the plasmon resonance frequency.

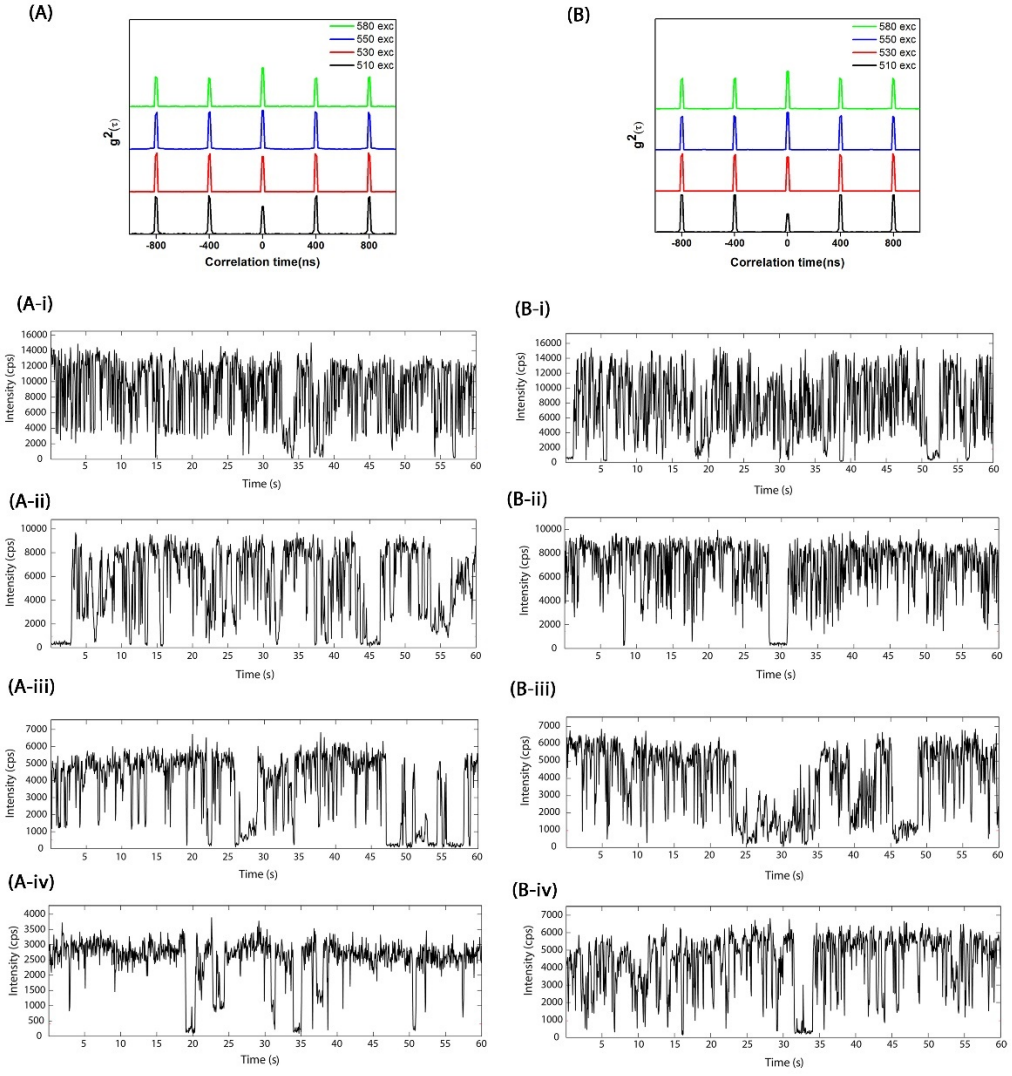


**Figure 3.4**. Photon correlation histograms and corresponding intensity-time traces for two representative single QDs on Au NP substrates at excitation wavelengths (510, 530, 550, 580nm)

In contrast, in the control experiments performed on single QDs on glass as illustrated in **Figure 3.5**, the $g^{(2)}(\tau)$ functions show no particular correlation or dependence on excitation wavelengths.

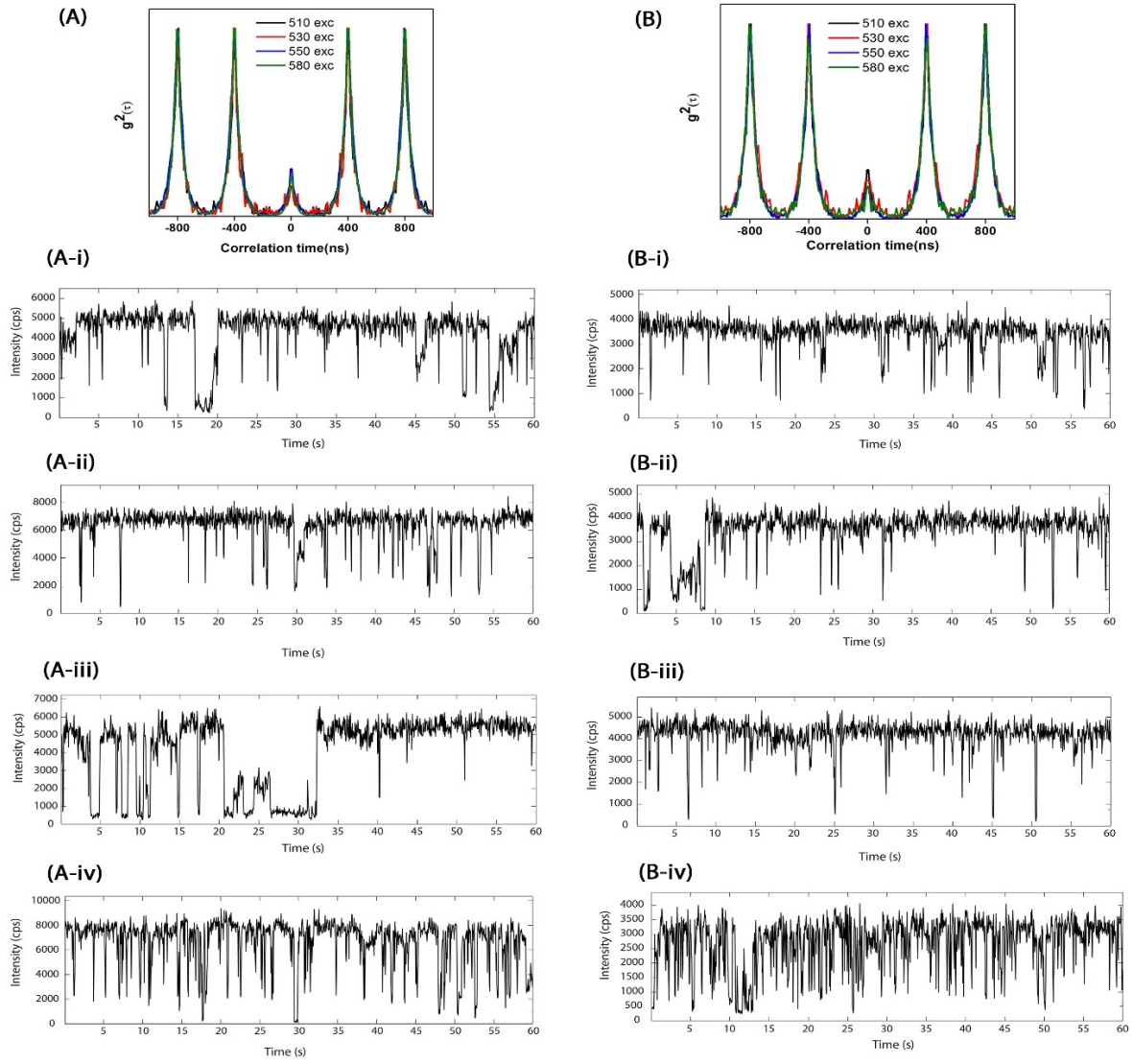


**Figure 3.5**. Photon correlation histograms and corresponding intensity-time traces for two representative single QDs on bare glass substrates at excitation wavelengths (510, 530, 550, 580nm)

In order to quantitatively evaluate the degree of enhancement of biexciton to exciton quantum yield ($QY_{BX}/QY_X$) as a function of excitation wavelength, we calculated the center to the

side peak area ratio for 45 individual QDs collected on glass, and 38 QDs on Au NP substrates. **Figure 3.6** shows the box and whisker plots of the ratios at different excitation wavelengths. For the QDs on glass, the ratios show small dot-to-dot variation that is independent of excitation wavelength.

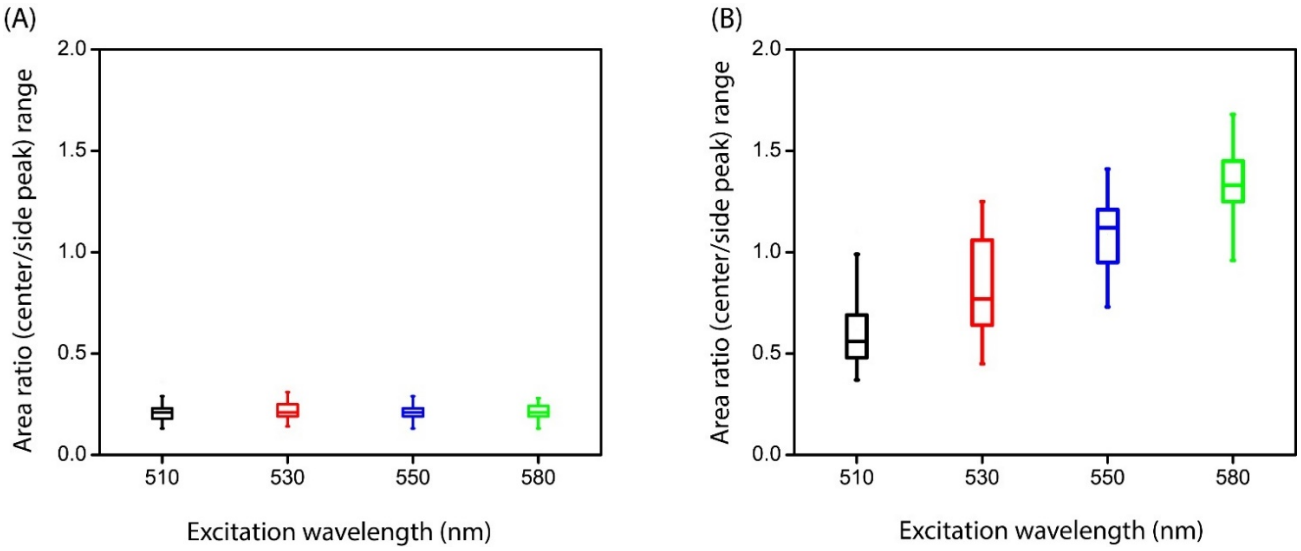


**Figure 3.6**. Box and whisker plots representing the measured $g^2(0)$ values (integrated area ratio of the center to side peaks obtained from $g^{(2)}(\tau)$ functions) of single QDs excited at 510 nm (black), 530 nm (red), 550 nm (blue) and 580 nm (green). The single QDs were deposited on (A) glass and on (B) Au NP substrates. The lines inside the box indicate the median values, the box edges indicate the first and third quartiles, and the top and bottom lines represent the maximum and minimum values.

The averaged ratio is 0.2, which is the biexciton QY of single QDs, according to previous literature. Whereas for the QDs on Au substrates, the ratio increases from an average of 0.62 (at

510 nm excitation) to an average of 1.33 (at 580 nm excitation). We also notice that the dot-to-dot variation in the ratios is much larger in the QDs on Au substrate than that of the QDs on glass. This is likely due to the variations in the positions of the QDs relative to Au NPs and variation in electric field experienced by the individual QDs. Since $QY_{BX}$ and $QY_X$ are dependent on the distance between the QD and the Au NPs as reported in our previous studies[12], the ratio will depend on the location of the QDs on the Au substrate. Nevertheless, the results show that by varying the excitation wavelength from "off" to "on" plasmon resonance, the statistical distribution of the spacing between consecutive photons emitted by a QD near Au NPs changes dramatically from sub-Poissonian to super-Poissonian distribution. For the same QD near a MNP, its multiexciton emission can be easily controlled by changing the excitation wavelength.

It is well known that the multiexciton emission intensity of QDs is dependent on laser excitation power.[33-42] Thus, in order to further understand the effect of plasmons on single and multiexciton emission, we measured the $g^{(2)}(\tau)$ functions of QDs at varying pump fluence at 580 nm excitation both on glass and on Au substrates. We are particularly interested in this wavelength because it is on the resonance with the LSPR and the effect on enhancement in multiexciton emission is even more pronounced than at any other wavelengths. The excitation powers used in our study were 50 nW, 250 nW, 500 nW, 1000 nW and 2500 nW. The estimated values of $\langle N \rangle$ for these powers are 0.02, 0.10, 0.21, 0.43 and 1.07, respectively. This relative change in $g^{(2)}(\tau)$ values collected from representative single QDs on both glass and on Au substrates as a function of excitation power are provided in **Figure 3.7A** and **Figure 3.7B** respectively.

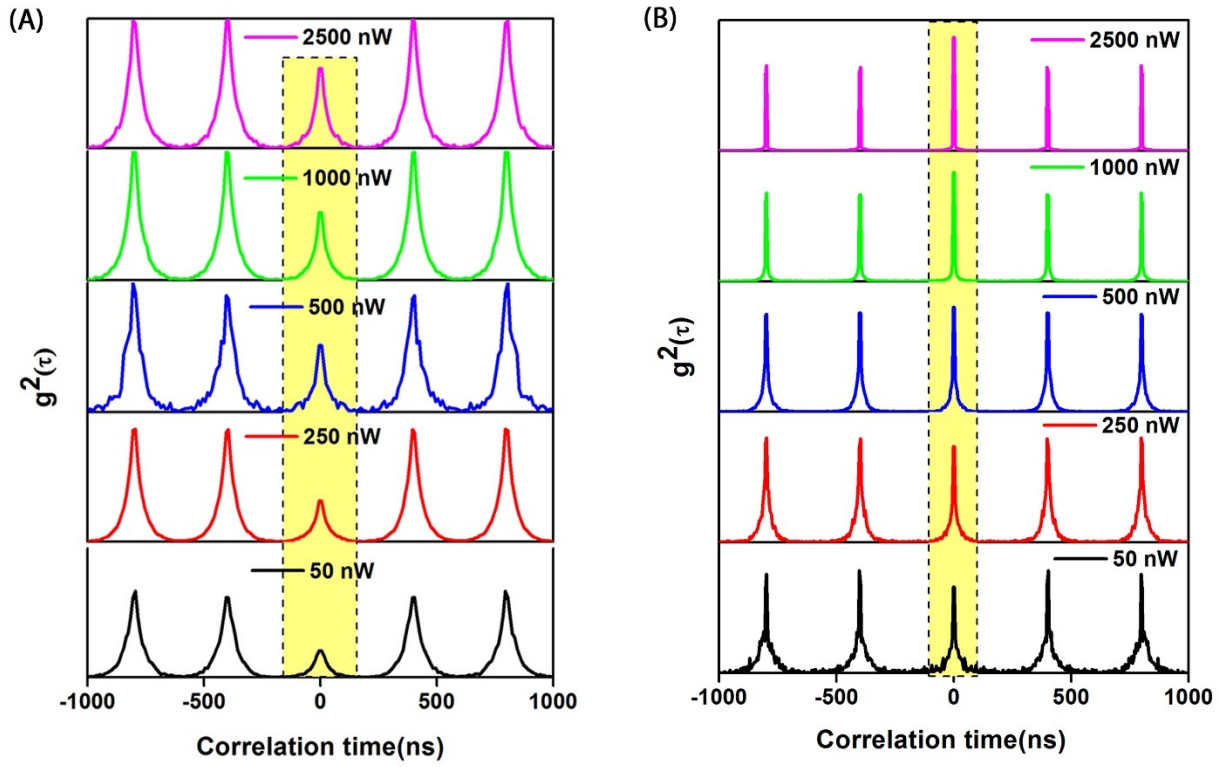


**Figure 3.7**. Representative photon correlation histograms at 580 nm excitation showing excitation pump fluence dependence of $g^2(0)$ functions for individual QD deposited on (A) glass and (B) Au NP substrates. The shaded portions in the histograms indicate the relative change in multiexciton emission behavior of individual QD under different excitation power as observed from the steep rise in center peak (at $\tau = 0$) when the excitation wavelength overlap/coincides with the LSPR of Au NPs ("on" resonance condition)

The area ratio of the center to the side peaks is plotted in **Figure 3.8**. The average value of the area ratio of the QDs on glass increases from 0.19 to 0.78 as a function of excitation power, due to the excitation of more biexcitons at higher power. Whereas for the QDs on Au substrate, the averaged ratio is 1.16 at 50 nW excitation. It increases gradually and levels off to 1.55 at 2500 nW excitation.

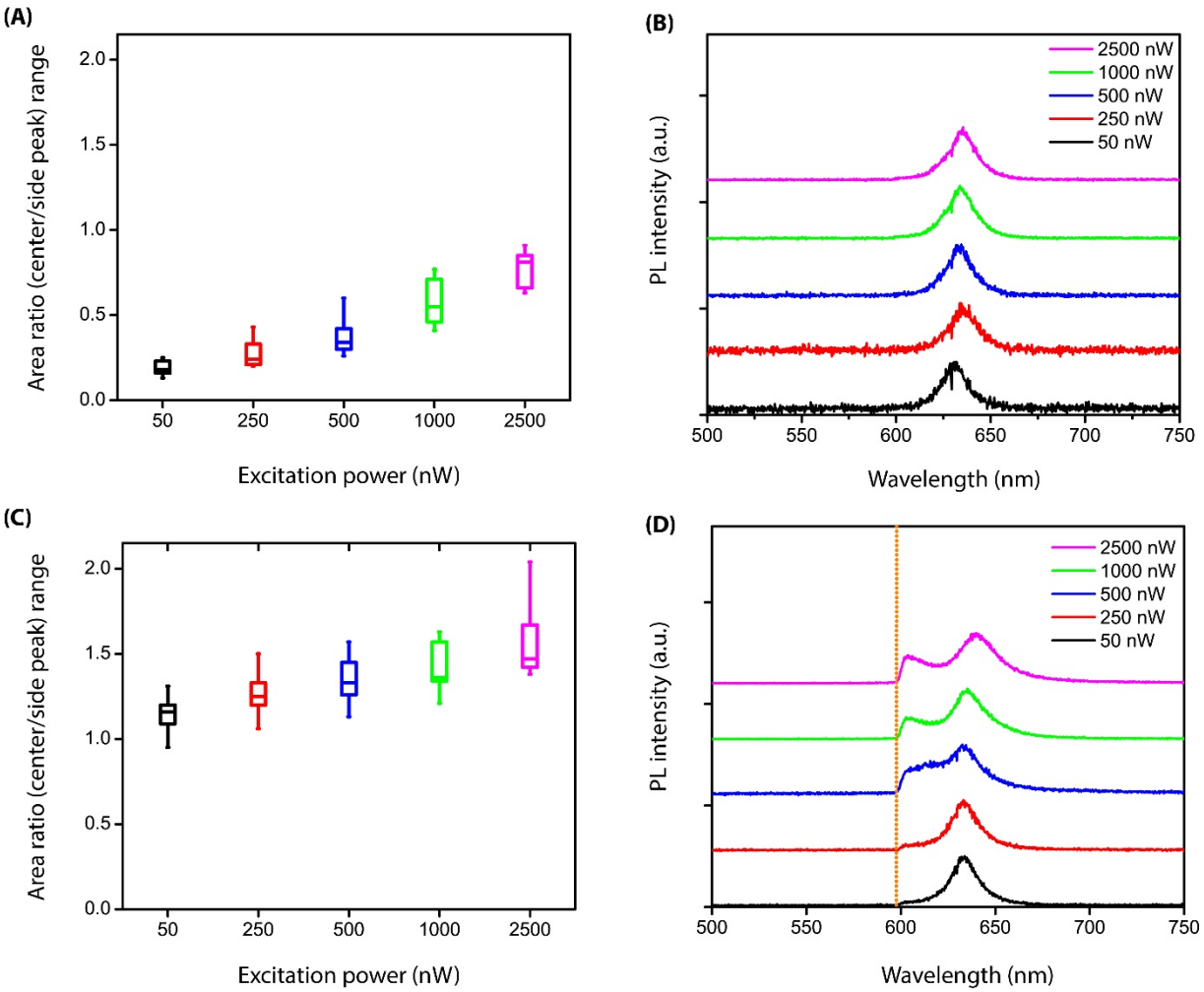


**Figure 3.8**. Box and whisker plots representing pump power dependence of g0 values plotted as a function of excitation power at 580 nm excitation for single QDs deposited on (A) glass and (C) Au NP substrate. (B) and (D) shows the representative photoluminescence spectra of a single QD on glass and on Au under 580 nm excitation at different excitation power (50 nW, 250 nW, 500 nW, 1000 nW and 2500 nW). The dotted line in figure (D) indicates the 600-long pass emission filter.

In addition to $g^{(2)}(\tau)$ measurements, pump-power dependent single QD PL spectra were simultaneously recorded. Along with increased BX emission when increasing excitation power,

there is a red-shift in the peak position of the PL spectra (**Figure 3.8B** and **Figure 3.9A, i, ii**) for the QDs on glass of ~20 meV.

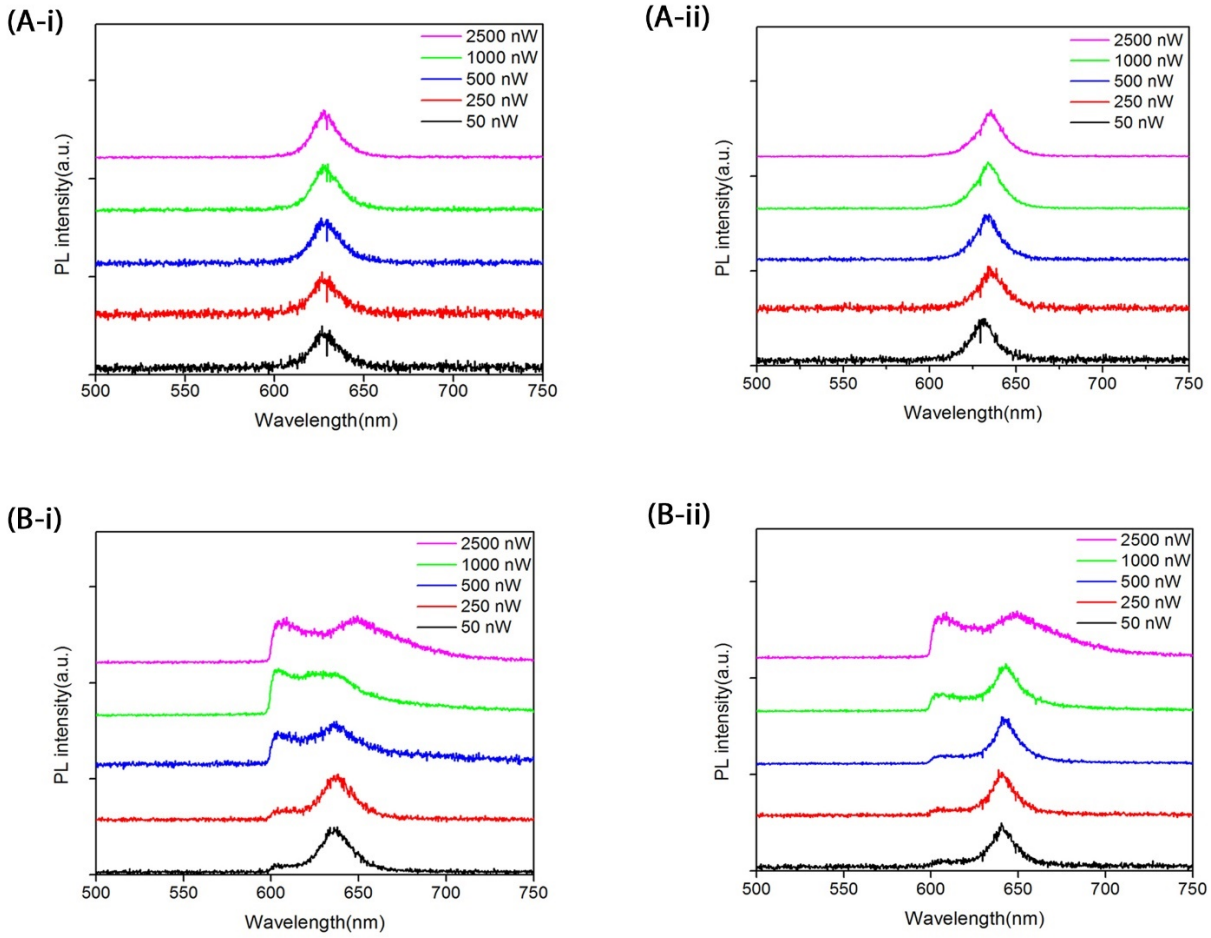


**Figure 3.9**. Representative single QD PL emission spectra plotted as a function of different excitation powers at (50nW,250nW,500nW,1000nW and 2500nW ) on (A) glass and (B) Au NP substrates respectively.

Biexciton(XX) in QDs is a quasiparticle consisting of a bound state 2e-2h pairs. As a result of spatial quantum confinement of multiple charge carriers, it results in a strong many-body mutual Coulombic interaction force. This interaction energy between the generated 2e-2h pair states can be expressed as biexciton binding energy, $E_{BE}^{XX} = 2E_X - E_{XX}$ (energy difference between two

independent excitons and a biexciton) where $E_X$= energy of X, $E_{XX}$= energy of biexciton. When BX state undergoes radiative relaxation, it decays down to an exciton and a photon. As a result of which, the photon or the energy that is being released is smaller than that of BX by an amount of the BX binding energy. Thus, the appearance of this BX emission peak in the photoluminescence spectrum is red-shifted (i.e. appears at the lower energy side) to that of the X emission peak. Theoretical model calculations revealed that biexciton binding energy($E_{BE}^{XX}$) is related to three-dimensional confinement dependent interplay between Coulombic interaction and correlation and exchange effects between the localized e-h pairs. In fact, the Coulombic interaction between the two pairs of localized excitons can be either positive(attraction) or negative(repulsion) resulting in a bound and unbound states of biexciton respectively. The binding state of BX results in red-shifted (at a lower energy than X), whereas an anti-binding (unbound) state of BX results in blue-shifted peak (at a higher energy than X). Of course, while deriving the binding energy values, it is necessary to consider the size of the nanocrystal. It has been observed earlier for ultra-small(sub-10nm) spherical CdSe QDs, the biexciton binding energy monotonically decreases as the overall size of the nanocrystal increases. Within a certain size regime, the $E_{BE}^{XX}$ follows 1/r dependence, but in the strong spatial confinement regime i.e. for ultra-small sizes of QD, it again results in e-e, h-h repulsion interaction. For CdSe QDs in the size range of 2.4-4 nm, these nanocrystals exhibited an overall increase in the binding energy values of triexcitons as compared to biexcitons. But it still followed a similar dependency with the size of the QD. However, apparently, the size of the QD is not the only deciding factor which determines the binding energy of excitons and multiexcitons. Critical consideration of electronic band structures which is also correlated to the wavefunction overlap of electron and hole states determine the magnitude of binding energy as well. Since binding energy is defined as the interaction strength between the e-h pairs, therefore it

is expected that delocalized carriers (unbound excitons) will possess lower binding energy relative to compact excitons. A previously reported theoretical study based on ab-initio and density functional theory calculations have discussed certain variation of exciton binding energy by separately considering the effects and contributions due to localization of excitons, valence and band-edge electrons and hole states. This red-shift observed in our study is due to the biexciton binding energy, as previously reported.[43-48] When the QDs were placed on Au substrates, an additional peak appeared at the blue (higher energy) side of the PL spectra along with the red shift of band-edge emission peak (see **Figure 3.8D** and **Figure 3.9B, i, ii**). Moreover, the intensity of the additional peak increases with increasing the excitation power. We were not able to measure the complete peak feature because a 600 nm long pass emission filter was used to block the excitation laser light at 580 nm. The additional peak feature at ~ 600 nm is ascribed to the emission from higher excitonic states, such as triexcitons of QDs. Triexciton emission was not observed in the QDs on glass because triexcitons could not be populated at the excitation power used in the experiment. But when QDs were close to Au NPs and excited at the LSPR, their absorption cross section was highly increased due to the plasmon resonance (see below for more discussion). This highly enhanced absorption makes it much easier to populate the higher order excitons in the QDs near Au NPs compared to the isolated ones. Therefore, triexciton emission was observed for the QDs on Au but not on glass at the same laser power.

From the experiments, we found that the multiexciton emission of QDs near Au NPs is highly dependent on the excitation wavelength. We hypothesize that this excitation dependence is mainly due to the difference in the QD absorption cross-section at different wavelength. This hypothesis is based on the well-established fact that the excitation of LSPR results in a highly enhanced electric field around the MNP, the magnitude of which is dependent on the excitation

wavelength.[49-53] To test our hypothesis, an electrodynamics simulation using discrete dipole approximation was performed to determine the change in the absorption cross-section of a single QD near Au NPs at different excitation wavelengths. In the simulation, an 8 nm QD was placed next to a 120 nm Au nanosphere, separated by a 20 nm layer of alumina (see **Figure 3.10A** for the scheme). The direction of the incident electric field was varied to be perpendicular or parallel to the axis defined by the center of the QD and the Au NP to account for the uncertainty in the direction of the electric field.

(A)

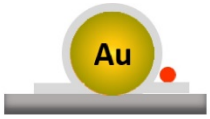


| Excitation wavelength (nm) | Averagea enhancement factor |
|---|---|
| 510 nm | 2.5 |
| 530 nm | 3.2 |
| 550 nm | 5.2 |
| 580 nm | 11.9 |

(B)

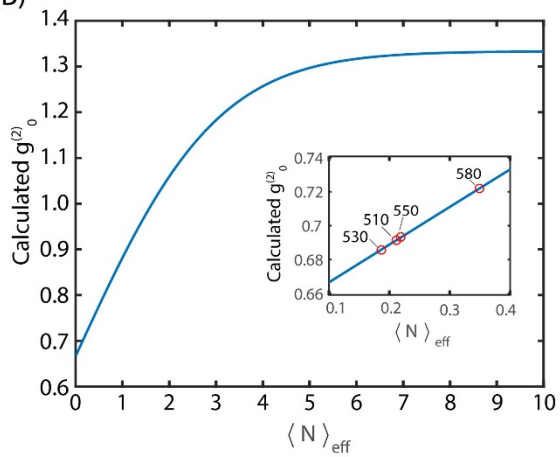


**Figure 3.10**. (A) The table indicates the calculated enhancement factor obtained at different excitation wavelengths for a single QD positioned on an Au NP substrate. The enhancement factor is averaged considering the variation in electric field direction. (B) Plot showing the calculated $g^2(0)$ values against the average number of photons absorbed per excitation pulse, <N> at 580nm excitation

The table in **Figure 3.10A** shows the average the electric field enhancement factor (EF). The enhancement factor EF is calculated using $EF=|E|^2/|E_{inc}|^2$, where $|E|^2$ is the magnitude of the

electric field the QD experiences, and $|E_{inc}|^2$ is the magnitude of the incident electric field. As a result of the electric field enhancement, the absorption cross-section of the QD near the Au NP is enlarged by EF times. The population of single and multiexcitons generated per pulse will change accordingly. Since the absorption of QDs follows Poisson distribution, the probability of generating k-th exciton is $P_{k-th\ exciton} = \frac{(EF\times\langle N\rangle)^k e^{-EF\times\langle N\rangle}}{k!}$

where $\langle N\rangle$ is the averaged photons absorbed per pulse, k=1 for single exciton, and k= 2 for biexciton and so on. Comparing the QDs on glass and on Au substrate, $P_{TX}$ is negligible for the QD on glass at low excitation power, but it is much higher for the QD on Au substrate. That is the reason why triexciton emission was observed in the QDs on the Au NPs substrate but not in the QDs on glass at the same laser power (**Figure 3.8, Figure 3.8B** and **Figure 3.8D**).

In addition to the absorption cross section, the exciton/multiexciton QYs of QDs are also modified when they are situated close to a MNP. Briefly, for an isolated QD, its emission QY can be expressed as $\eta = \frac{k_r}{k_r+k_{nr}}$

where $k_r$ and $k_{nr}$ represent the intrinsic radiative and non-radiative recombination rates of the QD. When the QD is placed near a MNP, its QY is modified and the new QY can be calculated with the following equation: $\eta' = \frac{k_r'}{k_r'+k_{nr}+k_{ET}}$

where $k_r'$ is the modified radiative rate and $k_{ET}$ is the additional non-radiative energy transfer rate from the QD to the MNP. Using these equations, exciton and biexciton QY of a QD close to Au NP (as illustrated in the scheme in **Figure 3.10A**) were calculated for the scenario when the electric field was perpendicular or parallel to the axis defined by the centers of the QD and the Au NP. The averaged $\eta_X'$ for single exciton is calculated to be 0.54 and the averaged $\eta_{BX}'$ for biexciton is 0.36. It is worth noting that $\eta_X'$ (=0.54) is lower than $\eta_X$(=0.95), meaning that the PL of excitons is

partially quenched when the QD was closed to the 120 nm Au NP. In contrast, $\eta'_{BX}$(=0.36) is higher than $\eta_{BX}$(=0.2), showing that the PL of biexcitons is enhanced in this case. This quenching/enhancing of exciton/biexciton emission in QDs near Au NPs has also been observed in our previous work.[12]

Using the modified QY and $\langle N\rangle_{eff}$where $\langle N\rangle_{eff}$=$\langle N\rangle\times EF$, the value of $g_0^{(2)}$ was calculated using $\mathrm{g}_0^{(2)} = \frac{2P_{N_{eff\geq 2}}}{(P_{N_{eff\geq 1}})^2}\frac{\eta'_{BX}}{\eta'_X}$ as a function of $\langle N\rangle_{eff}$ and the results are shown in **Figure 3.10B**. According to the calculation, $g_0^{(2)}$ increases with increasing $\langle N\rangle_{eff}$ and levels off, consistent with the experimental observations in Figure 4. In particular, when $\langle N\rangle_{eff}$ is greater than 1.6, $g_0^{(2)}$ value increases to above 1, indicating bunching of the emitted photons can be achieved under such conditions. To understand the excitation wavelength dependence of $g_0^{(2)}$, $\langle N\rangle_{eff}$ is calculated for 510, 530, 550 and 580 nm excitation at 50 nW power using $\langle N\rangle$ of the QD at these wavelengths and the EF listed in **Figure 3.10A**. In the inset of **Figure 3.10B**, $g_0^{(2)}$ of a QD near an Au NP for 510, 530, 550 and 580 nm excitation wavelength was labeled. Note that the $g_0^{(2)}$ values are lower than the experimental data (shown in **Figure 3.8**), and $g_0^{(2)}$ at 530 nm is lower than $g_0^{(2)}$ at 510 nm. This discrepancy is likely because we underestimate the EF. Since the Au NPs form aggregates on the substrate in **Figure 3.2B**, there is a good chance that the QDs will sit close to the Au NP aggregates, or at the junction between two Au NPs. The EF will be much higher than the single Au NP in that scenario. We would like to point out that this model completely neglects the contribution of the emission from higher order excitons, i. e. triexciton and above. It is acceptable to do so when the laser power is low and the EF is moderate. But at high laser power, there is substantial emission from triexcitons or even higher order excitons (e.g. **Figure 3.8D**). The emission from higher order excitons

should not be neglected in that case. Nevertheless, we show both experimentally and theoretically that $g_0^{(2)}$ of a QD near Au NPs is dependent on excitation wavelength and also excitation power.

## 3.5. Conclusion

In conclusion, the statistical distribution of photons emitted from single QDs can be manipulated by placing the QDs near plasmonic structures and varying excitation wavelength. This effect of exciton conditions was demonstrated in a simple hybrid system consisted of single CdSe/CdS QDs near Au NPs. Specifically, the photons emitted by a single QD switched from incomplete "anti-bunching" to "bunching" when the hybrid system was excited "on" plasmon resonance compared to "off" resonance. These results have indicated that higher order exciton emission can be significantly improved by suppressing the Auger recombination processes when the QDs are coupled to Au NPs and this enhancement of multiexciton emission can be judiciously manipulated by changing the excitation conditions. Both correlated experimental and theoretical studies are currently under progress to understand the optical response as a result of coherent interaction between single QDs and Au NPs and further explain the changes in lifetimes of QD on Au substrates as a function of excitation wavelength. These results suggest that excitation conditions should be considered when designing strongly coupled exciton-plasmon systems for optoelectronic devices or lasers.

## 3.6. References


1. Qian, L.; Zheng, Y.; Xue, J.; Holloway, P. H. Stable and efficient quantum-dot light-emitting diodes based on solution-processed multilayer structures. *Nat Photon* **2011,** *5* (9), 543-548.
2. Gao, X.; Cui, Y.; Levenson, R. M.; Chung, L. W. K.; Nie, S. In vivo cancer targeting and imaging with semiconductor quantum dots. *Nat Biotech* **2004,** *22* (8), 969-976.
3. Wang, X.; Ren, X.; Kahen, K.; Hahn, M. A.; Rajeswaran, M.; Maccagnano-Zacher, S.; Silcox, J.; Cragg, G. E.; Efros, A. L.; Krauss, T. D. Non-blinking semiconductor nanocrystals. *Nature* **2009,** *459* (7247), 686-689.
4. Chan, W. C. W.; Maxwell, D. J.; Gao, X.; Bailey, R. E.; Han, M.; Nie, S. Luminescent quantum dots for multiplexed biological detection and imaging. *Current Opinion in Biotechnology* **2002,** *13* (1), 40-46.
5. Michalet, X.; Pinaud, F. F.; Bentolila, L. A.; Tsay, J. M.; Doose, S.; Li, J. J.; Sundaresan, G.; Wu, A. M.; Gambhir, S. S.; Weiss, S. Quantum Dots for Live Cells, in Vivo Imaging, and Diagnostics. *Science* **2005,** *307* (5709), 538.
6. Sun, Q.; Wang, Y. A.; Li, L. S.; Wang, D.; Zhu, T.; Xu, J.; Yang, C.; Li, Y. Bright, multicoloured light-emitting diodes based on quantum dots. *Nat Photon* **2007,** *1* (12), 717-722.
7. Dai, X.; Zhang, Z.; Jin, Y.; Niu, Y.; Cao, H.; Liang, X.; Chen, L.; Wang, J.; Peng, X. Solution-processed, high-performance light-emitting diodes based on quantum dots. *Nature* **2014,** *515* (7525), 96-99.
8. García-Santamaría, F.; Chen, Y.; Vela, J.; Schaller, R. D.; Hollingsworth, J. A.; Klimov, V. I. Suppressed Auger Recombination in "Giant" Nanocrystals Boosts Optical Gain Performance. *Nano Letters* **2009,** *9* (10), 3482-3488.
9. Efros, A. L.; Nesbitt, D. J. Origin and control of blinking in quantum dots. *Nat Nano* **2016,** *11* (8), 661-671.
10. Galland, C.; Ghosh, Y.; Steinbrück, A.; Hollingsworth, J. A.; Htoon, H.; Klimov, V. I. Lifetime blinking in nonblinking nanocrystal quantum dots. *Nature Communications* **2012,** *3*, 908.
11. LeBlanc, S. J.; McClanahan, M. R.; Jones, M.; Moyer, P. J. Enhancement of Multiphoton Emission from Single CdSe Quantum Dots Coupled to Gold Films. *Nano Letters* **2013,** *13* (4), 1662-1669.
12. Dey, S.; Zhou, Y.; Tian, X.; Jenkins, J. A.; Chen, O.; Zou, S.; Zhao, J. An experimental and theoretical mechanistic study of biexciton quantum yield enhancement in single quantum dots near gold nanoparticles. *Nanoscale* **2015,** *7* (15), 6851-6858.
13. Park, Y.-S.; Ghosh, Y.; Chen, Y.; Piryatinski, A.; Xu, P.; Mack, N. H.; Wang, H.-L.; Klimov, V. I.; Hollingsworth, J. A.; Htoon, H. Super-Poissonian Statistics of Photon Emission from Single CdSe-CdS Core-Shell Nanocrystals Coupled to Metal Nanostructures. *Physical Review Letters* **2013,** *110* (11), 117401.
14. Masuo, S.; Kanetaka, K.; Sato, R.; Teranishi, T. Direct Observation of Multiphoton Emission Enhancement from a Single Quantum Dot Using AFM Manipulation of a Cubic Gold Nanoparticle. *ACS Photonics* **2016,** *3* (1), 109-116.
15. Wang, F.; Karan, N. S.; Minh Nguyen, H.; Ghosh, Y.; Hollingsworth, J. A.; Htoon, H. Coupling Single Giant Nanocrystal Quantum Dots to the Fundamental Mode of Patch Nanoantennas through Fringe Field. *Scientific Reports* **2015,** *5*, 14313.
16. Canneson, D.; Mallek-Zouari, I.; Buil, S.; Quélin, X.; Javaux, C.; Mahler, B.; Dubertret, B.; Hermier, J. P. Strong Purcell effect observed in single thick-shell CdSe/CdS nanocrystals coupled to localized surface plasmons. *Physical Review B* **2011,** *84* (24), 245423.

17. Naiki, H.; Masuhara, A.; Masuo, S.; Onodera, T.; Kasai, H.; Oikawa, H. Highly Controlled Plasmonic Emission Enhancement from Metal-Semiconductor Quantum Dot Complex Nanostructures. *The Journal of Physical Chemistry C* **2013,** *117* (6), 2455-2459.
18. Naiki, H.; Masuo, S.; Machida, S.; Itaya, A. Single-Photon Emission Behavior of Isolated CdSe/ZnS Quantum Dots Interacting with the Localized Surface Plasmon Resonance of Silver Nanoparticles. *The Journal of Physical Chemistry C* **2011,** *115* (47), 23299-23304.
19. Naiki, H.; Uedao, T.; Wang, L.; Tamai, N.; Masuo, S. Multiphoton Emission Enhancement from a Single Colloidal Quantum Dot Using SiO2-Coated Silver Nanoparticles. *ACS Omega* **2017,** *2* (2), 728-737.
20. Matsuzaki, K.; Vassant, S.; Liu, H.-W.; Dutschke, A.; Hoffmann, B.; Chen, X.; Christiansen, S.; Buck, M. R.; Hollingsworth, J. A.; Götzinger, S.; Sandoghdar, V. Strong plasmonic enhancement of biexciton emission: controlled coupling of a single quantum dot to a gold nanocone antenna. *Scientific Reports* **2017,** *7*, 42307.
21. Mandel, L. Sub-Poissonian photon statistics in resonance fluorescence. *Opt. Lett.* **1979,** *4* (7), 205-207.
22. Zou, X. T.; Mandel, L. Photon-antibunching and sub-Poissonian photon statistics. *Physical Review A* **1990,** *41* (1), 475-476.
23. Kimble, H. J.; Dagenais, M.; Mandel, L. Photon Antibunching in Resonance Fluorescence. *Physical Review Letters* **1977,** *39* (11), 691-695.
24. Matthiesen, C.; Stanley, M. J.; Hugues, M.; Clarke, E.; Atatüre, M. Full counting statistics of quantum dot resonance fluorescence. *Scientific Reports* **2014,** *4*, 4911.
25. Sonia, B.; Kelley, R.; Jelena, V. Engineered quantum dot single-photon sources. *Reports on Progress in Physics* **2012,** *75* (12), 126503.
26. Nair, G.; Zhao, J.; Bawendi, M. G. Biexciton Quantum Yield of Single Semiconductor Nanocrystals from Photon Statistics. *Nano Letters* **2011,** *11* (3), 1136-1140.
27. Park, Y.-S.; Ghosh, Y.; Xu, P.; Mack, N. H.; Wang, H.-L.; Hollingsworth, J. A.; Htoon, H. Single-Nanocrystal Photoluminescence Spectroscopy Studies of Plasmon–Multiexciton Interactions at Low Temperature. *The Journal of Physical Chemistry Letters* **2013,** *4* (9), 1465-1470.
28. Hoang, T. B.; Akselrod, G. M.; Mikkelsen, M. H. Ultrafast Room-Temperature Single Photon Emission from Quantum Dots Coupled to Plasmonic Nanocavities. *Nano Letters* **2016,** *16* (1), 270-275.
29. Sadahiro Masuo, H. N., Shinjiro Machida,Akira Itaya. Photon statistics in enhanced fluorescence from a single CdSe/ZnS quantum dot in the vicinity of silver nanoparticles. *Applied Physics Letters* **2009,** *95* (19), 193106.
30. Kimling, J.; Maier, M.; Okenve, B.; Kotaidis, V.; Ballot, H.; Plech, A. Turkevich Method for Gold Nanoparticle Synthesis Revisited. *The Journal of Physical Chemistry B* **2006,** *110* (32), 15700-15707.
31. Bastús, N. G.; Comenge, J.; Puntes, V. Kinetically Controlled Seeded Growth Synthesis of Citrate-Stabilized Gold Nanoparticles of up to 200 nm: Size Focusing versus Ostwald Ripening. *Langmuir* **2011,** *27* (17), 11098-11105.
32. Chen, O.; Zhao, J.; Chauhan, V. P.; Cui, J.; Wong, C.; Harris, D. K.; Wei, H.; Han, H.-S.; Fukumura, D.; Jain, R. K.; Bawendi, M. G. Compact high-quality CdSe–CdS core–shell nanocrystals with narrow emission linewidths and suppressed blinking. *Nat Mater* **2013,** *12* (5), 445-451.

33. Htoon, H.; Malko, A. V.; Bussian, D.; Vela, J.; Chen, Y.; Hollingsworth, J. A.; Klimov, V. I. Highly Emissive Multiexcitons in Steady-State Photoluminescence of Individual "Giant" CdSe/CdS Core/Shell Nanocrystals. *Nano Letters* **2010,** *10* (7), 2401-2407.
34. Vanmaekelbergh, D.; van Vugt, L. K.; Bakker, H. E.; Rabouw, F. T.; Nijs, B. d.; van Dijk-Moes, R. J. A.; van Huis, M. A.; Baesjou, P. J.; van Blaaderen, A. Shape-Dependent Multiexciton Emission and Whispering Gallery Modes in Supraparticles of CdSe/Multishell Quantum Dots. *ACS Nano* **2015,** *9* (4), 3942-3950.
35. Santori, C.; Solomon, G. S.; Pelton, M.; Yamamoto, Y. Time-resolved spectroscopy of multiexcitonic decay in an InAs quantum dot. *Physical Review B* **2002,** *65* (7), 073310.
36. J. Canet-Ferrer, G. M.-M., J. Herranz, D. Rivas, B. Alen, Y. Gonzalez, D. Fuster, L. Gonzalez,J. Martínez-Pastor. Exciton and multiexciton optical properties of single InAs/GaAs site-controlled quantum dots. *Applied Physics Letters* **2013,** *103* (18), 183112.
37. Dekel, E.; Gershoni, D.; Ehrenfreund, E.; Spektor, D.; Garcia, J. M.; Petroff, P. M. Multiexciton Spectroscopy of a Single Self-Assembled Quantum Dot. *Physical Review Letters* **1998,** *80* (22), 4991-4994.
38. Bonati, C.; Mohamed, M. B.; Tonti, D.; Zgrablic, G.; Haacke, S.; van Mourik, F.; Chergui, M. Spectral and dynamical characterization of multiexcitons in colloidal CdSe semiconductor quantum dots. *Physical Review B* **2005,** *71* (20), 205317.
39. Dekel, E.; Regelman, D. V.; Gershoni, D.; Ehrenfreund, E.; Schoenfeld, W. V.; Petroff, P. M. Cascade evolution and radiative recombination of quantum dot multiexcitons studied by time-resolved spectroscopy. *Physical Review B* **2000,** *62* (16), 11038-11045.
40. D. Hessman, P. C., M.- E. Pistol, C. Pryor, L. Samuelson. Excited states of individual quantum dots studied by photoluminescence spectroscopy. *Applied Physics Letters* **1996,** *69* (6), 749-751.
41. Park, Y. S.; Malko, A. V.; Vela, J.; Chen, Y.; Ghosh, Y.; García-Santamaría, F.; Hollingsworth, J. A.; Klimov, V. I.; Htoon, H. Near-Unity Quantum Yields of Biexciton Emission from $\mathrm{CdSe}/\mathrm{CdS}$ Nanocrystals Measured Using Single-Particle Spectroscopy. *Physical Review Letters* **2011,** *106* (18), 187401.
42. Ji, M.; Park, S.; Connor, S. T.; Mokari, T.; Cui, Y.; Gaffney, K. J. Efficient Multiple Exciton Generation Observed in Colloidal PbSe Quantum Dots with Temporally and Spectrally Resolved Intraband Excitation. *Nano Letters* **2009,** *9* (3), 1217-1222.
43. Klimov, V.; Hunsche, S.; Kurz, H. Biexciton effects in femtosecond nonlinear transmission of semiconductor quantum dots. *Physical Review B* **1994,** *50* (11), 8110-8113.
44. Choi, Y.; Lim, S.; Lee, Y. H.; Choi, H. In *Ultrafast red-shift of biexciton binding energy by multiple exciton generation in PbS quantum dots*, CLEO: 2013, 9-14 June 2013; 2013; pp 1-2.
45. Achermann, M.; Hollingsworth, J. A.; Klimov, V. I. Multiexcitons confined within a subexcitonic volume: Spectroscopic and dynamical signatures of neutral and charged biexcitons in ultrasmall semiconductor nanocrystals. *Physical Review B* **2003,** *68* (24), 245302.
46. Caruge, J. M.; Chan, Y.; Sundar, V.; Eisler, H. J.; Bawendi, M. G. Transient photoluminescence and simultaneous amplified spontaneous emission from multiexciton states in $\mathrm{CdSe}$ quantum dots. *Physical Review B* **2004,** *70* (8), 085316.
47. Fisher, B.; Caruge, J.-M.; Chan, Y.-T.; Halpert, J.; Bawendi, M. G. Multiexciton fluorescence from semiconductor nanocrystals. *Chemical Physics* **2005,** *318* (1–2), 71-81.
48. Fisher, B.; Caruge, J. M.; Zehnder, D.; Bawendi, M. Room-Temperature Ordered Photon Emission from Multiexciton States in Single CdSe Core-Shell Nanocrystals. *Physical Review Letters* **2005,** *94* (8), 087403.

49. Tanabe, K. Field Enhancement around Metal Nanoparticles and Nanoshells: A Systematic Investigation. *The Journal of Physical Chemistry C* **2008,** *112* (40), 15721-15728.
50. Agrawal, A.; Kriegel, I.; Milliron, D. J. Shape-Dependent Field Enhancement and Plasmon Resonance of Oxide Nanocrystals. *The Journal of Physical Chemistry C* **2015,** *119* (11), 6227-6238.
51. Huang, Y.; Ma, L.; Hou, M.; Li, J.; Xie, Z.; Zhang, Z. Hybridized plasmon modes and near-field enhancement of metallic nanoparticle-dimer on a mirror. *Scientific Reports* **2016,** *6*, 30011.
52. Encai Hao, G. C. S. Electromagnetic fields around silver nanoparticles and dimers. *The Journal of Chemical Physics* **2003,** *120* (1), 357-366.
53. Hille, A.; Moeferdt, M.; Wolff, C.; Matyssek, C.; Rodríguez-Oliveros, R.; Prohm, C.; Niegemann, J.; Grafström, S.; Eng, L. M.; Busch, K. Second Harmonic Generation from Metal Nano-Particle Resonators: Numerical Analysis On the Basis of the Hydrodynamic Drude Model. *The Journal of Physical Chemistry C* **2016,** *120* (2), 1163-1169.

# Chapter Four .

# Effect of Gradient Alloying on Photoluminescence Blinking of Single $CdS_xSe_{1-x}$ Nanocrystals

*"Reprinted and modified with permission from: S. Dey, S. Chen, S. Thota, Md. R. Shakil, S. L. Suib J. Zhao; J. Phys. Chem. C, 2016, 120 (37), 20547-20554. Copyright [2016] American Chemical Society."*

## 4.1. Abstract

Alloyed $CdS_xSe_{1-x}$ semiconductor nanocrystals (NCs) were obtained from a one-pot synthesis at reduced temperature with moderate quantum yield. Comprehensive structural characterizations of the CdSSe NCs reveal that the NCs have gradient alloyed structure, with Cd evenly distributed over the entire NC, Se rich in the center, and S rich on the outer region. This is due to the difference in the nucleation kinetics of S and Se precursors. Optical studies at the single NC level show that the NCs have reduced photoluminescence blinking, increased "on" time fraction, and good photo stability, in comparison with CdSe NCs. The incorporation of sulfur composition in the alloy NCs improves surface passivation, and in turn protects the NCs from (photo) oxidation. And the gradual change in the NC composition from center to outer regions creates a smooth "interface", compared to core/shell NCs. These factors lead to reduced non-radiative rates in the NCs, improving their emitting properties.

## 4.2. Introduction

Semiconductor nanocrystals (NCs) exhibit unique size-dependent tunability of their optoelectronic properties due to quantum confinement, making them promising materials in a wide range of applications, such as photovoltaics, catalysis, optoelectronics and biomedicine.[1-6] Popular ways of tailoring the band gap of the NCs are by tuning of the size of the NCs or by growing a semiconductor shell around the NC cores. The growth of a shell is favorable because the band-gap of the core/shell NCs can be conveniently controlled by the shell thickness.[7-17] In addition, the shell provides better surface passivation of the NC core, improving the photoluminescence quantum yield and photostability of the NCs.[14-15] With the development of synthetic techniques, core/shell CdSe/CdS NCs with an extremely high quantum yield (> 90%) and size uniformity have been achieved.[18-20] However, core/shell synthesis often involves multiple steps and the growth of a shell increases the overall size of the NC, which is not desired for many biological applications.[21-24] To address this issue, an effective strategy of engineering the band gap was developed by mixing two or more binary semiconductors to fabricate alloyed ternary ($AB_xC_{1-x}$) or quaternary ($A_xB_{1-x}C_yD_{1-y}$) semiconductor nanostructures.[22, 25] Band gap in these alloyed NCs can be controlled not only by their size, but also by their composition. Therefore, it is possible to tune the emission of alloyed NCs across a wide range while maintaining a small size. In addition, studies show that the formation of alloyed interface in core/shell NCs strongly affects the physical processes in the NCs, leading to reduced non-radiative Auger recombination, improving the emitting property of the NCs.[26-32]

Several previous reports have demonstrated one-pot synthesis of colloidal II-VI alloyed NCs with low to moderate quantum yield.[21-23, 33-42] On the basis of variation in their internal structure and charge carrier confinement potential, these alloyed systems can often be classified

either as homogeneous or gradient structure.[25] The gradient structure is interesting because the gradual smoothening of confinement potential may inhibit blinking (fluorescence intermittency) of the single NCs. Such effect has been observed in II-VI and IV-VI core/shell NCs with an interfacial alloying layer, where decreased Auger rate, suppressed blinking and increased multiexciton emission were found.[43-49] Recently, Keene et al. have discovered that in graded alloy $CdS_xSe_{1-x}$ NCs, the excited hole is decoupled from the surface traps.[50] By increasing the sulfur content in the $CdS_xSe_{1-x}$ NCs, the hole trapping process can be significantly reduced or even completely eliminated. The elimination of non-radiative hole-trapping greatly increases the quantum yield, and can potentially reduce the blinking phenomenon in these compact size NCs. The work shows that the alloyed NCs are a promising new class of fluorophores with high quantum yield and steady fluorescence intensity. However, single particle level studies of these alloyed $CdS_xSe_{1-x}$ NCs are still needed to understand the effect of gradient alloy formation on the optical properties of the NCs.

In the present work, we report detailed structural and optical characterization of ternary alloyed $CdS_xSe_{1-x}$ NCs prepared via single step synthetic method at reduced temperature derived from air stable precursors of cadmium acetate dihydrate, selenium and sulfur. The CdSSe NCs exhibited high crystallinity with a narrow size distribution from transmission electron microscopy (TEM) study. The formation of the alloyed nanostructures was confirmed using X-ray Photoelectron spectroscopy (XPS) and powder X-ray Diffraction (XRD) techniques and a detailed analysis of the internal structures were performed using High Angular Annular Dark Field-Scanning TEM (HAADF-STEM) measurements. The PL spectra of the NCs showed a single, narrow peak with the highest quantum yield (QY) of ~45%. Confocal fluorescence measurements were carried out to further investigate the effect of gradient alloy formation on the blinking

behavior and photostability of single CdSSe NCs, compared with the regular binary CdSe NCs. The blinking statistics and fluorescence "on" time fraction of the CdSSe and CdSe NCs were analyzed and compared. From the single particle optical measurements, with just a little incorporation of S into the structure, a significant improvement of the photostability and reduced blinking was observed. This improvement in the optical properties can be attributed to the formation of a pseudo core-shell like structure with a selenium enriched core and a sulfur-rich passivating layer on the cores.

## 4.3. Experimental Methods

### *4.3.1 Chemicals*

Cadmium acetate dihydrate (Cd(OAc)2.2H2O, ≥98.0%), cadmium oxide (>99.99%) elemental selenium (powder, ~ 100mesh, ≥99.5%), elemental sulfur (powder, ~325 mesh, 99.5%), octadecylamine (ODA, technical grade, 90%) 1-octadecene (ODE, technical grade, 90%), oleic acid (~90%) and oleylamine (70%) were purchased from Sigma Aldrich. Trioctylphosphine (TOP, technical grade, 90%) was purchased from Acros-Organics. Trioctylphosphine oxide (~99%) was purchased from Fisher Scientific. All of the chemicals were used as received without any further purification.

### *4.3.2 $CdS_xSe_{1-x}$ Nanocrystal Synthesis*

CdSxSe1-x ternary nanocrystals (NCs) were synthesized using a simple single step hot injection method. A typical synthesis involves a single injection of a premixed TOP-Se/TOP-S precursor solution into a three-neck round bottom flask containing cadmium precursor in TOP

solvent. To prepare the mixture of TOP-S and TOP-Se, 8 mg of elemental Se and 20 mg of elemental S powder were mixed with 1 mL of fresh TOP under vigorous stirring. The mixture was sonicated until it formed a clear homogeneous solution. Nitrogen gas was purged into the S/Se-TOP solution until it was transferred in a syringe for further injection into the reaction flask.

In a typical one-pot synthesis, 40 mg of the cadmium acetate dihydrate, 0.5g of ODA and 2.5 mL of TOP were loaded into a 25 mL three-neck flask. The reaction mixture was then heated to about 100 ºC for around 15 min under vacuum in order to get rid of any moisture or oxygen present in the reaction flask. Once the solution turned colorless, indicating most of the cadmium precursors and the alkyl amine were dissolved in TOP, the reaction mixture was further heated to 240 ºC at a rate of 10 ºC/min with constant stirring under nitrogen atmosphere. Once the reaction temperature reached 240 ºC, the premixed solution of TOP-Se/TOP-S was swiftly injected into the flask and the growth time was counted since then.

In order to monitor the growth of the NCs, reaction aliquots of small volume (~0.2 mL) were taken out quickly from the reaction flask at different growth times (30 sec, 1 min, 5 min, 10 min, 15 min and 25 min) and dispersed in 2mL of hexane. After 25 min of reaction, the heating mantle was removed and the reaction was allowed to cool down to room temperature under nitrogen. The synthesized NCs were further isolated, precipitated and washed a few times with a mixture of ethanol and hexane. The NC precipitate was re-suspended in a small amount of hexane and stored at room temperature for further characterization. All the NC solutions were cooled to room temperature before collecting the optical spectra.

### *4.3.3 Synthesis of CdSe nanocrystals*

CdSe nanocrystals were synthesized following a method reported by Peng et al[51] with a minor modification. In a typical synthesis, 0.2 mmol of $Cd(OA)_2$, 250 mg of TOPO, 1.0 mL of

oleylamine, and 4.0 mL of ODE were loaded into a three-neck flask. After the flask was washed for 10 min by nitrogen, the mixed solution was heated to 210 ºC at a rate of 20 ºC/min. Selenium solution (16 mg of selenium dissolved in the mixed solution of 0.3 mL of TOP and 0.7 mL of ODE) was injected into the flask and reacted for 2 minutes at 210 ºC. After removing the heating mantle, 8.0 mL of ethanol was quickly injected into the flask, and the reaction solution was centrifuged at 5000 rpm for 5 min. After removing the supernatant, CdSe nanocrystals were redispersed in 5.0 mL of ethanol, followed by centrifugation at 5000 rpm for 5 min. The products were dispersed in hexane for further characterization.

### *4.3.4 Characterization*

The UV-visible absorption and photoluminescence (PL) spectra of the NCs in solution were recorded using a Cary-60 (Agilent Technologies) UV-vis spectrophotometer and a Cary Eclipse (Agilent) spectrofluorometer, respectively. Structural and compositional characterization of the NCs was performed using transmission electron microscopy, powder x-ray diffraction and X-ray photoelectron spectroscopy. The shape and size distribution of the NCs was studied by using a JEOL 2010 transmission electron microscope operated at 200 kV. The elemental distribution of Cd, Se and S in the NCs were analyzed using a FEI-TALOS high resolution TEM measured in a high angle annular dark field (HAADF)-scanning transmission electron microscopy (STEM) mode. Composition of the NCs was determined by XPS. The XPS measurements were carried out using a PHI model 590 Multi-probes system with a monochromatic Al $K_\alpha$ radiation ($\lambda$ =1486.6 eV) as X-ray source. The pressure in the analysis chamber was 2.0 × 10−8 Torr during the data collection and the survey scans were performed at a pass energy of 100 eV. The spectra obtained were analyzed and fitted using Casa XPS software (version 2.3.12). All the spectra were calibrated to the C 1s transition set at 284.6 eV. Powder XRD patterns of the NCs were recorded between 20°

to 60° in 2θ mode at room temperature using a Rigaku ultima IV power X-ray Diffractometer with Cu Kα radiation operated at a tube voltage of 40 kV and current of 44 mA with a scanning rate of 0.5°/min.

Room temperature PL quantum yields of the NCs were calculated by comparing to Rhodamine 6G dye dissolved in ethanol (QY = 0.95). The PL intensity time trajectories of single CdSSe and CdSe NCs emitting at similar spectral region were acquired using a home-built confocal microscope. To prepare the sample for single NC measurements, the NC solution was highly diluted and spun casted onto a clean glass coverslip. The density of the NCs on glass is low enough to allow one NC to be studied at a time. All the single NC measurements were carried out at room temperature. The single NCs were excited at 532 nm (SOLEA Supercontinuum laser, Picoquant) with an excitation power of 40 nW, and repetition rate of 2.5 MHz. The emission was collected using a τ-SPAD (Picoquant) with proper spectral filter.

## 4.4. Results and Discussion

The growth of $CdS_xSe_{1-x}$ NCs was monitored by UV-Vis and PL spectroscopy of reaction aliquots taken at different reaction times. **Figure 4.1A** shows the UV-Vis absorption spectra of the CdSSe nanocrystals dissolved in hexane at growth time between 30 sec to 25 min. The absorption spectra of all the samples show several distinct excitonic features. As an immediate effect of quantum confinement, we also observe a continuous red shift in the first excitonic absorption peak as the NCs grow in size. The corresponding PL spectra of the NC samples are shown in **Figure 4.1B**.

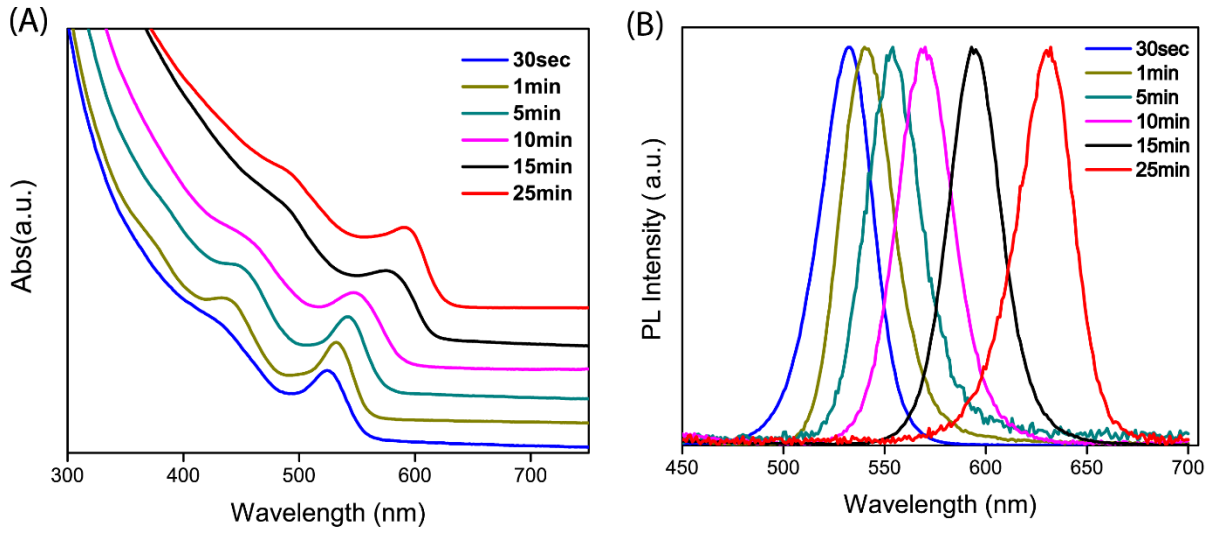


**Figure 4.1**. (A) Absorption spectra of alloyed CdSSe NCs at different growth times. (B) Corresponding photoluminescence(PL) spectra of the same samples dispersed in hexane.

The emission peaks lie in the range between 535-630 nm with PL FWHM (full width half maximum) between 27-32 nm. With an increase in size of the NCs, the PL spectra of the samples show a sequential red shift. Notice that in some of the earlier studies, the PL spectra of the alloyed CdSSe NCs had a high-energy peak from band edge emission and a broad low energy emission peak from the surface trap state emission. [23, 52-53] In contrast, the PL spectra of our samples exhibit only a single, narrow emission peak, indicating better surface passivation of the CdSSe NCs synthesized in this work.

A comprehensive structural characterization of these NCs was performed using high resolution transmission electron microscopy as shown in **Figure 4.2**. From **Figure 4.2A**, the NCs have a mean diameter of 6.5±0.75 nm, which indicates a narrow size distribution. The inset in **Figure 4.2A** shows high crystalline nature of the NCs with clear lattice fringes from a single NC.

**Figure 4.2B** shows the HAADF-STEM image of the alloyed CdSSe NCs, and **Figure 4.2C** represents the STEM image superimposed with the energy dispersive spectroscopy (EDS) mapping images of cadmium (**Figure 4.2D**), selenium (**Figure 4.2E**) and sulfur (**Figure 4.2F**).

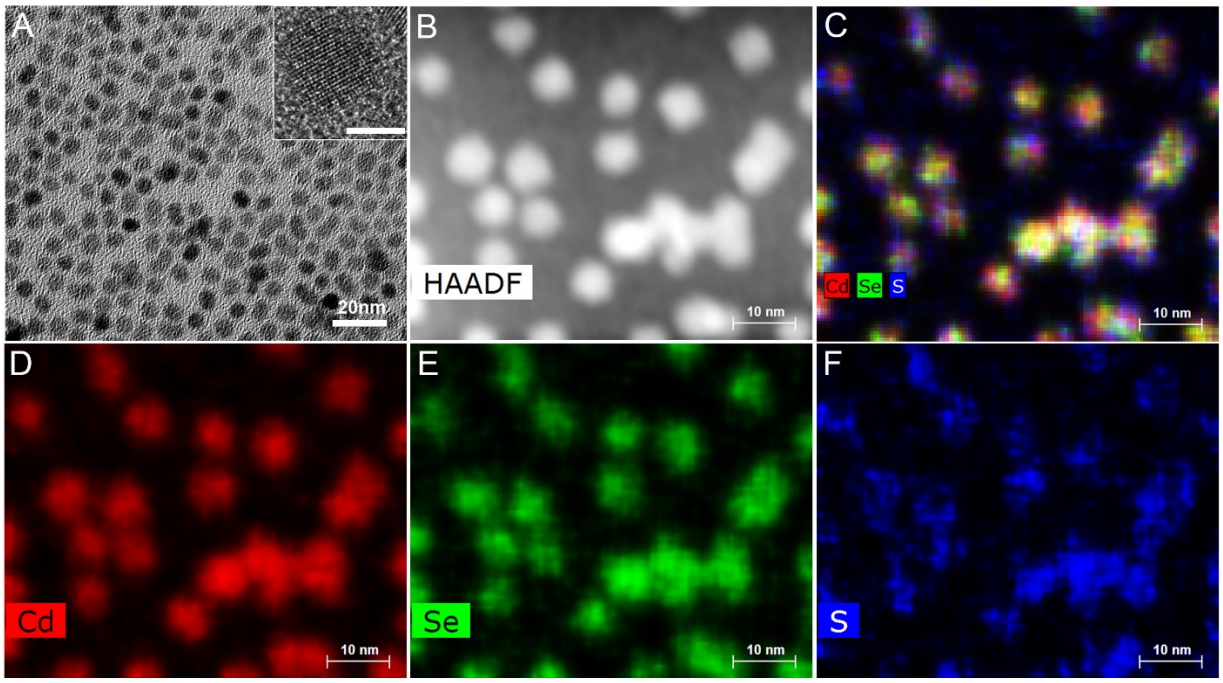


**Figure 4.2**. (A) TEM image of CdSSe NCs, and inset, HR TEM image (scale bar=5nm) showing high crystallinity of the NC. (B) High-angular annular dark field (HAADF) scanning transmission electron microscopy (STEM) image of the NCs. (C) Overlaid STEM image of CdSSe NCs with individual EDS mapping images of (D) cadmium, (E) selenium and (F) sulfur. The images show the elemental distribution of individual elements in the alloyed CdSSe NCs.

From the EDS mapping images and representative line scans of individual particles as shown in **Figure 4.3**, it is clear that the Cd is evenly distributed throughout the entire NCs whereas Se is enriched in center and S is randomly distributed but deficient in the center.

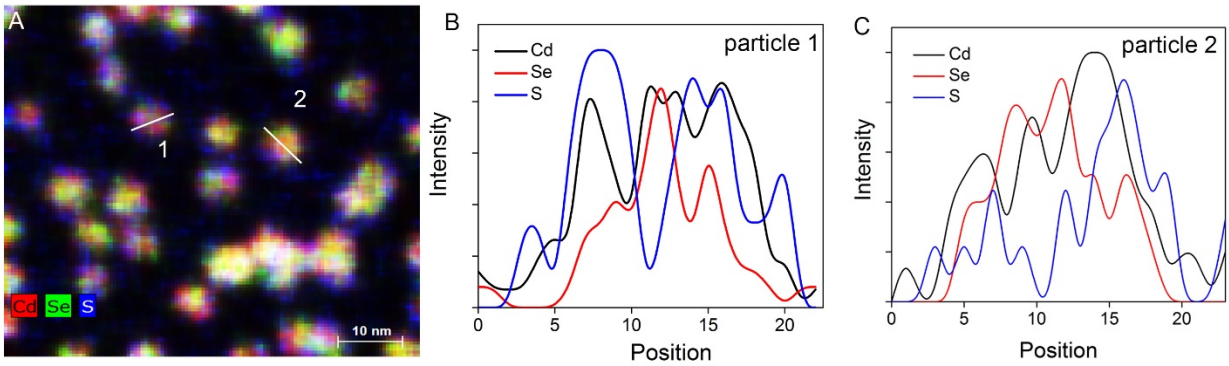


**Figure 4.3**. (A) Overlay of STEM and EDS images of CdSSe NCs. (B, C) Line scans of two NCs (labeled particle 1 and 2) showing the distribution of cadmium, selenium, and sulfur within the NCs.

The formation process of core-shell like alloyed NCs can be explained by studying the variation in the elemental composition of these NCs during reaction using XPS. XPS survey spectrum of the samples at different growth times (1 min, 5 min, 10 min, 15 min and 25min) were scanned in the range 0-600 eV. **Figure 4.4** shows a typical XPS survey spectrum of the CdSSe NCs. The characteristic peaks of Cd $3d_{5/2}$ (~ 405 eV), S 2p (~159 eV) and Se 3d (~ 52 eV) confirmed the existence of three elements in CdSSe NCs. The amount of Cd and Se are calculated from Cd 3d and Se 3d signals respectively and S is from S 2p.

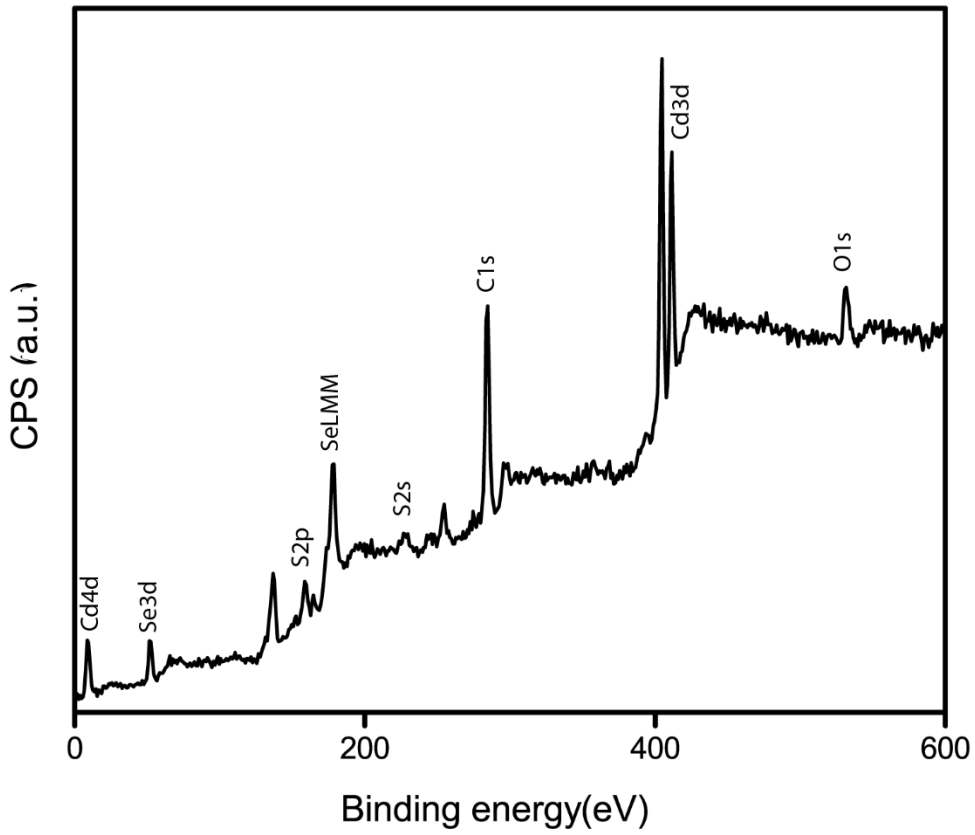


**Figure 4.4**. A typical XPS survey spectrum of CdSSe NCs showing all the elements present. Peak fitting was performed using CasaXPS data processing software. All analyses were calibrated to C 1s at 284.6 eV.

The XPS data also allowed for the determination of S/S+Se ratio in the surface region of the CdSSe NCs. **Table 4.4** shows the calculated composition of the CdSSe NCs at different growth times. There is a gradual increase of the S content in the system when reaction time is increased. The overall %Cd stays nearly constant throughout the entire reaction time, suggesting that the reaction undergoes in a Cd-rich conditions. It was also found that at the initial growth stage, the Se content

is higher. This indicates the early formation of CdSe like core due to the difference in the nucleation kinetics of S and Se precursors, i.e. TOP-Se reacts faster with Cd(II) precursor than TOP-S.[23, 39, 53-54] Since the reactivity of the TOP-Se towards the Cd salt precursor is higher than that of S-TOP, the NCs evolve with a gradient composition having a Se-enriched core followed by gradual incorporation of S into the CdSe lattice.

**Table 4.4**. XPS data showing the elemental composition of CdSSe NCs at different growth times

| **Sample growth time** | **% Cd** | **% Se** | **% S** | **S:(S+Se)** | **$CdS_xSe_{1-x}$** |
|---|---|---|---|---|---|
| 1min | 60.92 | 34.25 | 4.83 | 0.14 | $CdS_{0.14}Se_{0.86}$ |
| 5min | 61.30 | 33.00 | 5.70 | 0.18 | $CdS_{0.18}Se_{0.82}$ |
| 10min | 59.80 | 32.71 | 7.49 | 0.24 | $CdS_{0.24}Se_{0.76}$ |
| 15min | 60.41 | 29.77 | 9.82 | 0.33 | $CdS_{0.33}Se_{0.67}$ |
| 25min | 58.41 | 29.70 | 11.88 | 0.40 | $CdS_{0.40}Se_{0.60}$ |

The crystal structure of the NCs was determined by the X-ray diffraction (XRD) data as shown in **Figure 4.5**. As depicted by the XRD patterns, the major diffraction peaks of (100), (002), (101), (110), (103) and (112) planes were observed, corresponding to a typical hexagonal wurtzite structure.[21, 33, 39, 55-58] As mentioned in most of the earlier works on alloyed CdSeS systems[23, 39, 52], if the resultant NCs were a mixture of individual CdSe and CdS domains, the XRD pattern would

likely be a superposition of XRD patterns of pure bulk CdSe and CdS. Instead, we observe that the diffraction peaks of our alloyed samples lie intermediate between bulk CdSe (JCPDS no.00-002-0330) and bulk CdS (JCPDS no.00-002-0549), which again confirms the formation of alloyed NCs.

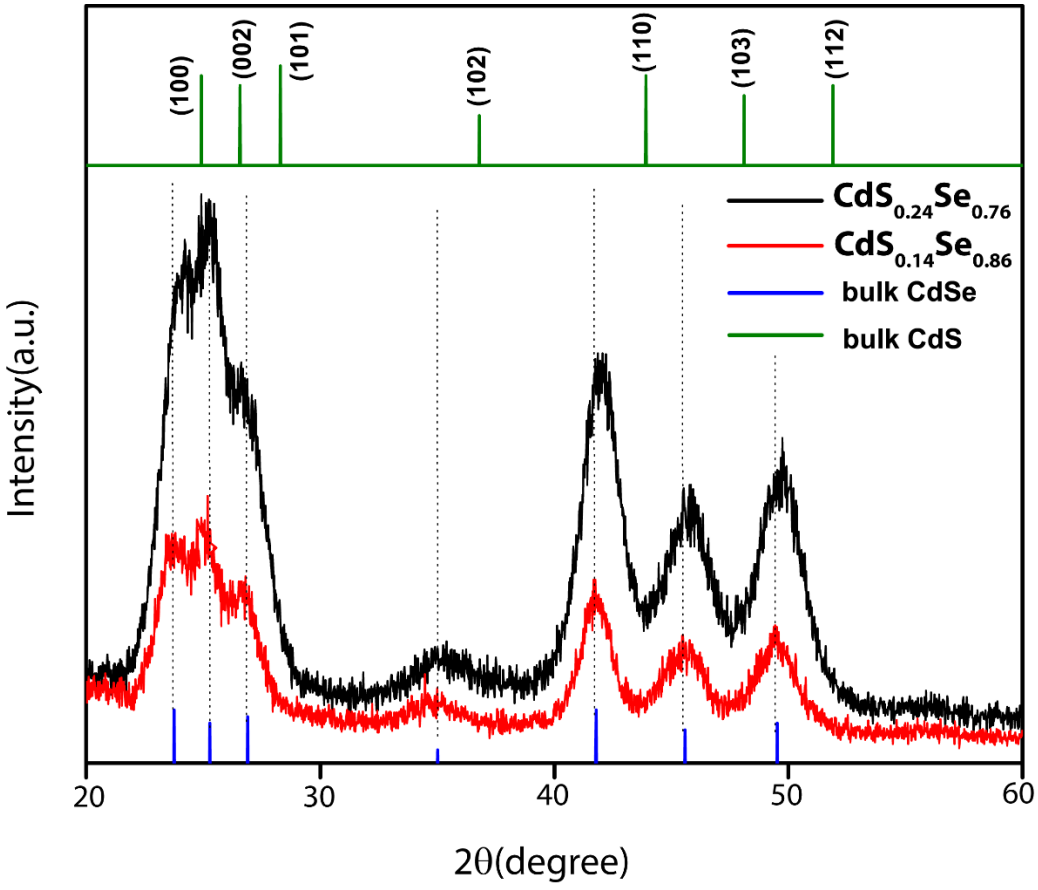


**Figure 4.5**. Powder XRD spectra of CdSSe QDs at different growth times (1 min, red and 10 min, black), showing hexagonal wurtzite structure. The 2θ values for all the major diffraction peaks of both the NC samples lie between that of pure bulk CdSe (blue, JCPDS no. 00-002-0330) and CdS(green, JCPDS no. 00-002-0549), which indicates the formation of alloyed NCs.

The XRD data in **Figure 4.5** shows a sequential shift of all the major diffraction peaks towards a higher value of 2θ for the samples with a higher percentage of S. Notice that the lattice

constants of hexagonal bulk wurtzite CdS (a = b = 4.13 Å, c = 6.74 Å) and bulk CdSe ( a = b = 4.3 Å, c= 7.01 Å).[59] As the reaction proceeds, more S gets incorporated into the crystal lattice of the NCs. As a consequence, the lattice constants decreased which resulted in shifting of peaks towards larger 2θ values. Detailed information on the peak patterns of our samples ((hkl) vs 2θ) are also provided in the **Table 4.5** below.

**Table 4.5**. Powder XRD data showing (hkl) vs 2θ values for the wurtzite type alloyed CdSSe NCs at two different growth times ($CdS_{0.14}Se_{0.86}$,1min and $CdS_{0.24}Se_{0.76}$,10min)

| **(hkl)** | **Bulk CdSe(00-002-0330)** | **Bulk CdS(00-002-0549)** | **$CdS_{0.14}Se_{0.86}$** | **$CdS_{0.24}Se_{0.76}$** |
|---|---|---|---|---|
| (100) | 23.77 | 24.92 | 23.87 | 24.06 |
| (002) | 25.28 | 26.59 | 25.08 | 25.40 |
| (101) | 26.91 | 28.31 | 26.65 | 27.09 |
| (102) | 35.02 | 36.80 | 34.76 | 35.32 |
| (110) | 41.78 | 43.92 | 41.76 | 42.10 |
| (103) | 45.59 | 48.10 | 45.53 | 45.73 |
| (112) | 49.53 | 51.91 | 49.40 | 49.84 |

To evaluate the emitting properties of the CdSSe NCs, the PL quantum yields (QYs) of the alloyed NC samples at different reaction times were measured. It is observed that the QY increases from 28% to 45% as the reaction proceeds. The increase in QY with longer reaction time is likely due to the better surface passivation more S gets incorporated into the pseudo-core/shell NCs, decreasing the non-radiative recombination rate. The PL intensity trajectories of individual CdSSe

NCs on glass substrate were acquired under 532 nm pulsed laser excitation with a pulse repetition rate of 2.5 MHz at an excitation power of 40 nW. For comparison, CdSe NCs synthesized using Peng's method[51] (emitting at 625nm) with slight modification and single CdSSe NCs (25min sample, $CdS_{0.40}Se_{0.60}$ emitting at 630nm) were studied under the same conditions. The representative blinking traces of single CdSSe and CdSe NCs are shown in **Figure 4.6A** and **Figure 4.6D**, respectively. The PL intensity distribution is provided by the right side of each intensity trace, from which the background level ("off" state) and the emission state ("on" state) can be distinguished. The red lines denote the intensity threshold level between the "on" and "off" states as obtained from bin-threshold mode of analysis.

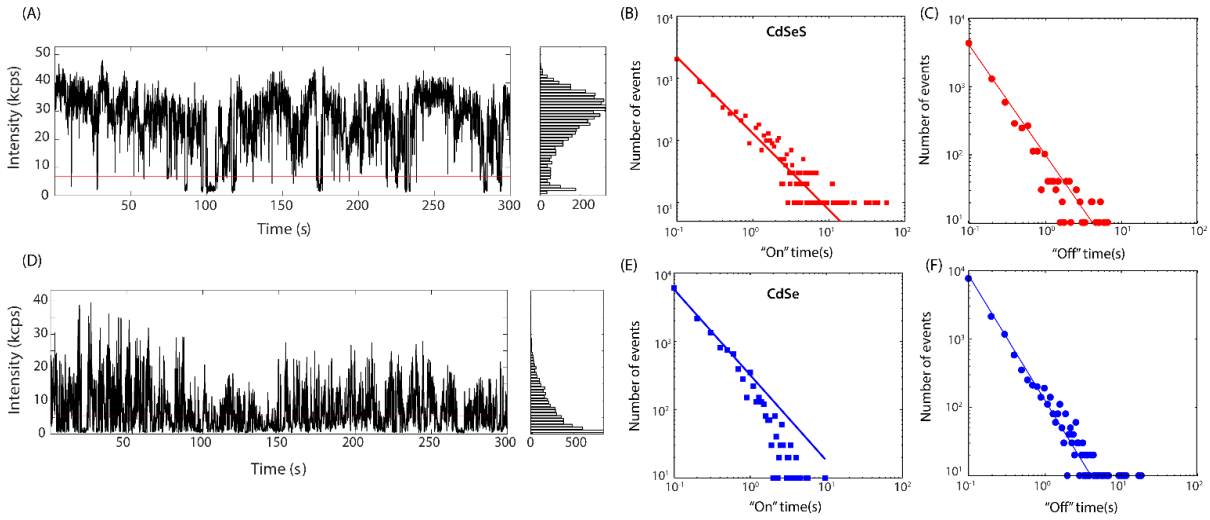


**Figure 4.6**. (A) Representative PL intensity trajectories of a single CdSSe NC with binning time of 50 ms and corresponding intensity distribution histograms. (B) and (C) the distribution of "on" and "off" times of CdSSe NC. (D-F) the corresponding PL time trace and "on"/"off" times for a CdSe NC, as comparison.

Comparing the PL traces of single CdSSe and CdSe NCs, the CdSSe NCs shows a clear two-step binary blinking with a well-defined "on" and "off" states. The intensity histogram of CdSSe clearly exhibits a bimodal distribution with a higher "on" time fraction as compared to CdSe. In the case of CdSe, the emission trace shows spikier intensity signals with much shorter "on" events and longer "off" events. From the PL intensity trajectories, we have also analyzed the distribution of "on" and "off" durations for single CdSSe (Fig.6B and C) and CdSe (Fig.6E and F) NCs. From **Figure 4.6B** and **Figure 4.6C**, the distributions of "on"/"off" times of CdSSe NC fit well with the power–law distribution (Number of events $\propto {t_{on/off}}^{-\alpha_{on/off}}$), where $\alpha_{on} = -1.10$,

and $\alpha_{off} = -1.60$. The blinking statistics of CdSSe is similar to that of CdSe/CdS core/shell QDs.[60-63] For CdSe NCs, the "on" time probability distributions are well described by an inverse power law for shorter duration times with $\alpha_{on} = -1.25$, crossing over to an exponential fall-off at longer duration times. The probability distribution of "off" time events fits well with a power law with $\alpha_{off} = -1.82$. These results indicated that the CdSSe NCs statistically have more "on" and fewer "off" events than CdSe. Moreover, the "on" time statistical distribution of CdSe followed "truncated power law", and that of CdSSe followed "expanded power-law". We have also plotted "on" time fraction histograms out of 67 single CdSSe NCs (**Figure 4.7A**) and 53 single CdSe NCs (**Figure 4.7B**).

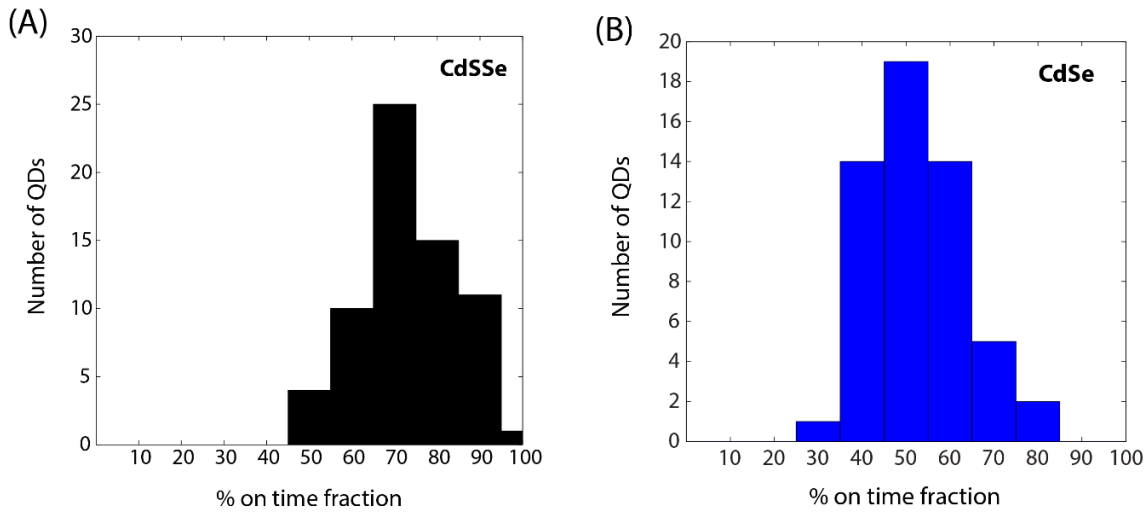


**Figure 4.7**. Histograms of the "on" time fraction of single (A) CdSSe and (B) CdSe NCs. The histograms were built out of 67 CdSSe NCs and 54 CdSe NCs.

It was observed that 76% of the single CdSSe NCs exhibited an "on" time fraction greater than 70%, as compared to only 13% of CdSe have "on" time fraction > 70%. Moreover, the on-time fraction distribution of CdSSe was much narrower compared to CdSe, which could be due to reduced surface defects in the alloyed NCs. It is important to note that with a little incorporation of S into NC lattice resulted in a significant improvement in the optical properties (with relatively reduced blinking) as observed at the single particle level.

The photostability of the alloyed CdSSe and that of binary CdSe NCs were further examined at longer acquisition time as shown in the representative time traces for the CdSSe and CdSe NCs in **Figure 4.8** . No significant change in the emitting behaviour was observed for the CdSSe NCs. Even exciting them for 20 min, they still exhibit a clear bimodal distribution of PL intensities as shown in **Figure 4.8A**. On the contrary, the CdSe NCs under prolonged excitation has long "off" events and the PL intensity became much lower (**Figure 4.8B**). The gradual decrease in their intensity can be attributed to the fact that CdSe NCs are more prone to photooxidation or photobleaching as compared to the alloyed CdSSe NCs. In addition, it is observed that when the NCs were deposited on glass substrate and exposed in air overnight, the CdSSe NCs were still emitting without much change in the intensity whereas most of the CdSe NCs stopped emitting. This experiment shows that even without photo excitation, the CdSe NCs can easily be oxidized irreversibly while the CdSSe are much more stable.

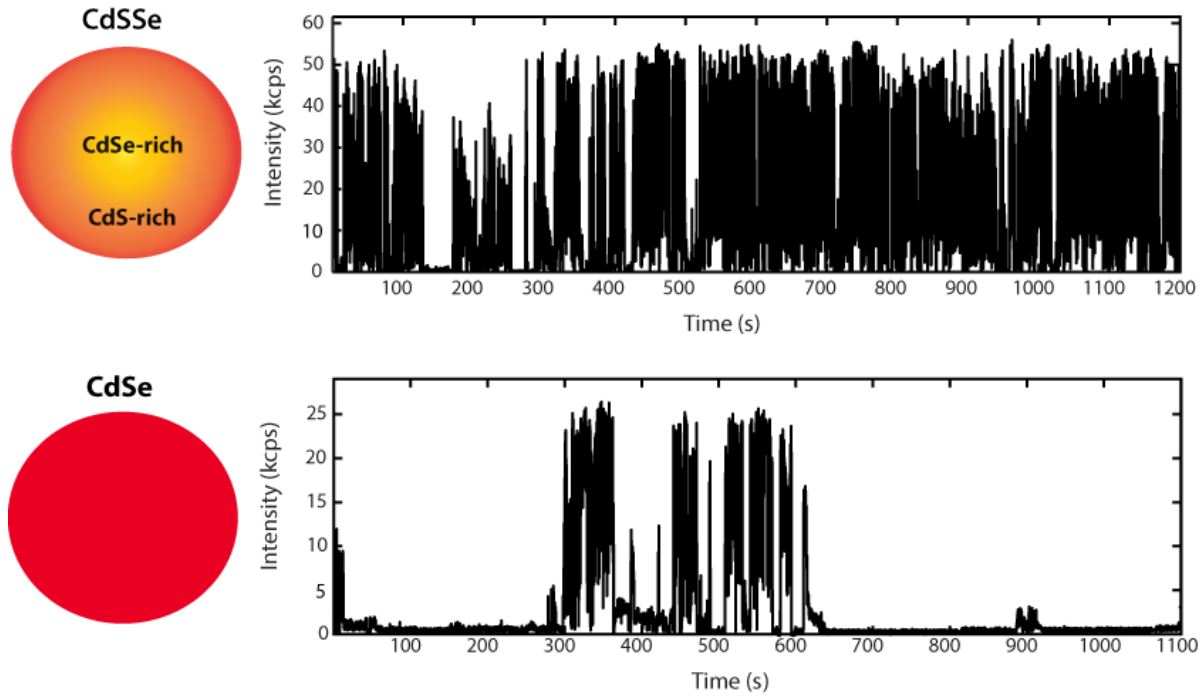


**Figure 4.8**. Pictorial representation of the variation in internal structures of CdSSe and CdSe nanocrystals((left), Photostability comparison from the emission trajectories between the single (A)CdSSe and (B)CdSe NCs. The CdSSe NC shows more robustness in their emission behavior without any considerable change in their intensities as compared to CdSe NC under longer duration of data acquisition

In an attempt to further explore the stability of CdSSe NCs in water phase, we performed ligand exchange with methoxy-polyethylene-glycol thiol (PEG-SH) using a similar procedure as described earlier by Chen et al.[60] After the ligand exchange, the CdSSe NCs were successfully transferred from their native phase hexane into phosphate buffer/water medium without any significant loss in their PL QY(QY before/after ligand exchange = 45%/31%), in contrast to some earlier reported works, where usually phase transfer results in a significant lowering of the PL

QY.[64-66] After being phase transferred into water, the NCs still remained fluorescent and stable for at least 6 months without any considerable change in their emission intensity (**Figure 4.9**).

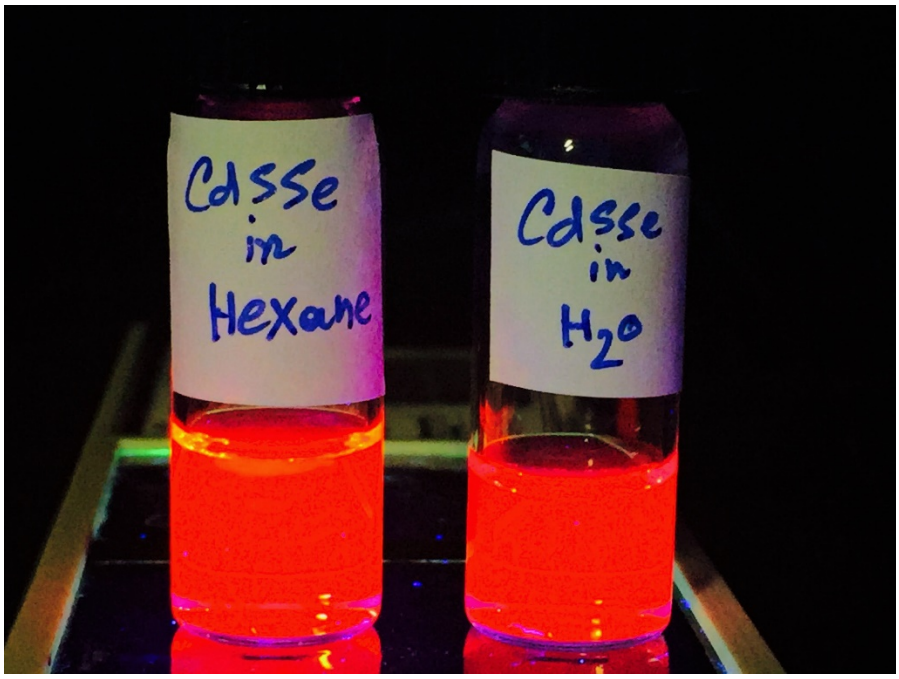


**Figure 4.9**. Images showing the CdSSe NCs before(dispersed in hexane) and after phase transfer(dispersed in nanopure water).The NCs stay well dispersed in water even after 3-6months of ligand exchange (under storage conditions at $4^0$C)

From the optical studies of the CdSSe NCs at both the ensemble and single NC level, the gradient alloyed CdSSe NCs from the one-step synthesis exhibit significantly improved PL behavior compared to the CdSe NCs. The improvement can be attributed to several factors. One, the incorporation of S into CdSSe provides better surface passivation, thus decreasing surface trapping related non-radiative recombination rates. Second, the gradient structure yields a smoothed interface between the Se rich "core" and S rich "shell", suppressing Auger recombination. These two factors result in reduced blinking and high "on" fraction of the NCs.

Lastly, S protects the NC from (photo)oxidation, increasing the stability for the NCs. The gradient alloyed CdSSe NCs are promising fluorophores with high quantum yield and stable emission.

## 4.5. Conclusions

In the present study, we reported a one-pot synthesis of alloyed CdSSe NCs prepared at reduced temperature. The NCs have uniform size distribution of a QY of 45%. In-depth structure and composition analyses using TEM, HAADF-STEM, XPS and XRD showed the wurtzite NCs had a pseudo core-shell structure with a Se-rich core and S present on the outer regions of the NCs, due to the different reactivity of Se and S precursors with Cd(II) salt. PL intensity time traces of single CdSSe NCs exhibited significantly reduced blinking and increased "on" time fraction compared to single CdSe NCs. The improved PL properties are attributed to better surface passivation and a gradual change in the composition due to the formation of gradient alloy structure. The findings demonstrated progress towards fabrication and characterization of gradient cadmium based alloyed NCs, which are useful for various biomedical and optoelectronic applications. Further studies are still required in order to elucidate how the composition of the NCs will affect their blinking and photostability without increasing the overall size.

## 4.6. Acknowledgement

JZ would like to acknowledge the financial support from UConn Startup Funds and the American Chemical Society Petroleum Research Fund (PRF# 54004-DN15). ST thanks the financial support from FEI fellowship.

## 4.7. References


1. Colvin, V. L.; Schlamp, M. C.; Alivisatos, A. P., Light-Emitting Diodes Made from Cadmium Selenide Nanocrystals and a Semiconducting Polymer. *Nature* **1994**, *370*, 354-357.
2. Tessler, N.; Medvedev, V.; Kazes, M.; Kan, S.; Banin, U., Efficient near-Infrared Polymer Nanocrystal Light-Emitting Diodes. *Science* **2002**, *295*, 1506-1508.
3. Klimov, V. I.; Mikhailovsky, A. A.; Xu, S.; Malko, A.; Hollingsworth, J. A.; Leatherdale, C. A.; Eisler, H.-J.; Bawendi, M. G., Optical Gain and Stimulated Emission in Nanocrystal Quantum Dots. *Science* **2000**, *290*, 314-317.
4. Chan, W. C. W.; Nie, S., Quantum Dot Bioconjugates for Ultrasensitive Nonisotopic Detection. *Science* **1998**, *281*, 2016-2018.
5. Han, M.; Gao, X.; Su, J. Z.; Nie, S., Quantum-Dot-Tagged Microbeads for Multiplexed Optical Coding of Biomolecules. *Nat.Biotech.* **2001**, *19*, 631-635.
6. Bruchez, M.; Moronne, M.; Gin, P.; Weiss, S.; Alivisatos, A. P., Semiconductor Nanocrystals as Fluorescent Biological Labels. *Science* **1998**, *281*, 2013-2016.
7. Murray, C. B.; Norris, D. J.; Bawendi, M. G., Synthesis and Characterization of Nearly Monodisperse CdE (E = Sulfur, Selenium, Tellurium) Semiconductor Nanocrystallites. *J.Am.Chem.Soc.* **1993**, *115*, 8706-8715.
8. Peng, X., Green Chemical Approaches toward High-Quality Semiconductor Nanocrystals. *Chem.Eur.J* **2002**, *8*, 334-339.
9. Peng, Z. A.; Peng, X., Formation of High-Quality CdTe, CdSe, and CdS Nanocrystals Using CdO as Precursor. *J.Am.Chem.Soc.* **2001**, *123*, 183-184.
10. Qu, L.; Peng, Z. A.; Peng, X., Alternative Routes toward High Quality CdSe Nanocrystals. *Nano Lett.* **2001**, *1*, 333-337.
11. Qu, L.; Peng, X., Control of Photoluminescence Properties of CdSe Nanocrystals in Growth. *J.Am.Chem.Soc.* **2002**, *124*, 2049-2055.
12. Romcevic, M.; Romcevic, N.; Kostic, R.; Klopotowski, L.; Dobrowolski, W. D.; Kossut, J.; Čomor, M. I., Photoluminescence of Highly Doped $Cd_{1-x}Mn_xS$ Nanocrystals. *J.Alloys Compd.* **2010**, *497*, 46-51.
13. Mahler, B.; Lequeux, N.; Dubertret, B., Ligand-Controlled Polytypism of Thick-Shell CdSe/CdS Nanocrystals. *J.Am.Chem.Soc.* **2010**, *132*, 953-959.
14. Reiss, P.; Protiere, M.; Li, L., Core/Shell Semiconductor Nanocrystals.S*mall* **2009**, *5*, 154-168.
15. Peng, X.; Schlamp, M. C.; Kadavanich, A. V.; Alivisatos, A. P., Epitaxial Growth of Highly Luminescent CdSe/CdS Core/Shell Nanocrystals with Photostability and Electronic Accessibility. *J.Am.Chem.Soc.* **1997**, *119*, 7019-7029.
16. Anlian, P.; Hua, Y.; Richeng, Y.; Bingsuo, Z., Fabrication and Photoluminescence of High-Quality Ternary CdSSe Nanowires and Nanoribbons. *Nanotechnology* **2006**, *17*, 1083.
17. Tyrakowski, C. M.; Shamirian, A.; Rowland, C. E.; Shen, H.; Das, A.; Schaller, R. D.; Snee, P. T., Bright Type II Quantum Dots. *Chem.Mater.* **2015**, *27*, 7276-7281.
18. Greytak, A. B.; Allen, P. M.; Liu, W.; Zhao, J.; Young, E. R.; Popovic, Z.; Walker, B. J.; Nocera, D. G.; Bawendi, M. G., Alternating Layer Addition Approach to CdSe/CdS Core/Shell Quantum Dots with near-Unity Quantum Yield and High on-Time Fractions. *Chem.Sci.* **2012**, *3*, 2028-2034.
19. Li, J. J.; Wang, Y. A.; Guo, W.; Keay, J. C.; Mishima, T. D.; Johnson, M. B.; Peng, X., Large-Scale Synthesis of Nearly Monodisperse CdSe/CdS Core/Shell Nanocrystals Using Air-Stable

Reagents Via Successive Ion Layer Adsorption and Reaction. *J.Am.Chem.Soc.* **2003**, *125*, 12567-12575.
20. Yu, W. W.; Peng, X., Formation of High-Quality Cds and Other II–VI Semiconductor Nanocrystals in Noncoordinating Solvents: Tunable Reactivity of Monomers. *Angew.Chem.Int.Ed.* **2002**, *41*, 2368-2371.
21. Zhong, X.; Feng, Y.; Knoll, W.; Han, M., Alloyed $Zn_xCd_{1-x}S$ Nanocrystals with Highly Narrow Luminescence Spectral Width. *J.Am.Chem.Soc.* **2003**, *125*, 13559-13563.
22. Bailey, R. E.; Nie, S., Alloyed Semiconductor Quantum Dots: Tuning the Optical Properties without Changing the Particle Size. *J.Am.Chem.Soc.* **2003**, *125*, 7100-7106.
23. Swafford, L. A.; Weigand, L. A.; Bowers, M. J.; McBride, J. R.; Rapaport, J. L.; Watt, T. L.; Dixit, S. K.; Feldman, L. C.; Rosenthal, S. J., Homogeneously Alloyed $CdS_xSe_{1-x}$ Nanocrystals: Synthesis, Characterization, and Composition/Size-Dependent Band Gap. *J.Am.Chem.Soc.* **2006**, *128*, 12299-12306.
24. Zimmer, J. P.; Kim, S.-W.; Ohnishi, S.; Tanaka, E.; Frangioni, J. V.; Bawendi, M. G., Size Series of Small Indium Arsenide−Zinc Selenide Core−Shell Nanocrystals and Their Application to in Vivo Imaging. *J.Am.Chem.Soc.* **2006**, *128*, 2526-2527.
25. Regulacio, M. D.; Han, M.-Y., Composition-Tunable Alloyed Semiconductor Nanocrystals. *Acc.Chem.Res.* **2010**, *43*, 621-630.
26. Efros, A. L.; Rosen, M., Random Telegraph Signal in the Photoluminescence Intensity of a Single Quantum Dot. *Phys.Rev.Lett.* **1997**, *78*, 1110-1113.
27. Frantsuzov, P. A.; Volkán-Kacsó, S.; Jankó, B., Model of Fluorescence Intermittency of Single Colloidal Semiconductor Quantum Dots Using Multiple Recombination Centers. *Phys. Rev.Lett.* **2009**, *103*, 207402.
28. Kim, S.; Fisher, B.; Eisler, H.-J.; Bawendi, M., Type-II Quantum Dots: CdTe/CdSe(Core/Shell) and CdSe/ZnTe(Core/Shell) Heterostructures. *J.Am.Chem.Soc.* **2003**, *125*, 11466-11467.
29. Chen, Y.; Vela, J.; Htoon, H.; Casson, J. L.; Werder, D. J.; Bussian, D. A.; Klimov, V. I.; Hollingsworth, J. A., "Giant" Multishell CdSe Nanocrystal Quantum Dots with Suppressed Blinking. *J.Am.Chem.Soc.* **2008**, *130*, 5026-5027.
30. García-Santamaría, F.; Chen, Y.; Vela, J.; Schaller, R. D.; Hollingsworth, J. A.; Klimov, V. I., Suppressed Auger Recombination in "Giant" Nanocrystals Boosts Optical Gain Performance. *Nano Lett.* **2009**, *9*, 3482-3488.
31. Wang, X.; Ren, X.; Kahen, K.; Hahn, M. A.; Rajeswaran, M.; Maccagnano-Zacher, S.; Silcox, J.; Cragg, G. E.; Efros, A. L.; Krauss, T. D., Non-Blinking Semiconductor Nanocrystals. *Nature* **2009**, *459*, 686-689.
32. Cragg, G. E.; Efros, A. L., Suppression of Auger Processes in Confined Structures. *Nano Lett.* **2010**, *10*, 313-317.
33. Zhong, X.; Han, M.; Dong, Z.; White, T. J.; Knoll, W., Composition-Tunable $Zn_xCd_{1-x}Se$ Nanocrystals with High Luminescence and Stability. *J.Am.Chem.Soc.* **2003**, *125*, 8589-8594.
34. Zhong, X.; Zhang, Z.; Liu, S.; Han, M.; Knoll, W., Embryonic Nuclei-Induced Alloying Process for the Reproducible Synthesis of Blue-Emitting $Zn_xCd_{1-x}Se$ Nanocrystals with Long-Time Thermal Stability in Size Distribution and Emission Wavelength. *J.Phys.Chem.B* **2004**, *108*, 15552-15559.
35. Zhong, X.; Liu, S.; Zhang, Z.; Li, L.; Wei, Z.; Knoll, W., Synthesis of High-Quality CdS, ZnS, and $Zn_xCd_{1-x}S$ Nanocrystals Using Metal Salts and Elemental Sulfur. *J.Mater.Chem.* **2004**, *14*, 2790-2794.

36. Jiang, W.; Singhal, A.; Zheng, J.; Wang, C.; Chan, W. C. W., Optimizing the Synthesis of Red- to near-IR-Emitting CdS-Capped $CdTe_xSe_{1-x}$ Alloyed Quantum Dots for Biomedical Imaging. *Chem.Mater.* **2006**, *18*, 4845-4854.
37. Ratcliffe, C. I.; Yu, K.; Ripmeester, J. A.; Badruz Zaman, M.; Badarau, C.; Singh, S., Solid State Nmr Studies of Photoluminescent Cadmium Chalcogenide Nanoparticles. *Phys.Chem.Chem.Phys.* **2006**, *8*, 3510-3519.
38. Jang, E.; Jun, S.; Pu, L., High Quality Cdses Nanocrystals Synthesized by Facile Single Injection Process and Their Electroluminescence. *Chem.Commun.* **2003**, 2964-2965.
39. Al-Salim, N.; Young, A. G.; Tilley, R. D.; McQuillan, A. J.; Xia, J., Synthesis of CdSeS Nanocrystals in Coordinating and Noncoordinating Solvents: Solvent's Role in Evolution of the Optical and Structural Properties. *Chem.Mater.* **2007**, *19*, 5185-5193.
40. Ouyang, J.; Ripmeester, J. A.; Wu, X.; Kingston, D.; Yu, K.; Joly, A. G.; Chen, W., Upconversion Luminescence of Colloidal Cds and Zncds Semiconductor Quantum Dots. *J.Phys.Chem.C* **2007**, *111*, 16261-16266.
41. Ouyang, J.; Ratcliffe, C. I.; Kingston, D.; Wilkinson, B.; Kuijper, J.; Wu, X.; Ripmeester, J. A.; Yu, K., Gradiently Alloyed $Zn_xCd_{1-x}S$ Colloidal Photoluminescent Quantum Dots Synthesized Via a Noninjection One-Pot Approach. *J.Phys.Chem.C* **2008**, *112*, 4908-4919.
42. Aubert, T.; Cirillo, M.; Flamee, S.; Van Deun, R.; Lange, H.; Thomsen, C.; Hens, Z., Homogeneously Alloyed $CdSe_{1-x}S_x$ Quantum Dots ($0 \leq x \leq 1$): An Efficient Synthesis for Full Optical Tunability. *Chem.Mater.* **2013**, *25*, 2388-2390.
43. Park, Y.-S.; Bae, W. K.; Padilha, L. A.; Pietryga, J. M.; Klimov, V. I., Effect of the Core/Shell Interface on Auger Recombination Evaluated by Single-Quantum-Dot Spectroscopy. *Nano Lett.* **2014**, *14*, 396-402.
44. García-Santamaría, F.; Brovelli, S.; Viswanatha, R.; Hollingsworth, J. A.; Htoon, H.; Crooker, S. A.; Klimov, V. I., Breakdown of Volume Scaling in Auger Recombination in CdSe/CdS Heteronanocrystals: The Role of the Core−Shell Interface. *Nano Lett.* **2011**, *11*, 687-693.
45. Lifshitz, E.; Vaxenburg, R.; Maikov, G. I.; Rubin-Brusilovski, A.; Yanover, D.; Tilchin, J.; Sashchiuk, A., The Influence of Alloy Composition on the Electronic Properties of IV–VI Core/Shell Colloidal Heterostructures. *Isr.J.Chem.* **2012**, *52*, 1037-1052.
46. Maikov, G. I.; Vaxenburg, R.; Sashchiuk, A.; Lifshitz, E., Composition-Tunable Optical Properties of Colloidal IV−VI Quantum Dots, Composed of Core/Shell Heterostructures with Alloy Components. *ACS Nano* **2010**, *4*, 6547-6556.
47. Talapin, D. V.; Koeppe, R.; Götzinger, S.; Kornowski, A.; Lupton, J. M.; Rogach, A. L.; Benson, O.; Feldmann, J.; Weller, H., Highly Emissive Colloidal CdSe/CdS Heterostructures of Mixed Dimensionality. *Nano Lett.* **2003**, *3*, 1677-1681.
48. Xie, R.; Kolb, U.; Li, J.; Basché, T.; Mews, A., Synthesis and Characterization of Highly Luminescent CdSe−Core $CdS/Zn_{0.5}Cd_{0.5}S/ZnS$ Multishell Nanocrystals. *J.Am.Chem.Soc.* **2005**, *127*, 7480-7488.
49. van Embden, J.; Jasieniak, J.; Mulvaney, P., Mapping the Optical Properties of CdSe/CdS Heterostructure Nanocrystals: The Effects of Core Size and Shell Thickness. *J.Am.Chem.Soc.* **2009**, *131*, 14299-14309.
50. Keene, J. D.; McBride, J. R.; Orfield, N. J.; Rosenthal, S. J., Elimination of Hole–Surface Overlap in Graded $CdS_xSe_{1-x}$ Nanocrystals Revealed by Ultrafast Fluorescence Upconversion Spectroscopy. *ACS Nano* **2014**, *8*, 10665-10673.

51. Nan, W.; Niu, Y.; Qin, H.; Cui, F.; Yang, Y.; Lai, R.; Lin, W.; Peng, X., Crystal Structure Control of Zinc-Blende CdSe/CdS Core/Shell Nanocrystals: Synthesis and Structure-Dependent Optical Properties. *J.Am.Chem.Soc.* **2012**, *134*, 19685-19693.
52. Wang, B.; Jiang, Y.; Liu, C.; Lan, X.; Liu, X.; Wang, W.; Duan, H.; Zhang, Y.; Li, S.; Zhang, Z., One-Pot Synthesis of Homogeneous $CdSe_xS_{1-x}$ Alloyed Quantum Dots with Tunable Composition in a Green N-Oleoylmorpholine Solvent. *Phys.Stat.Solidi A* **2012**, *209*, 306-312.
53. Ouyang, J.; Vincent, M.; Kingston, D.; Descours, P.; Boivineau, T.; Zaman, M. B.; Wu, X.; Yu, K., Noninjection, One-Pot Synthesis of Photoluminescent Colloidal Homogeneously Alloyed CdSeS Quantum Dots. *J.Phys.Chem.C* **2009**, *113*, 5193-5200.
54. Harrison, M. A.; Ng, A.; Hmelo, A. B.; Rosenthal, S. J., CdSSe Nanocrystals with Induced Chemical Composition Gradients. *Isr.J.Chem.* **2012**, *52*, 1063-1072.
55. Zou, Y.; Li, D.; Yang, D., Single Step Synthesis of Cdses Nanorods with Chemical Composition Gradients. *J.Cryst.Growth* **2010**, *312*, 3406-3409.
56. Chen, Z.; Tian, Q.; Song, Y.; Yang, J.; Hu, J., One-Pot Synthesis of $Zn_xCd_{1-x}S$ Nanocrystals with Tunable Optical Properties from Molecular Precursors. *J.Alloys Compd.* **2010**, *506*, 804-810.
57. Hou, B.; Parker, D.; Kissling, G. P.; Jones, J. A.; Cherns, D.; Fermín, D. J., Structure and Band Edge Energy of Highly Luminescent $CdSe_{1-x}Te_x$ Alloyed Quantum Dots. *J.Phys.Chem.C* **2013**, *117*, 6814-6820.
58. Tan, G.; Li, S.; Murowchick, J. B.; Wisner, C.; Leventis, N.; Peng, Z., Preparation of Uncapped $CdSe_{1-x}S_x$ Semiconducting Nanocrystals by Mechanical Alloying. *J.Appl.Phys.* **2011**, *110*, 124306.
59. Xu, Y.-N.; Ching, W. Y., Electronic, Optical, and Structural Properties of Some Wurtzite Crystals. *Phys.Rev. B* **1993**, *48*, 4335-4351.
60. Chen, O., et al., Compact High-Quality Cdse–Cds Core–Shell Nanocrystals with Narrow Emission Linewidths and suppressed Blinking. *Nat.Mater.* **2013**, *12*, 445-451.
61. Vela, J.; Htoon, H.; Chen, Y.; Park, Y.-S.; Ghosh, Y.; Goodwin, P. M.; Werner, J. H.; Wells, N. P.; Casson, J. L.; Hollingsworth, J. A., Effect of Shell Thickness and Composition on Blinking Suppression and the Blinking Mechanism in 'Giant' CdSe/CdS Nanocrystal Quantum Dots. *J.Biophotonics* **2010**, *3*, 706-717.
62. Mahler, B.; Spinicelli, P.; Buil, S.; Quelin, X.; Hermier, J.-P.; Dubertret, B., Towards Non-Blinking Colloidal Quantum Dots. *Nat.Mater.* **2008**, *7*, 659-664.
63. Heyes, C. D.; Kobitski, A. Y.; Breus, V. V.; Nienhaus, G. U., Effect of the Shell on the Blinking Statistics of Core-Shell Quantum Dots: A Single-Particle Fluorescence Study. *Phys. Rev.B* **2007**, *75*, 125431.
64. Gaponik, N.; Talapin, D. V.; Rogach, A. L.; Eychmüller, A.; Weller, H., Efficient Phase Transfer of Luminescent Thiol-Capped Nanocrystals: From Water to Nonpolar Organic Solvents. *Nano Lett.* **2002**, *2*, 803-806.
65. Gao, X.; Cui, Y.; Levenson, R. M.; Chung, L. W. K.; Nie, S., In Vivo Cancer Targeting and Imaging with Semiconductor Quantum Dots. *Nat.Biotech.* **2004**, *22*, 969-976.
66. Su, Y.; He, Y.; Lu, H.; Sai, L.; Li, Q.; Li, W.; Wang, L.; Shen, P.; Huang, Q.; Fan, C., The Cytotoxicity of Cadmium Based, Aqueous Phase – Synthesized, Quantum Dots and Its Modulation by Surface Coating. *Biomaterials* **2009**, *30*, 19-25.